Instantaneous planar pressure determination from particle image velocimetry

Roeland DE KAT

Instantaneous planar pressure determination from particle image velocimetry

Proefschrift

ter verkrijging van de graad van doctor
aan de Technische Universiteit Delft;
op het gezag van de Rector Magnificus prof. ir. K. C. A. M. Luyben;
voorzitter van het College voor Promoties
in het openbaar te verdedigen
op maandag 5 maart 2012 om 10.00 uur

door

Roeland DE KAT
ingenieur luchtvaart en ruimtevaart
geboren te Utrecht

Dit proefschrift is goedgekeurd door de promotor:
Prof. dr. F. Scarano.

Copromotor:
Dr. ir. B. W. van Oudheusden.

Samenstelling promotiecommissie:

Rector Magnificus,	voorzitter
Prof. dr. F. Scarano,	Technische Universiteit Delft, promotor
Dr. ir. B. W. van Oudheusden,	Technische Universiteit Delft, copromotor
Prof. Dr. J. Katz,	Johns Hopkins University, USA
Prof. Dr. rer. nat. C. J. Kähler,	Universität der Bundeswehr München, D
Prof. Dr.-Ing. G. Eitelberg,	Technische Universiteit Delft
Prof. dr. ir. J. Westerweel,	Technische Universiteit Delft
Dr. B. Ganapathisubramani,	University of Southampton, UK
Prof. dr. ir. drs. H. Bijl,	Technische Universiteit Delft, reservelid

to my love Ana

Abstract

Instantaneous planar pressure determination from particle image velocimetry

Forces on flapping or rotating wings, like flapping wings of micro air vehicles or blades of wind turbines are of great interest to engineers. To investigate the ways birds and insects fly, forces created by flapping wings are of importance to biologists. The pressure field, combined with the velocity field, gives a complete description of the (incompressible) flow dynamics. Furthermore the pressure field is the main contributor to the aerodynamic loading of bodies immersed in the fluid.

Traditional techniques to determine pressure and forces rely on the determination of surface pressure and integral loads by point pressure and force balance measurements. In situations where it is difficult (or impossible) to instrument the body, using particle image velocimetry (PIV) velocity data to determine forces and pressure poses an interesting alternative to the existing approaches to determine sectional loading.

The operating principle of obtaining pressure from PIV-data, using either a Eulerian or a Lagrangian approach, is covered and, based on the current implementation, theoretical considerations lead to estimates of the limitations of the method. These estimates are checked using a performance analysis on a synthetic flow field, comprised of an advecting Gaussian vortex, as well as on an experimental test-case, the flow around a square cylinder. All results indicate that in order to perform successful pressure-PIV the following criteria should be met:

The spatial resolution needed to successfully (based on peak mod-

ulation smaller than 10%) perform pressure-PIV is $WS/\lambda_x < 0.2$ (*WS* is the interrogation window size and λ_x is the spatial wavelength(s) present in the flow) and was found to be the same for both the Eulerian and the Lagrangian approach.

The temporal resolution needed to successfully perform pressure-PIV is $f_{acq} > 10 \times f_{flow}$ (f_{acq} is the acquisition frequency and f_{flow} is the frequency/frequencies in the flow). For the Eulerian approach f_{flow} is related to the Eulerian time scales. For the Lagrangian approach f_{flow} is related to the Lagrangian time scales. Depending on the problem at hand one method might be more suitable than the other.

Addition of the third component is necessary in order to successfully obtain the pressure from the velocity field in 3D flow. The influence of measurement noise could not be observed in the current analysis of the experimental results.

The description of the pressure field around and loading on a square cylinder showed that the vortices, emanating from the shear-layer instability change the flow around the cylinder significantly. Pressure loading and pressure fluctuations along the side of the cylinder can increase, depending on Reynolds number. An increase in amplitude of estimated periodic lift for $Re_D = 9,500$ compared with $Re_D = 6,000$ and $19,000$ of $> 10\%$ was found. Together with the slight change in location of the Kármán-like vortex in the wake this suggest an intimate (and complex) relationship exists between the side-wall pressure, shear-layer, separation region, and near-wake, which changes significantly with Reynolds number.

Samenvatting

Instantane drukbepaling in een vlak met "particle image velocimetry"

Krachten op klappende of roterende elementen, zoals klappende vleugels van "micro air vehicles" of de bladen van een windturbine, zijn van groot belang voor ingenieurs. Om te onderzoeken hoe vogels en insecten vliegen zijn de krachten geproduceerd door klappende vleugels belangrijk voor biologen. Het drukveld, samen met het snelheidveld, geeft een complete beschrijving van de (incompressibele) stromingsdynamiek. Verder levert het drukveld de hoofdbijdrage aan de krachten die een stroming op een lichaam uitoefent.

Traditionele technieken om druk en krachten te bepalen, vertrouwen op oppervlaktedruk en integrale belasting op basis van punt druk en krachtenbalans metingen. In situaties waar het moeilijk (of onmogelijk) is om het voorwerp te instrumenteren kan het gebruik van PIV om sectiegewijze krachten en druk te bepalen een uitkomst bieden.

De basis principes voor drukbepaling van PIV-data, door middel van een Eulerian of een Lagrangian methode, wordt beschreven. Theoretische afwegingen leiden, op basis van de huidige implementatie, tot afschattingen van de beperkingen van de methode. Deze afschattingen zijn getest met een prestatie analyse op een synthetische stroming, bestaande uit een met de stroming meebewegende Gaussische wervel, en tevens met een experimentele test-case, de stroming rondom een vierkante balk. Alle resultaten geven aan dat er aan een aantal criteria voldaan moet worden om succesvol druk te bepalen uit PIV-data. Deze criteria zijn:

De benodigde ruimtelijke resolutie voor succesvolle (gebaseerd op een piekmodulatie kleiner dan 10%) drukbepaling is $WS/\lambda_x < 0.2$ en is hetzelfde voor zowel de Eulerian als de Lagrangian methode.

De benodigde tijdsresolutie is $f_{acq} > 10 \times f_{flow}$. Voor de Eulerian methode is f_{flow} gerelateerd aan de Eulerian tijdschalen en voor de Lagrangian methode aan de Lagrangian tijdschalen. Afhankelijk van het probleem dat onderzocht wordt kan de ene methode beter geschikt zijn dan de andere.

Toevoeging van de derde component is noodzakelijk om succesvol druk te bepalen van het snelheidsveld in 3D stromingen. De invloed van meetruis kan niet worden waargenomen met de huidige analyse van de experimentele resultaten.

Het experiment op de vierkante balk laat zien dat wervels, die ontstaan vanuit de "shear-layer" instabiliteit, een significant invloed hebben op het stromingsveld rondom de balk. Druk belasting en druk fluctuaties langs de zijkant van de balk kunnen toenemen, afhankelijk van het Reynolds getal. Een toename in amplitude voor (benaderde) periodieke lift van $> 10\%$ is gevonden voor $Re_D = 9{,}500$ in vergelijking met $Re_D = 6{,}000$ en $19{,}000$. Dit, samen met de subtiele verandering van de locatie van de Kármán-achtige wervel, suggereert dat er een intieme (en complexe) relatie bestaat tussen de druk op de zijkant, de "shear-layer", het losgelaten gebied en het zog. Deze relatie verandert significant met een verandering van het Reynolds getal.

Contents

Chapter 1

Introduction

The pressure field in a fluid is of great interest in both fluid mechanics and engineering. Combined with the velocity field, the pressure field gives a complete description of the (incompressible) flow dynamics. Furthermore the pressure field is the main contributor to the aerodynamic loading of bodies immersed in the fluid.

Traditional techniques to determine pressure and forces rely on the determination of surface pressure and integral loads by point pressure and force balance measurements. These methods have their advantages and disadvantages. Using PIV velocity data to determine forces and pressure poses a interesting complementary method to the existing approaches, since it potentially can be used in regimes where direct force and pressure measurements are problematic or impossible. Think of pressure fields around and forces on flapping wings of birds, insects or micro air vehicles, see e.g. figure 1.1. Also for rotating structures, like wind turbines and propellers, where it is difficult to instrument the body, this technique could pose a rather straightforward alternative in determining sectional loading.

Apart from addressing techniques to extract pressure fields from velocity measurements, the thesis also considers its application in the analysis of bluff body flow. This introduction provides a brief historical sketch of fluid dynamics, followed by a description of the current state of technology with regards to force and pressure determination from velocity data. The flow around bluff bodies is interesting and challenging,

Figure 1.1: Damselfly (Beautiful Demoiselle, *left*). Flapping micro air vehicle, DelFly II, in hovering flight (*right*, de Clercq et al. 2009)

and it is difficult to understand and to fully capture its behaviour, due to the complex unsteady and three-dimensional behaviour, especially at moderate to high Reynolds numbers. Therefore the square cylinder was used as an experimental test bed. The square cylinder flow problem is introduced. Next, the aims and objectives of this thesis are stated. Finally the outline of the thesis will be given.

1.1 Short historical sketch

This short historical sketch is intended to give a global and concise view of the scientific context of the research described in this thesis. For more complete descriptions on history and theory the reader is referred to standard fluid dynamic text books, such as White (1991) and Anderson (1991), whose works were the basis of this sketch.

The forces exerted on a body immersed in a (viscous) fluid are of great interest for engineering applications. The related theory dates back to the work of Archimedes (287-212 B.C.) with his two postulates of buoyancy. However, it took a long time before a mathematical sound description of fluid flow (and therefore the forces acting on a body immersed in it) was formulated. Having its origin in the work of Newton's *Principia* it took over a century before the form of the fluid flow equations we know today took shape. Various contributions
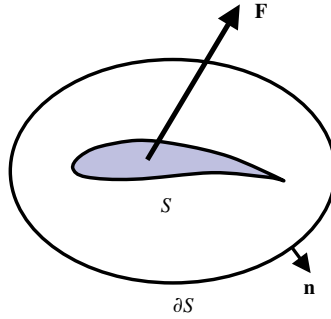
Figure 1.2: Control volume. Adapted from van Oudheusden et al. (2007)

with varying importance and elegance were made by Bernoulli, Euler, Lagrange, Laplace, Gerstner, Navier, Cauchy, Poisson, St. Venant and Stokes, which finally resulted in the Navier-Stokes (momentum) equations

$$\rho \frac{D\mathbf{u}}{Dt} = \rho \left\{ \frac{\partial \mathbf{u}}{\partial t} + (\mathbf{u} \cdot \nabla)\mathbf{u} \right\} = \rho \mathbf{f_b} - \nabla p + \mu \nabla^2 \mathbf{u}, \qquad (1.1)$$

where $D\mathbf{u}/Dt$ is the material acceleration, $\partial \mathbf{u}/\partial t$ is the local acceleration, $\mathbf{u} \cdot \nabla$ the advective operator, $\mathbf{f_b}$ the body force (like gravitational acceleration), ∇p the pressure gradient, μ the fluid viscosity, and $\nabla^2 \mathbf{u}$ the Laplacian of the velocity.

Forces acting on a body immersed in a fluid can be described by a control volume approach (see Anderson 1991) using the integral form of the momentum equations (with omission of the body force term)

$$\mathbf{F} = \int_S \rho \frac{\partial \mathbf{u}}{\partial t} dV + \int_{\partial S} \left\{ \rho (\mathbf{u} \cdot \mathbf{n})\mathbf{u} - p\mathbf{n} + \tau \cdot \mathbf{n} \right\} dA, \qquad (1.2)$$

where τ is the viscous stress tensor, S the control volume, ∂S the exterior boundary of the control volume and $\mathbf{n}$ the normal to ∂S, see figure 1.2.

Representing the forces on a body as a function of the flow around it is convenient, for measuring pressure and friction forces directly on the

body surface poses significant instrumentation challenges. This form is therefore widely used in solving engineering problems.

The momentum equations pose considerable difficulties in handling, due to their inherent nonlinearity and complexity. To date there is still no unique general analytic solution to these equations. With the advent of computational fluid dynamics the Navier-Stokes equations can be solved explicitly for a specific problem, but only on a limited domain and for a limited range of Reynolds numbers. Especially the simulation capability for high Reynolds number flows with transitional and turbulent effects remains limited in accuracy. Since the means of describing flow theoretically and numerically are limited, experiments are needed to validate the theory and numerics, as well as to gain understanding in the areas where theory and numerics are unable to capture the correct physics.

With the development and success of particle image velocimetry (PIV, see e.g. Adrian 2005, Raffel et al. 2007), a nonintrusive flow diagnostic technique, new potentials have emerged to gain insight in flow physics by determining complete (instantaneous planar) velocity fields. With cameras and lasers obtaining higher and higher acquisition frequencies, more and more flows can be captured time-resolved. PIV has proven its capability in characterizing instantaneous velocity fields and derived quantities such as vorticity, whereas its use in determining forces and pressure fields, using equation 1.1 and equation 1.2, just has started to be explored.

1.2   State-of-technology

Considerable effort has been put into deriving forces from velocity-fields (such as delivered by PIV-data) and even though the pressure field is an integral part of the forces that are exerted on the body immersed in the fluid, most efforts try to avoid calculating the pressure explicitly. Lin & Rockwell (1996) show the link between vortical structures in the wake of a circular cylinder and the forces on it, using the impulse concept as introduced by Lighthill (1986). Noca et al. (1997, 1999) rewrite the integrals in equation 1.2 in such a way that pressure is not explicitly needed and in this way extending the impulse approach. Unal et al.
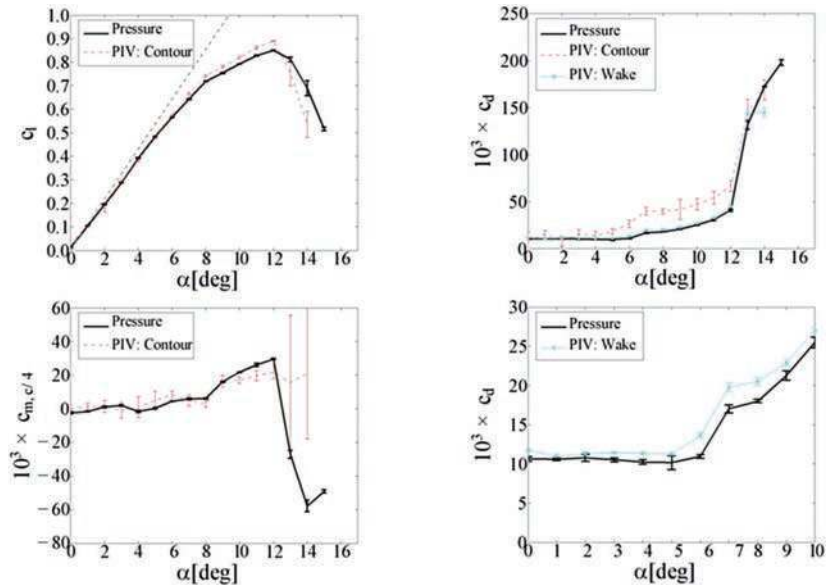
Figure 1.3: Time-averaged forces determined from PIV compared with forces determined from surface and wake pressure measurements (van Oudheusden et al. 2008).

(1997) apply this method to a computational and experimental comparison. Birch & Dickinson (2003) and Birch et al. (2004) show the application of the extended impulse approach on a flapping wing, showing influences of wing wake and leading edge vortex contributions, respectively.

Using an explicit determination of the pressure along a contour, van Oudheusden et al. (2006), van Oudheusden et al. (2007), and van Oudheusden et al. (2008) show various applications of force determination from PIV ranging from average forces on an aerofoil in incompressible flow (see figure 1.3) and in supersonic flow to time-averaged forces on a square cylinder. Ragni et al. (2009) determines time-averaged forces on an aerofoil in transonic flow. Kurtulus et al. (2007) use a time-resolved PIV system to determine unsteady local (sectional) forces on a square cylinder. David et al. (2009) apply time resolved PIV to determine the
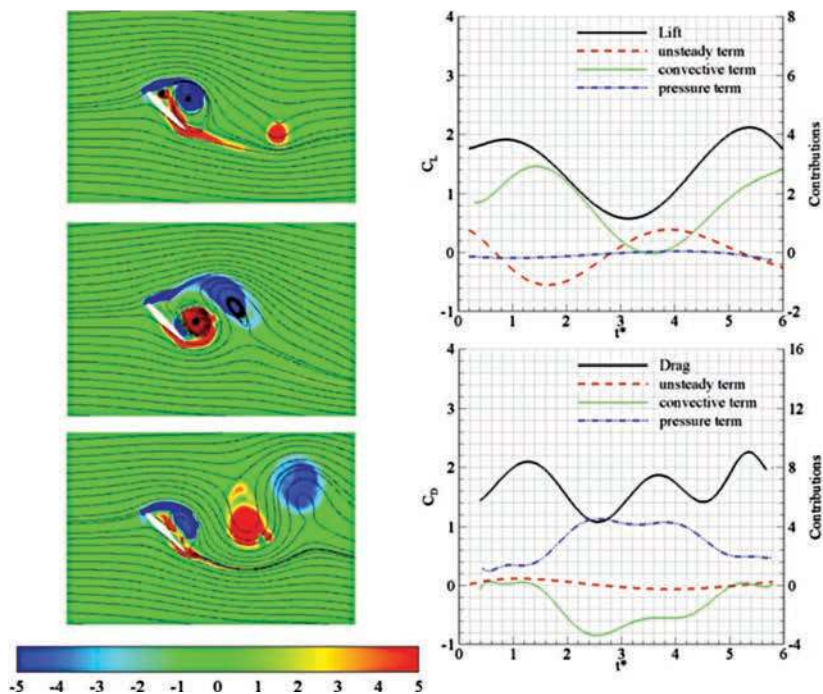
Figure 1.4: Instantaneous forces on a 2D wing (David et al. 2009). *Left*: three vorticity fields at different time instances. *Right*: time evolution of the force and the different contributions to the force.

instantaneous forces on a flapping two-dimensional (2D) wing, see figure 1.4

With the explicit calculation of the pressure, the (relative) importance of this term can be determined with respect to the advective momentum and acceleration terms. As seen in figure 1.4 the pressure has an important role in the drag determination, largely balancing with the advective (convective) term. For the lift determination, the pressure contribution is almost nonexistent. On the other hand, van Oudheusden et al. (2007) show that for their choice of control volume (closer to the aerofoil) the contribution of the pressure to the lift and drag were 83% and 92%, respectively. The amount to which the pressure along the contour will contribute therefore seems to be largely dependent on

the contour taken. This is not surprising, since the lift and drag can be determined by the integration of the pressure and friction forces along the surface of the body. For correct determination of the forces on bodies immersed in a fluid, the pressure is therefore important, whether one explicitly or implicitly uses its contribution.

Now we turn our attention to the pressure field itself. Gurka et al. (1999) derived from a steady velocity field the pressure distribution in a channel flow. Concurrently, Baur & Köngeter (1999) explored determination of instantaneous pressure from time-resolved data, addressing the local pressure reduction in the vortices shed from a wall-mounted obstacle, using a 2D approach. Hosokawa et al. (2003) used PIV-data to obtain the pressure distribution around single bubbles, while Fujisawa et al. (2005) derived pressure fields around and fluid forces on a circular cylinder. Liu & Katz (2006) show the application of pressure determination from PIV on a cavity flow. Fujisawa et al. (2006) apply pressure reconstruction on a micro channel using micro-PIV data. Pressure evaluation from PIV-data has even found its extension into the compressible regime as demonstrated by van Oudheusden (2008).

Haigermoser (2009) shows the application of the method of Liu & Katz (2006) to predict the acoustic emission using a rectangular cavity in water. Koschatzky et al. (2011) extends the use of acoustic emission prediction to air and compares the results to microphone measurements.

Several studies have explored the possibility to obtain the pressure field and have assessed the impact of using different methods (Eulerian or Lagrangian, i.e. fixed and moving reference frame) to determine the fluid acceleration and the subsequent integration of the pressure gradient, as well as the effect of the most important experimental parameters (notably spatial and temporal resolution and noise).

Charonko et al. (2010) compare different approaches in a Eulerian basis applied on two ideal sample flow fields and show an application to an oscillating flow in a diffuser. They investigate the influence of temporal and spatial resolution, but do not include the filtering effect that PIV has on both the velocity-field and the measurement noise (in combination with overlap this will lead to correlated noise, whereas they use uncorrelated noise). Violato et al. (2011) compare a Eulerian approach with a Lagrangian approach on a rod-aerofoil configuration and found that the Lagrangian approach is less prone to measurement noise.
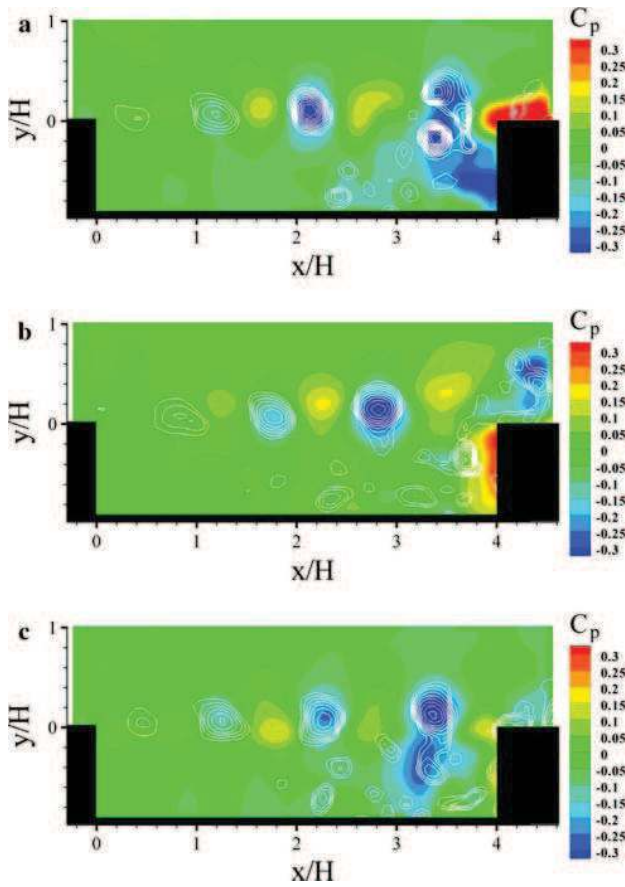
Figure 1.5: Pressure fluctuations in a rectangular cavity derived from PIV (Haigermoser 2009).
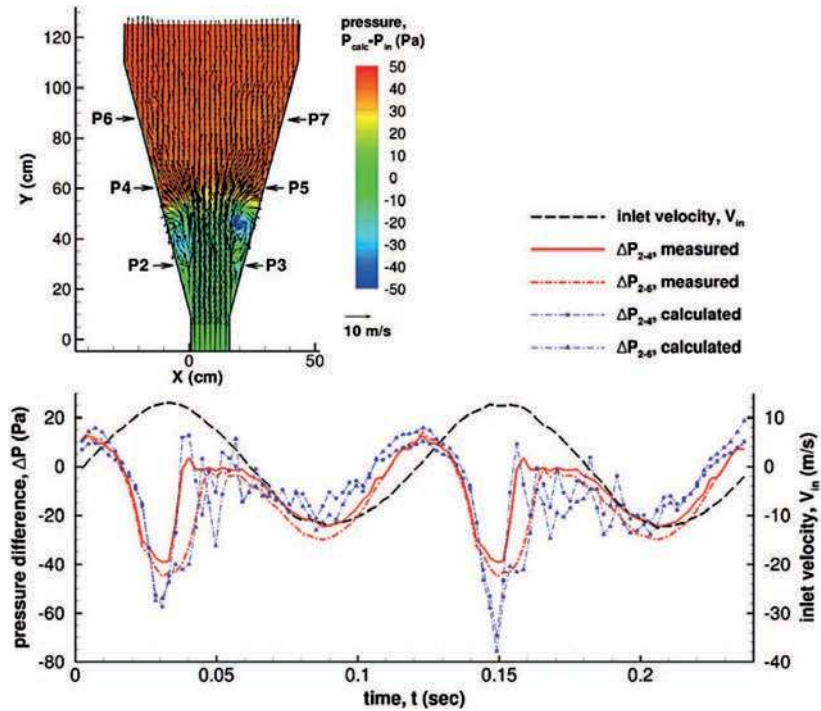
Figure 1.6: Instantaneous pressure derivation from PIV in a diffusor (Charonko et al. 2010). *Top*: instantaneous pressure field. *Bottom*: instantaneous pressure from PIV compared with phase-averaged transducer measurements.

Christensen & Adrian (2002) found that for their advecting turbulence
experiment the material acceleration was about one order of magnitude
smaller than the time change of the velocity at one point, which would
also promote the use of a Lagrangian approach. On the other hand,
Jakobsen et al. (1997) found that, for waves impinging on a vertical
wall, their Lagrangian approach had limitations and showed bias ef-
fects, resulting in a worse performance than their Eulerian approach.
These contradictory results show the need of a direct comparison of the
two approaches.

1.3   Square cylinder flow

As an experimental test bed for the pressure determination we have
adopted the square cylinder. This is a relatively simple and well docu-
mented flow geometry and time-averaged forces and pressure field un-
der similar flow conditions have been determined by van Oudheusden
et al. (2007), see figure 1.7.

However, it is well know that this wake flow is highly unsteady
(due to vortex shedding) and that at higher Reynolds numbers (larger
than 160, Luo et al. 2007) the wake behind square cylinders becomes
three-dimensional (3D). Figure 1.8 shows that for $Re_D = 155$ the wake
is still 2D, but for $Re_D = 188$ and higher Reynolds numbers the wake is
clearly 3D.

Computation by Sheard et al. (2009) showed similar structures as
depicted in figure 1.9. For increasing Reynolds numbers the complexity
(and therefore the three-dimensionality) of the flow is only expected
to increase. So far computational restrictions have stopped DNS from
reaching moderate to high values of Reynolds numbers (e.g 10,000 and
higher).

LES has potential for reaching higher Reynolds numbers, but is lim-
ited by the assumptions made by the modelling of the smallest scales,
where it is still unclear how these small scales behave. Nevertheless
LES calculations can give us an idea of what we can expect for the
large scales. Farhadi & Rahnama (2005) performed LES calculation
on the flow around a square cylinder at a Reynolds number of 22,000.
Figure 1.10 show the results they obtained and, here, the 3D nature of
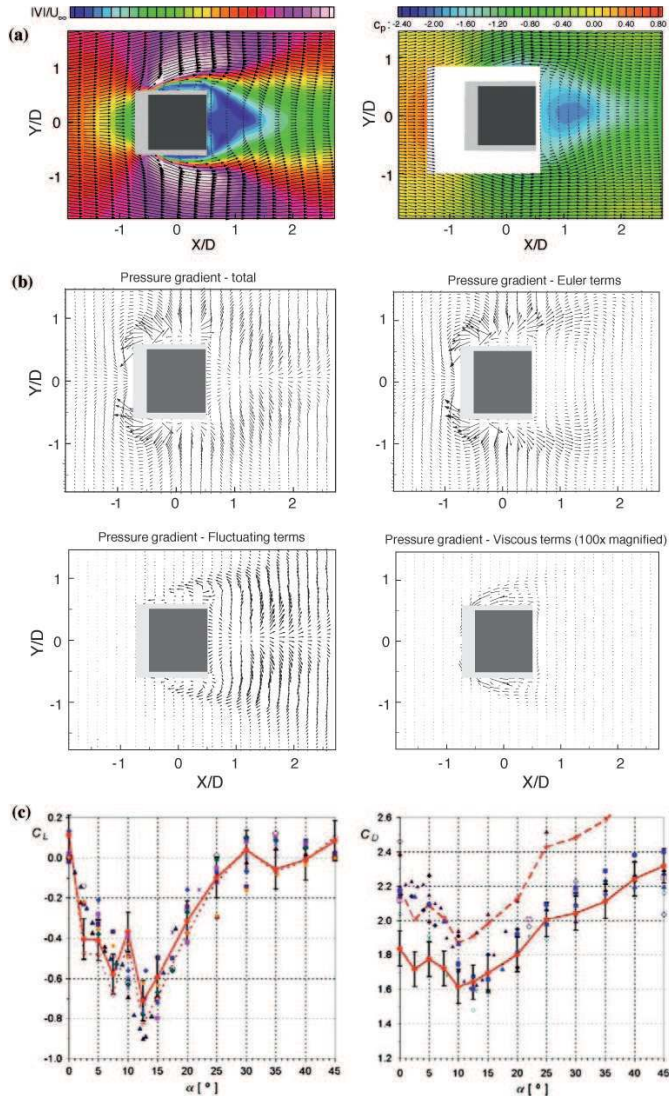
Figure 1.7: Time-averaged forces on and pressure field around a square cylinder at $Re_D = 10{,}000$ (van Oudheusden et al. 2007). (*a*) Velocity magnitude and pressure field. (*b*) Different contributions to the pressure gradient. (*c*) Lift and drag forces with α.
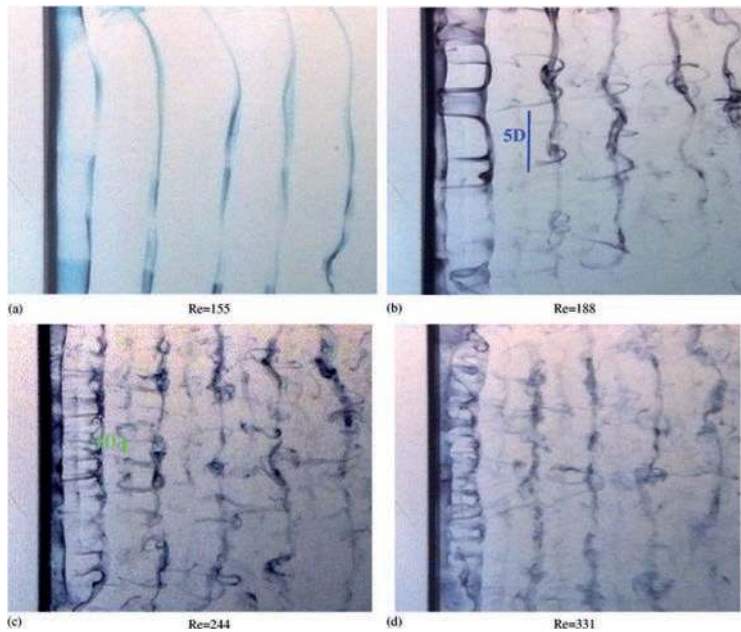
Figure 1.8: Dye visualizations of a square cylinder wake at different Reynolds numbers. 3D instabilities are clearly present from $Re_D = 188$ (Luo et al. 2007).
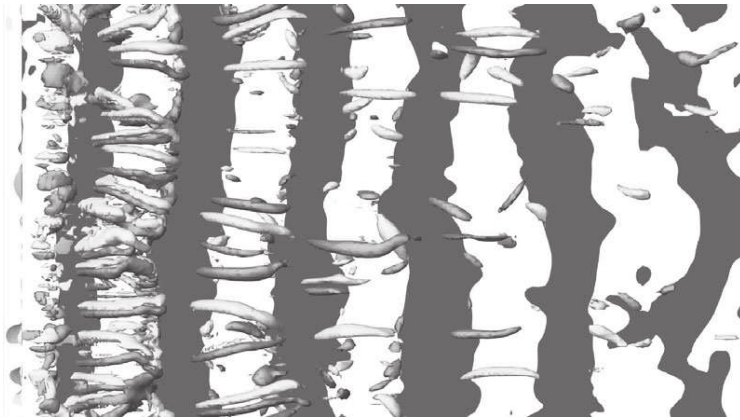
Figure 1.9: DNS calculation of the three-dimensional structure of the wake behind a square cylinder at $Re_D = 300$. The vortex street is identified by contours of (white) positive and (black) negative out-of-plane velocity plotted on the $y = 0$ plane. Isosurfaces of streamwise vorticity with levels $\pm 1U/D$ are shaded light and dark. Flow is from left to right and, the cylinder (not shown) is located at the left. (Sheard et al. 2009).
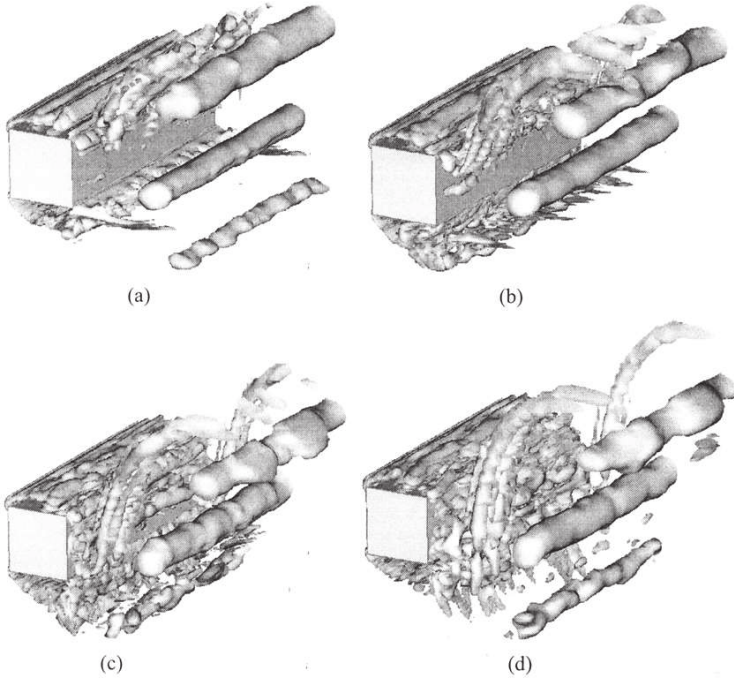
Figure 1.10: LES calculation of the flow around a square cylinder, Re_D = 22,000. Instantaneous isocontours of the second invariant of velocity gradient, Q (Farhadi & Rahnama 2005).

the flow is also readily apparent.

For Reynolds numbers of 5,000 to 20,000 the flow shear-layer separating from the leading edge of the square cylinder starts to develop Kelvin-Helmholtz type instabilities along the side of the cylinder. To quantify and describe the flow around a square cylinder at these Reynolds numbers, we need to turn to experimental techniques. However, experiments come with their own problems, e.g. the control of the boundary conditions, and limitations, e.g. no (instantaneously) simultaneous full field velocity and pressure measurements. In this Reynolds number regime, there have been a few investigations looking into the large scale motions and into fluctuations around these large scale motions, see Durao et al. (1988), Lyn & Rodi (1994), Lyn et al. (1995), and van

Oudheusden et al. (2005). They focus on the large scale motions and their relation to turbulent quantities or their relation to angle of incidence. The relationship between the large scale motions, small scale motions and the pressure field has not yet been investigated.

1.4 Aims and objectives

So far, no method can instantaneously measure both the velocity and pressure field. Although several studies have explored the possibility to derive the pressure field from velocity data by use of the Navier-Stokes equations, relatively little attention has been given to systematic analysis of experimental aspects that determine the accuracy of the pressure determination. Essential elements are the spatial and temporal resolution of the velocity measurements, as well as the different approaches (Eulerian or Lagrangian) to determine the fluid acceleration and the subsequent integration of the pressure gradient.

Next to this, the velocity-data used as input is primarily obtained from planar PIV, therefore most of these studies are hampered by the restriction of 2D (average) flow or necessarily making 2D flow assumptions, where it is not obvious what the impact of this assumption can be. Also, no complete comprehensive analysis of the experimental parameters (PIV settings, such as interrogation window-size, overlap-factor, etc.) that will determine the success of pressure-PIV has been reported yet.

Furthermore, previous efforts to validate the pressure determination have given little attention to advecting vortices, whereas they are characteristic features occurring in many fluid dynamic problems (e.g. turbulence, vortex shedding). Also a direct experimental validation for instantaneous pressure is still lacking.

The aim of this work is to assess the performance of a Eulerian and Lagrangian approach in pressure determination for turbulent flows. First the operating principles are introduced together with theoretical considerations to estimate frequency response (both truncation and precision effects) and expected limitations of the approaches. Next, the different approaches are tested on a synthetic flow field, an advecting Gaussian vortex, from which influences of different flow parameters

are determined (e.g. advective velocity, vortex strength). From both the theoretical considerations and the assessment on the synthetic flow field, conclusions regarding the proper application of the approaches will be drawn. To show experimental viability of pressure evaluation methods, stereoscopic PIV (stereo-PIV) and tomographic-PIV (tomo-PIV) experiments on a square cylinder are performed, employing surface pressure data for validation. Pressure dominated flows around bluff bodies pose relevant and challenging test-cases for pressure evaluation from planar-PIV, due to the complex time-evolving three-dimensional (3D) nature of the flow field, especially at moderate to high Reynolds numbers (see e.g. Williamson 1996). Furthermore the use instantaneous pressure determination from PIV allows for describing the link between velocity and pressure.

1.5   Outline

Starting with some fundamental concepts that support the understanding of the following analyses are given in chapter 2. The basics of PIV are explained in chapter 3. Chapter 4 explains in detail how to derive pressure from PIV velocity data. The performance of pressure-PIV is assessed on a synthetic flow field in chapter 5. The experimental arrangement and procedures are given in chapter 6, followed by the assessment of pressure-PIV on the square cylinder flow in chapter 7. Chapter 8 describes the pressure around and loading on a square cylinder, highlighting the link between velocity and pressure. Finally, the work will be summarised and conclusions will be drawn in chapter 9

The theory and findings that are covered in chapters 4-7 have been published in *Exp. Fluids* (de Kat & van Oudheusden 2011).

Chapter 2

Terminology & tools

Before we embark on a journey exploring the determination of pressure from PIV and exploring the flow around a square cylinder at a (moderate to) high Reynolds number, we need to ascertain a theoretical foundation to properly convey the points that will be made. First, some terminology, like the reference frame, is defined. Next, a description of data analysis procedures is given. Finally, the principles of the uncertainty analysis used throughout this thesis is described.

2.1   Terminology

The reference system is a stationary cartesian coordinate system with x-, y-, and z-coordinates indicating the directions. The x-direction is in streamwise direction. The velocity components are u, v, and w in x-, y-, and z-direction, respectively.

Equation 1.1 gives two different ways of looking at the change of momentum. We can either follow a fluid parcel and look at the change of momentum it experiences (as expressed by the material acceleration) or we can look at a fixed point in space and observe the acceleration of the fluid in and the advection of momentum through this point. These two different ways of looking at the change of momentum are generally referred to as a Lagrangian and a Eulerian reference frame of the momentum, respectively. As described in the introduction these different ways of looking at the momentum change have different consequences

in their interpretation.

Another issue with the flow equations is that they are posed in a continuous form, whereas experimental data is generally acquired in points and therefore have a discrete nature, e.g. PIV results are grids with a finite number of vectors instead of a continuous description of the flow.

The analysis in this thesis assumes spatially uniform spaced grids, i.e. $\Delta x = \Delta y = \Delta z = h$. However, all procedures can be easily extended to nonuniform spaced grids.

Derivatives of discretely sampled data can be approximated by the technique of finite differences. Consider the Taylor expansion in time for function f:

$$f(\mathbf{x}, t + \Delta t) = f(\mathbf{x}, t) + \frac{\partial f}{\partial t}(\mathbf{x}, t)\Delta t + \ldots + \frac{\partial^n f}{\partial t^n}(\mathbf{x}, t)\frac{\Delta t^n}{n!}, \quad (2.1)$$

for $n \to \infty$. This expansion can be used to derive estimates for the gradient (in time or space). One common estimate of the gradient (here in time) is the central finite difference, given as

$$\frac{\partial f}{\partial t}(\mathbf{x}, t) \approx \frac{f(\mathbf{x}, t + \Delta t) - f(\mathbf{x}, t - \Delta t)}{2\Delta t}, \quad (2.2)$$

which is obtained taking the difference between the Taylor expansion for $t + \Delta t$ and $t - \Delta t$ and neglecting higher order derivatives (second order and higher).

The pressure coefficient, C_p, is defined to be

$$C_p = \frac{p - p_\infty}{\frac{1}{2}\rho U^2}, \quad (2.3)$$

where p is the local pressure, p_∞ is the free-stream pressure, ρ the density, and U the free-stream velocity.

2.2   Data analysis procedures

2.2.1   Statistical tools

Time-average

A time-dependent quantity under investigation, say the velocity field $u(\mathbf{x},t)$, may decomposed into

$$u(\mathbf{x},t) = \overline{u}(\mathbf{x}) + u'(\mathbf{x},t), \tag{2.4}$$

where $\overline{u}(\mathbf{x})$ is the (global) long-time-averaged velocity and $u'(\mathbf{x},t)$ is the fluctuating velocity around the time-average. The time-averaged component is formally defined by

$$\overline{u}(\mathbf{x}) = \lim_{T \to \infty} \frac{1}{T} \int_0^T u(\mathbf{x},t)\, \mathrm{d}t, \tag{2.5}$$

where T is the length of the time-series data. Practically, an ensemble-average of a discrete time-series signal is determined by

$$\langle u(\mathbf{x}) \rangle = \frac{1}{N} \sum_{n=1}^N u(\mathbf{x},t_n), \tag{2.6}$$

which for a (on average) stationary flow is equal to the time-average, $\overline{u}(\mathbf{x}) = \langle u(\mathbf{x}) \rangle$. Note that the notation used to indicate the ensemble-average is only used as such here. Further on in this thesis, this notation is reserved for a phase-average (which is a special case or an ensemble-average).

In analogous manner the spatial average can be determined.

Root-mean-square

To indicate the fluctuations around the (time-)average a common measure is the root-mean-square (RMS). For the temporal fluctuations around the time-average it is defined by

$$\sigma_u(\mathbf{x}) = \sqrt{\frac{1}{N} \sum_{n=1}^N (u(\mathbf{x},t_n) - \overline{u}(\mathbf{x}))^2} = \sqrt{\frac{1}{N} \sum_{n=1}^N (u'(\mathbf{x},t_n))^2}. \tag{2.7}$$

In analogous manner the spatial RMS can be determined.

(Co)variance

The covariance of two signals, f and g, is defined as

$$\operatorname{cov}(f,g) = \frac{1}{N} \sum_{n=1}^{N} f_n' g_n'. \qquad (2.8)$$

The covariance of a signal with itself (variance) is equal to its RMS square:

$$\operatorname{var}(f) = \operatorname{cov}(f,f) = \sigma_f^2. \qquad (2.9)$$

Correlation coefficient

The correlation coefficient is a measure for alignment of the fluctuations of two signals around their respective means and is defined as:

$$\rho_c(f,g) = \frac{\operatorname{cov}(f,g)}{\sigma_f \sigma_g} \qquad (2.10)$$

It indicates whether the fluctuations (variance-contributions) of one signal are aligned with the fluctuations of the other signal (in time or space). However, it does not indicate anything about the (dis)similarity in amplitude of the two signals.

Power spectrum

To show the frequency content of a signal (in time or space) the power per frequency can be determined by determining the power spectrum. The power spectrum is defined as

$$P_{u'u'}(f) = Y_{u'}^*(f) Y_{u'}(f) \qquad (2.11)$$

where Y_u' is the Fourier transform of u' (as function in time or space) as a function of frequency f and $Y_{u'}^*$ its complex conjugate.

Co-spectrum

The co-spectrum is defined as

$$P_{u'v'}(f) = Y_{u'}^*(f) Y_{v'}(f) \qquad (2.12)$$

where $Y_{u'}^*$ is the complex conjugate of the Fourier transform of u' and $Y_{v'}$ the Fourier transform of v'.

Dynamic correlation

Normalising the co-spectrum with the respective power spectra results in the coherence, which is a measure for the amount the two signals match per frequency and also includes phase information in the imaginary part. Taking only the real part of the coherence gives information about the match between two signals at zero phase difference and this we define to be the dynamic correlation. The dynamic correlation is given by

$$\text{Dyn.Corr.} = \Re \left(\frac{P_{u'v'}}{\sqrt{P_{u'u'} P_{v'v'}}} \right) \tag{2.13}$$

It describes the match (correlation) between the signals per frequency.

2.2.2 Phase-averaging

As introduced by Hussain & Reynolds (1970), for certain phenomena, the fluctuating component, u', may be further decomposed into a periodic fluctuation and a random fluctuation around this periodic fluctuation, resulting in a triple decomposition

$$u(\mathbf{x},t) = \overline{u}(\mathbf{x}) + \tilde{u}(\mathbf{x},t) + \hat{u}(\mathbf{x},t), \tag{2.14}$$

where $\tilde{u}(\mathbf{x},t)$ is the periodic component with zero mean, and $\hat{u}(\mathbf{x},t)$ is the fluctuating velocity around the periodic component. The phase-average is the combination of the time-averaged and periodic components, such that

$$u(\mathbf{x},t) = \langle u(\mathbf{x}, \phi(t)) \rangle + \hat{u}(\mathbf{x},t), \tag{2.15}$$

where $\langle u(\mathbf{x}, \phi(t)) \rangle$ is the phase-averaged velocity at any point in space at a given phase $\phi(t)$. The phase-averaged velocity field is defined by

$$\langle u(\mathbf{x}, \phi(t)) \rangle = \frac{1}{N} \sum_{n=0}^{N-1} u(\mathbf{x}, \phi(t+n\tau)), \tag{2.16}$$

where τ is the period of the periodic component and $n\tau$ is the ensemble over which the phase-average is made. In this representation, phase-averaging is akin to Reynolds-averaging, except that the averaging is performed over an ensemble $n\tau$ rather than the complete data.

2.2.3   Phase determination

For phenomena where the periodicity is enforced (e.g. by being driven with a prescribed frequency) the phase determination is quite obvious. However, for natural occurring quasi-periodic phenomena (like vortex shedding), there can be significant frequency and amplitude modulations throughout time. A relatively simple and robust method of identifying the phase variable can be found using the Hilbert transform (see Huang et al. 1998). A major advantage of the Hilbert transform is that it constructs an analytic signal from the measured one, thereby providing the amplitude and phase variables directly. It thereby constitutes an unambiguous and robust method of determining $\phi(t)$. In the Hilbert approach, the Hilbert transformation $H\{p(t)\}$ of the signal $p(t)$ is formally defined as

$$H\{p(t)\} = \frac{1}{\pi} P \int_{-\infty}^{\infty} \frac{p(\tau)}{t - \tau} \mathrm{d}\tau, \qquad (2.17)$$

where P is the Cauchy principal value defined by

$$P = \int_{-\infty}^{\infty} f(x) \mathrm{d}x \equiv \lim_{R \to \infty} \int_{-R}^{R} f(x) \mathrm{d}x. \qquad (2.18)$$

The Cauchy principal value is required because of the possibility of a singularity in $H\{p(t)\}$ at $t = \tau$. With the definition of the Hilbert transform, $H\{p(t)\}$ and $p(t)$ form a complex conjugate pair, such that we can define a (complex) analytic signal $Z(t)$ using

$$Z(t) = p(t) + iH\{p(t)\}, \qquad (2.19)$$

where i is the imaginary number ($i^2 = -1$). To introduce the phase variable $\phi(t)$, we recast the analytic signal in terms of exponential notation by writing

$$Z(t) = a(t)e^{i\phi(t)}, \qquad (2.20)$$

where $a(t)$ is the amplitude and $\phi(t)$ is the phase of the analytic function. These are given respectively by

$$a(t) = \sqrt{p(t)^2 + H\{p(t)\}^2}, \tag{2.21}$$

$$\phi(t) = \tan^{-1}\left(\frac{H\{p(t)\}}{p(t)}\right). \tag{2.22}$$

Thus, in this representation, the analytic function is nothing more than a local fit of an amplitude and phase varying trigonometric function to $p(t)$ (see Huang et al. 2003), and we therefore have a suitable method for determining $\phi(t)$ that can cope with modulation in frequency and amplitude.

2.3 Uncertainty analysis

2.3.1 Statistical uncertainty estimation

Benedict & Gould (1996) describe how to estimate the uncertainty of turbulence statistics, such as mean and RMS values derived from an ensemble of N uncorrelated observations. The uncertainty on the mean can be expressed as

$$\varepsilon_{\overline{u}} = \frac{\sigma_u}{\sqrt{N}} \tag{2.23}$$

The uncertainty on the RMS can be expressed as

$$\varepsilon_{\sigma_u} = \frac{\sigma_u}{\sqrt{2N}} \tag{2.24}$$

The uncertainty on the variance can be expressed as

$$\varepsilon_{\overline{u'^2}} = \frac{2\sigma_u^2}{\sqrt{2N}} \tag{2.25}$$

The uncertainty on the covariance can be expressed as

$$\varepsilon_{\overline{u'v'}} = \frac{\sqrt{1 + \rho_c(u,v)}\sigma_u\sigma_v}{\sqrt{N}}, \tag{2.26}$$

where the uncertainty on the correlation coefficient can be expressed as

$$\varepsilon_{\rho_c(u,v)} = \frac{1 - \rho_c(u,v)}{\sqrt{N}}.$$

(2.27)

2.3.2   Linear uncertainty propagation

Following the basis principles of linear uncertainty propagation as laid down by Kline & McClintock (1953) (for a detailed explanation, see Stern et al. 1999), one can estimate the uncertainty of a single sample measurement based on the uncertainties of the measurement techniques on which it is based. If a value of a quantity y depends on a series of n uncorrelated variables x, such that

$$y = f(x_1, x_2, \ldots, x_n),$$

(2.28)

then its uncertainty can be estimated as

$$\varepsilon_y = \sqrt{\left(\frac{\partial f}{\partial x_1}\varepsilon_{x_1}\right)^2 + \left(\frac{\partial f}{\partial x_2}\varepsilon_{x_2}\right)^2 + \ldots + \left(\frac{\partial f}{\partial x_n}\varepsilon_{x_n}\right)^2},$$

(2.29)

where $\partial f/\partial x_n$ is the sensitivity coefficient of f with respect to x_n and ε_{x_n} is the uncertainty to the measurement of x_n.

To illustrate the use of this approach the uncertainty of the spatial gradient in x-direction $\varepsilon_{\partial f/\partial x}$ of the function f with uncertainty ε_f is estimated. The central finite difference equation

$$\frac{\partial f}{\partial x} = \frac{f(x + \Delta x) - f(x - \Delta x)}{2\Delta x},$$

(2.30)

gives the following sensitivity coefficients

$$\frac{\partial(\partial f/\partial x)}{\partial f(x + \Delta x)} = \frac{1}{2\Delta x},$$

(2.31)

$$\frac{\partial(\partial f/\partial x)}{\partial f(x - \Delta x)} = -\frac{1}{2\Delta x}.$$

(2.32)

This results in the uncertainty estimate to be

$$\varepsilon_{\partial f/\partial x} = \frac{\sqrt{2}}{2}\frac{\varepsilon_f}{\Delta x}.$$

(2.33)

Chapter 3

Particle image velocimetry

This chapter aims at setting out the basics of PIV and the implementations used in this thesis. This knowledge is a prerequisite to understanding the value of the extension of the method to deriving pressure from the PIV velocity data. Detailed studies have been performed on the workings of PIV and all its implementations and deeper understanding is still created in ongoing research. Interested readers are referred to Raffel et al. (2007) and references therein for further reading.

3.1   General working principles

PIV is an imaging based measurement method that uses tracer particles. A schematic representation of a PIV setup is depicted in figure 3.1. It consists of a laser system with laser optics to create a laser-light sheet, light-scattering tracer particles in the flow, and a lens-camera combination (imaging optics and image plane) to record the location of the particles at different times. PIV is a non-intrusive technique when it uses tracer particles that (1) do not influence the flow, (2) follow the flow exactly, and (3) do not interact with each other (Westerweel 1997). Although these requirements cannot be met completely, PIV is generally considered a non-intrusive technique.

Using tracer particles is an inherently Lagrangian measurement of the fluid flow, where we have no control over what path the particles will take (this is purely dictated by the flow around the particle) and
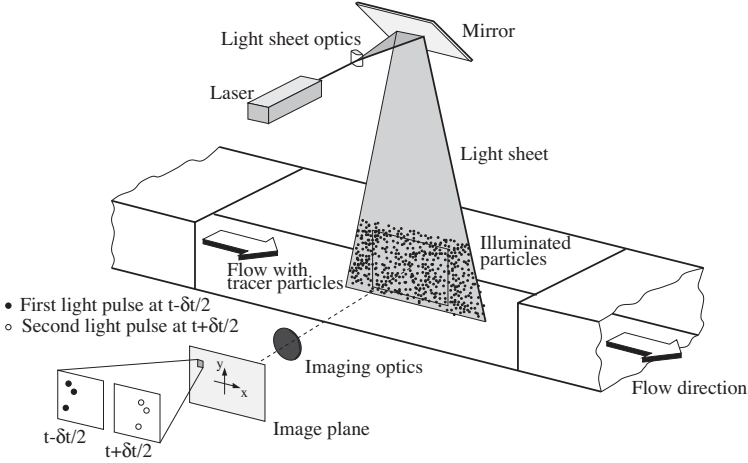
Figure 3.1: Schematic representation of a PIV-setup. Modified from Raffel et al. (2007)

therefore what areas of the flow will be covered during measurement (for an insightful essay, see Price 2006). The only way to measure the complete region of interest is to have enough particles and let the flow take them everywhere we want to measure. The particles are illuminated by a laser-light sheet and subsequently captured by a digital camera. The camera records two images within a short time interval (laser-pulse separation, δt). The displacement of the particles between the two recordings can be used to determine the velocity of particle using a (central) finite difference

$$\mathbf{u}_p\left(t\right) = \frac{\mathbf{x}_p\left(t + \delta t/2\right) - \mathbf{x}_p\left(t - \delta t/2\right)}{\delta t} + O\left(\delta t^2\right), \qquad (3.1)$$

where $\mathbf{u}_p$ is the particle velocity and $\mathbf{x}_p$ the particle location. The location where the particle has this velocity is estimated to be

$$\mathbf{x}_p\left(t\right) \approx \frac{\mathbf{x}_p\left(t + \delta t/2\right) + \mathbf{x}_p\left(t - \delta t/2\right)}{2}. \qquad (3.2)$$

Instead of applying this principle to each particle image pair individually and afterwards interpolating the velocity field onto a carte-

sian grid, PIV uses a statistical analysis technique, cross-correlation, to determine the (average) displacement of a group of particles images within an interrogation window. This approach has the advantages that it can be applied such that no explicit particle detection is required and that no additional interpolation is needed to represent the results on a cartesian grid. The resulting field can represent the Eulerian velocity field, since at a given point in space and moment in time the Eulerian and Lagrangian velocities are the same.

3.1.1 Tracer particles

The (non-)intrusiveness of PIV and the accuracy with which the particles follow the flow is primarily influenced by the choice of tracer particles. The particles need to be large enough to scatter enough light for imaging, but small (and light) enough to follow the flow. Melling (1997) describes an estimate for the response of heavy particles in air to be

$$\frac{\mathrm{d}\mathbf{u}_p}{\mathrm{d}t} = C\left(\mathbf{u}_f - \mathbf{u}_p\right),\qquad(3.3)$$

where $\mathbf{u}_p$ is the particle velocity, $\mathbf{u}_f$ is the fluid velocity (at the particle location) and C is the characteristic frequency of the particle motion, which can be estimated using Stokes drag law as

$$C = \frac{18\mu_f}{\rho_p d_p^2},\qquad(3.4)$$

where μ_f is the fluid viscosity, ρ_p is the particle density and d_p is the particle diameter. The frequency response of the particles in a fluctuating (turbulent) flow can be estimated using the characteristic frequency and

$$\frac{\overline{u_p^2}}{\overline{u_f^2}} = \left(1 + \frac{\omega_c}{C}\right)^{-1},\qquad(3.5)$$

where ω_c is the highest frequency of interest.

Melling (1997) indicates that for a frequency response of 10 kHz in air the particle diameter should not exceed 1μm. More recent work

by Ragni et al. (2010) shows that particle smaller than 1 μm have a frequency response exceeding 10 kHz (up to 500 kHz).

3.1.2   Particle imaging

The image of the tracer particles is focussed on an imaging plane using photographic lenses. Starting from Gauss's lens formula (assuming all lenses are thin and all angles are small)

$$\frac{1}{f} = \frac{1}{z_0} + \frac{1}{Z_0}, \tag{3.6}$$

where f is the focal length of the lens, z_0 is the image plane distance to the lens and Z_0 is the object distance to the lens. Next we define the magnification, M, and the focal ratio or f-number, $f_\#$, to be

$$M = \frac{z_0}{Z_0}; \quad f_\# = \frac{f}{D_a}, \tag{3.7}$$

where D_a is the aperture diameter of the lens. It is fairly straight forward to show that the depth of field, δ_z, is

$$\delta_z = \frac{2f_\# c\,(M+1)}{M^2 - \left(\frac{f_\# c}{f}\right)^2} \approx 2f_\# c\frac{M+1}{M^2}, \tag{3.8}$$

where c is the circle of confusion. A schematic drawing of this is shown in figure 3.2. The second term in the denominator can be neglected, since for PIV purposes it is very small compared to the magnification term.

   Finite aperture lenses are diffraction limited. This means that point sources will show up as Airy disk and rings on the imaging plane (see Raffel et al. 2007). The size of this disk, d_{diff} can be estimated by

$$d_{diff} = 2.44 f_\# \lambda\,(M+1), \tag{3.9}$$

where λ is the wavelength of the the light passing through the lens. The minimal image-size of a particle (for an aberration-free lens) now becomes

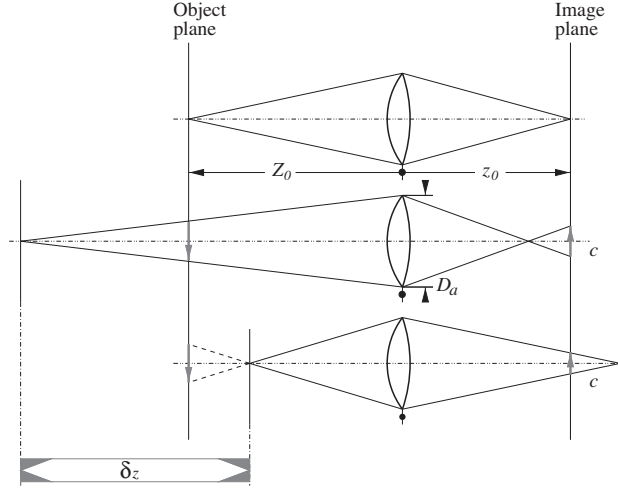$$d_\tau = \sqrt{(Md_p)^2 + \left(d_{diff}\right)^2}, \tag{3.10}$$

Figure 3.2: Schematic representation of depth of field. Modified from Raffel et al. (2007)

for small particles this means $d_\tau \approx d_{diff}$.

Typically the circle of confusion is determined by the desired print size and viewing distance of an image combined with an estimate for human visual acuity. However, for digital sensors it is more straightforward to use the pixel pitch as the circle of confusion. In PIV the d_{diff} (aimed to be 2-3 pixels) is generally used to estimate the depth of field and the estimate of δ_z becomes

$$\delta_z = 4.88 f_\#^2 \lambda \left(\frac{M+1}{M} \right)^2. \tag{3.11}$$

For experiments λ is determined by the laser, d_p is determined by the desired frequency response and M the desired field-of-view, leaving $f_\#$ as only adjustable parameter. Using $f_\#$ to optimize the particle image size is important for the accuracy of PIV, since the error in velocity measurement and the amount of light captured on the sensor depend on it (see Raffel et al. 2007).

3.1.3   Image analysis

Only the basic operating principle of cross-correlation is explained. For a more detailed description the reader is referred to Raffel et al. (2007).

The process is illustrated in figure 3.3. First, the particle images recordings are divided into smaller regions, the interrogation windows. Next, these smaller regions are cross-correlated with the corresponding interrogation window, one for time instant $t + \delta t/2$ and one or time instant $t - \delta t/2$. The basic cross-correlation approach determines the covariance of the overlap of the interrogation windows for different integer pixel-shifts. The maximum of this cross-correlation map is the most likely displacement. However, this approach can introduce a bias error due to the changing overlap between the two interrogation windows and differences between the two laser-pulses. The bias can be corrected for by using a normalized cross-correlation approach, where the cross-correlation values are based on the correlation coefficient for each different shift.

$$\rho_{cc}(\delta \mathbf{s}) = \rho_c \left(I\left(WS, t - \delta t/2\right), I\left(WS + \delta \mathbf{s}, t + \delta t/2\right)\right), \qquad (3.12)$$

where WS indicates the interrogation window area and $\delta \mathbf{s}$ is the shift of the interrogation window. The velocity is then determined using the displacement corresponding to the maximum correlation, $\delta \mathbf{s} = \delta \mathbf{s}|_{max(\rho_{cc})}$ and the laser-pulse time separation

$$\mathbf{u} = \frac{\delta \mathbf{s}}{\delta t}, \qquad (3.13)$$

This procedure is repeated for all interrogation windows.

Subpixel accuracy can be achieved by applying a three-point Gaussian fit or by finding the centroid of the correlation peak. Where the former is less sensitive to pixel-locking (see Raffel et al. 2007). The accuracy can further be improved by applying iterative window deformation techniques (see e.g. Scarano & Riethmuller 2000, Schrijer & Scarano 2008), which not only increase the subpixel accuracy, but also reduces the spatial modulation of the cross-correlation technique.

To give more assurance on the validity of a vector validation a median filter can be applied (see Westerweel & Scarano 2005). The median filter compares the difference of the vector to be validated with

(*a*) Recording

t-δt/2 t+δt/2

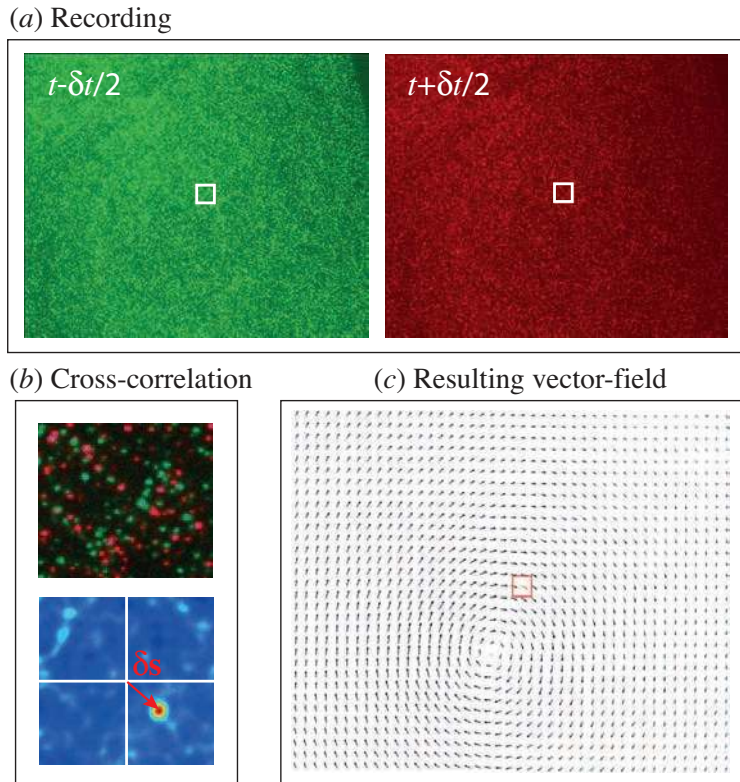(*b*) Cross-correlation (*c*) Resulting vector-field

δs

Figure 3.3: Schematic representation of the cross-correlation procedure. Coloring of the particle images has no physical significance and is purely for clarity. Modified from de Kat (2007)
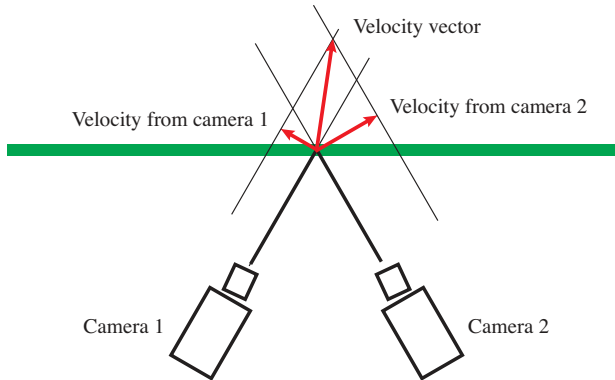
Figure 3.4: Schematic representation of a stereoscopic-PIV setup.

its neighbouring vectors to the RMS of the neighbouring vectors. If
this difference is larger than three times the RMS of the neighbouring
vectors the vector is generally rejected.

3.1.4   Calibration

Following the work of Soloff et al. (1997), images can be corrected
for off-axis viewing, lens-abberations, and imperfect optical windows
using a third order polynomial fit. The calibration procedure consists of
aligning a calibration target with the laser-light sheet, taking images of
the calibration target, fitting the third order polynomial to the acquired
images, and correct the images. The calibration target typically consists
of a black metal plate with white dots or crosses at a know distribution.
Using the knowledge of the physical (relative) locations of the dots,
the image plane coordinates (x_i, y_i) mapping onto a physical coordinate
system (X, Y, Z) can be determined.

3.2   Stereoscopic-PIV

The basic PIV setup gives us a two component velocity field in the
laser sheet plane. If we now also want to know the third component
of the velocity we can add a camera to the setup to make the setup

stereoscopic. The two cameras both look at the measurement plane at a different angle, therefore 'seeing' a different projection of the particle displacement. This translates into different projections of the velocity as shown in figure 3.4. With these two projections the three components of the real velocity can be reconstructed using the viewing angles of the cameras (Prasad 2000). Two parallel calibration planes are needed to incorporate the viewing angle into the equations for the reconstruction.

An interesting use of having (a minimum of) two cameras is that the calibration can be improved using the fact that both cameras look at the same particles at the same time. Using this extra information from multiple views can reduce the calibration error significantly, see e.g. Wieneke (2005).

One minor disadvantage of stereo-PIV is the loss of image area due to the back projection of the recordings on the measurement plane (Willert 1997), as the views of the two cameras on the measurement plane do not overlap completely.

3.3 Tomographic-PIV

In tomographic-PIV the particles are captured by multiple cameras (typically four), then reconstructed in 3D using a tomographic reconstruction technique and then the resulting 3D light intensity distributions are correlated to obtain a volume with 3D velocity information (Elsinga et al. 2006). This process is illustrated in figure 3.5.

The 3D light-intensity distributions is reconstructed using the multiplicative algebraic reconstruction technique (MART, see Herman & Lent 1976). The relation between the 3D light-intensity distribution E and the image I is given by

$$I(x_i, y_i), = \sum_{j \in N_i} w_{i,j} E(X_j, Y_j, Z_j) \tag{3.14}$$

where $w_{i,j}$ is the weighting coefficient that describes the contribution of the jth voxel intensity $E(X_j, Y_j, Z_j)$ to the ith pixel intensity $I(x_i, y_i)$. N_i is the total number of voxels in the line-of-sight corresponding to the ith pixel. The 3D light-intensity distribution is solved for iteratively using
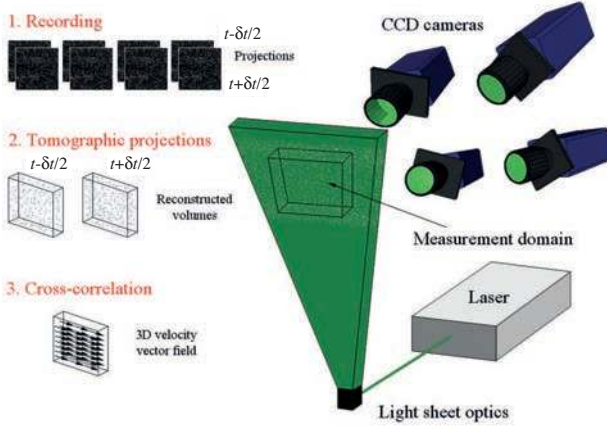
Figure 3.5: Schematic representation of the tomographic-PIV procedure. From Humble (2008), based on Elsinga et al. (2006)

$$E^{k+1}\left(X_j, Y_j, Z_j\right) = E^k\left(X_j, Y_j, Z_j\right) \times \left(\frac{I\left(x_i, y_i\right)}{I^k\left(x_i, y_i\right)}\right)^{\mu w_{i,j}}, \qquad (3.15)$$

where $\mu \in (0,1)$ is a relaxation factor. A schematic represenation of the reconstruction process is shown in figure 3.6.

Similar to the planar self-calibration for stereo-PIV, the calibration of the volume for tomo-PIV can be improved using particle pairing and triangulation (see Wieneke 2008).

3.4 Uncertainty estimates

Following the methodology explained in §2.3, the uncertainty estimates of the statistical quantities are straightforward to determine. The uncertainty for the instantaneous results require some derivation. The uncertainty estimate for the instantaneous streamwise velocity component (as determined by equation 3.13) becomes
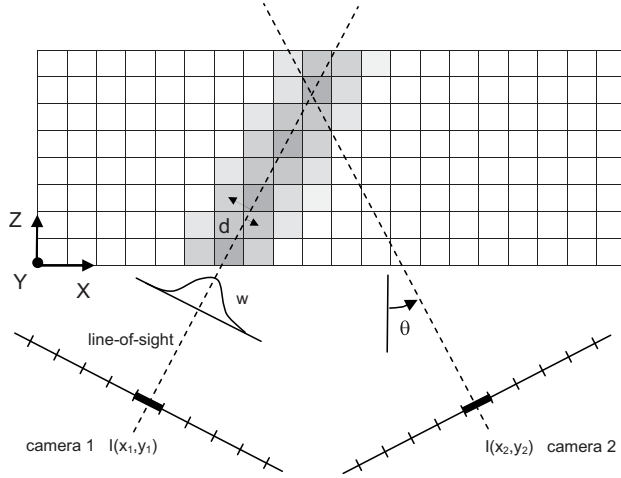
Figure 3.6: Schematic representation the tomopraphic reconstruction procedure. From Elsinga et al. (2006)

$$\varepsilon_u = \sqrt{\left(\frac{\varepsilon_{\delta x}}{\delta t}\right)^2 + \left(\frac{\delta x}{\delta t}\frac{\varepsilon_{\delta t}}{\delta t}\right)^2}, \qquad (3.16)$$

where $\varepsilon_{\delta x}$ is the uncertainty on the displacement in streamwise direction and $\varepsilon_{\delta t}$ the uncertainty on the time separation. The error on the time separation is generally small (can be estimated as the laser pulse width, which is small with respect to the laser pulse time separation).

Uncertainty in magnification influences $\varepsilon_{\delta x}$ and can be estimated by

$$\kappa = \frac{l_c}{n_c}; \quad \varepsilon_\kappa = \kappa\sqrt{\left(\frac{\varepsilon_{l_c}}{l_c}\right)^2 + \left(\frac{\varepsilon_{n_c}}{n_c}\right)^2}, \qquad (3.17)$$

where κ is the magnification, l_c the physical distance between calibration points, n_c the number of pixels spanning l_c, ε_κ is the uncertainty on the magnification, ε_{l_c} is the uncertainty on the distance between calibration points, and ε_{n_c} is the uncertainty on number of pixels. The value of ε_κ is generally very small (see e.g. Humble 2008).

Now, the uncertainty in the particle displacement can be estimated by

$$\varepsilon_{\delta x} = \sqrt{(\kappa \varepsilon_{cc})^2 + \left(\delta x \frac{\varepsilon_{\kappa}}{\kappa}\right)^2}, \tag{3.18}$$

where ε_{cc} is the uncertainty in the cross-correlation.

The uncertainty on the *x*-component of the gradient of the stream-wise velocity, when based on central finite differences (and neglecting the influence of ε_{κ}), can be estimated as

$$\varepsilon_{\partial u/\partial x} = \sqrt{2}\frac{\varepsilon_u}{2h}, \tag{3.19}$$

where h is the grid spacing (see equations 2.30 and 2.33).

The uncertainty on acceleration (similar as the uncertainty on the velocity gradient) follows directly from the central finite differencing uncertainty,

$$\varepsilon_{\partial u/\partial t} = \sqrt{2}\frac{\varepsilon_u}{2\Delta t}, \tag{3.20}$$

where Δt is the time separation between two successive velocity fields.

The uncertainty on the vorticity can be estimated using the uncertainties on the velocity gradient,

$$\varepsilon_{\omega_z} = \sqrt{\varepsilon_{\partial v/\partial x}^2 + \varepsilon_{\partial u/\partial y}^2}. \tag{3.21}$$

Chapter 4

Pressure from PIV

Pressure evaluation from PIV velocity data involves two steps. First, the pressure gradient is evaluated from locally applying the momentum equation in differential form. The second step is to spatially integrate the pressure gradient to obtain the pressure field. These steps can be performed in different ways, where each way has its own characteristics and associated limitations as will be described in this section.

4.1 Operating principle

The incompressible momentum equation can give the relation between the pressure gradient and the velocity data in two different forms: the Eulerian form and the Lagrangian form, given as

$$\nabla p = -\rho \left\{ \frac{\partial \mathbf{u}}{\partial t} + (\mathbf{u} \cdot \nabla) \mathbf{u} - \nu \nabla^2 \mathbf{u} \right\} \quad \text{or}$$

$$\nabla p = -\rho \left\{ \frac{D\mathbf{u}}{Dt} - \nu \nabla^2 \mathbf{u} \right\}, \tag{4.1}$$

respectively. $D\mathbf{u}/Dt$ is the material acceleration, $\partial \mathbf{u}/\partial t$ is the local acceleration, $\mathbf{u} \cdot \nabla$ the advective operator, ∇p the pressure gradient, μ the fluid viscosity, and $\nabla^2 \mathbf{u}$ the Laplacian of the velocity. Although the viscous term can be determined, its effect on the pressure gradient can generally be neglected and will therefore be omitted in the following discussion (see van Oudheusden et al. 2007, show found the vis-

cous contribution to be two orders of magnitude smaller for a similar Reynolds number).

In case of 2D flow, planar time-resolved PIV will suffice for determining the pressure gradients, but for 3D flow all components of the velocity and velocity-gradient are needed, which may be accomplished by a time-resolved tomo-PIV procedure, for example (see Schröder et al. 2008).

We will concentrate on the procedure to determine the pressure in a cross-sectional plane in the flow. To evaluate the pressure in the plane (here defined as the *x-y*-plane) only the two pressure gradient components in this plane are needed. The reader should note however that these in-plane pressure gradient components contain in- and out-of-plane components of the velocity and velocity-gradient.

To obtain the pressure, the pressure gradient can be spatially integrated using a direct spatial integration of the pressure gradient or using a Poisson formulation. In the latter approach the in-plane divergence of the pressure gradient (equation 4.2) is taken and subsequently integrated by a Poisson solver. The in-plane divergence of a vector function, $\mathbf{g}$, is $\nabla_{xy} \cdot \mathbf{g} = \partial g_x / \partial x + \partial g_y / \partial y$, where g_x and g_y are the components in *x*-direction and *y*-direction respectively.

$$\nabla_{xy} \cdot \nabla p = \frac{\partial^2 p}{\partial x^2} + \frac{\partial^2 p}{\partial y^2} = -\rho f_{xy} \qquad (4.2)$$

where f_{xy} is a function of the velocity field obtained by taking the in-plane divergence of equation 4.1 and dividing by $-\rho$, resulting in

$$f_{xy} = f_{2D} + f_{3D} = \left\{ \left(\frac{\partial u}{\partial x} \right)^2 + 2 \frac{\partial v}{\partial x} \frac{\partial u}{\partial y} + \left(\frac{\partial v}{\partial y} \right)^2 \right\} + \qquad (4.3)$$

$$\left\{ \frac{\partial \left(\nabla_{xy} \cdot \mathbf{u} \right)}{\partial t} + \left(\mathbf{u} \cdot \nabla \right) \left(\nabla_{xy} \cdot \mathbf{u} \right) + \frac{\partial w}{\partial x} \frac{\partial u}{\partial z} + \frac{\partial w}{\partial y} \frac{\partial v}{\partial z} \right\}$$

where f_{2D} indicates the part caused by the in-plane part of the flow and f_{3D} indicates the additional terms for 3D flow.

Now, even for 3D flow, most of the extra terms that appear can be extracted from planar-PIV-data, see equation 4.3. The additional 3D flow contributions contain the in-plane divergence of the velocity, which can be derived from planar PIV-data. 3D velocity information is needed for the parts containing an out-of-plane gradient.

4.2 Numerical implementation

For the numerical implementation we choose to split the problem in two. First we determine the pressure gradient field and subsequently we determine the pressure field by integrating the pressure gradient field. This makes it easier to pinpoint where the errors in the pressure determination arise. In the following discussion Δt refers to the vector field time separation $(1/f_{acq})$ as distinct from the laser pulse time separation for which we will use δt.

4.2.1 Pressure gradient determination

As reflected by the two alternative formulations for the momentum equation (see equation 4.1), the pressure gradient can be computed in two different ways: a Lagrangian form where all quantities are evaluated with respect to an element moving with the flow and in a Eulerian form where everything is taken relative to a fixed spatial location. For the Eulerian approach we use second-order central finite differences in space and time, as expressed by

$$\frac{\partial u}{\partial x}(x,y,z,t) = \frac{u(x+h,y,z,t)-u(x-h,y,z,t)}{2h} + O(h^2) \tag{4.4}$$

$$\frac{\partial u}{\partial t}(x,y,z,t) = \frac{u(x,y,z,t+\Delta t)-u(x,y,z,t-\Delta t)}{2\Delta t} + O(\Delta t^2), \tag{4.5}$$

respectively. u is the velocity component in x-direction, h is the grid spacing, and Δt is the time separation between consecutive velocity fields. The description of space and time is therefore not linked in computation or formulation (see equation 4.1).

For the Lagrangian approach we need to reconstruct the fluid-parcel trajectory. In the present study the fluid trajectory is reconstructed using a pseudo-tracking approach, which is derived from velocity fields rather than particle locations (see Liu & Katz 2006). A second-order fluid path is reconstructed using an iterative approach (indicated by the superscript k) given by

$$\mathbf{x}_p^k(t,\tau) = \mathbf{x}+\mathbf{u}(\mathbf{x},t)\,\tau+\tfrac{1}{2}\frac{D\mathbf{u}}{Dt}^k(\mathbf{x},t)\,\tau^2 \tag{4.6}$$

$$\frac{D\mathbf{u}}{Dt}^{k+1}(\mathbf{x},t) = \frac{\mathbf{u}\big(\mathbf{x}_p^k(t,\Delta t),t+\Delta t\big)-\mathbf{u}\big(\mathbf{x}_p^k(t,-\Delta t),t-\Delta t\big)}{2\Delta t} \tag{4.7}$$

where $\mathbf{x}_p$ is the fluid-parcel location. equation 4.6 is the second order expansion of the particle location with time interval τ relative to time instance t.

Although for the Lagrangian form the description of space and time seems not to be linked, based on the formulation in equation 4.1, it is clearly linked in the computation (equation 4.6).

The pressure gradient field is then determined using equation 4.1. Both approaches use linear forward or backward schemes at domain edges.

4.2.2   Pressure integration

Pressure integration is done by a Poisson solver that solves the in-plane Poisson formulation (equation 4.2) directly using a standard 5-point scheme (second order central finite differences),

$$\frac{p_{i+1,j} + p_{i-1,j} + p_{i,j+1} + p_{i,j-1} - 4p_{i,j}}{h^2} = -\rho f_{i,j}, \qquad (4.8)$$

where h is the grid spacing (uniform, $\Delta x = \Delta y = h$). The forcing term is determined with

$$f = f_{xy} = -\frac{1}{\rho} \left(\frac{\partial}{\partial x} \left(\frac{\partial p}{\partial x} \bigg|_{\text{PIV}} \right) + \frac{\partial}{\partial y} \left(\frac{\partial p}{\partial y} \bigg|_{\text{PIV}} \right) \right). \qquad (4.9)$$

To verify the proper working of this approach, we compared it to two alternative approaches for the integration of the pressure gradient: the omnidirectional integration approach used by Liu & Katz (2006) and a least-squares approach. A third approach, a direct spatial integration approach, was tested (see de Kat et al. 2008), but was excluded from this comparison because of its unfavorable directional dependence (see van Oudheusden 2008).

The differences in peak and noise response of the methods were found to be well below 1%, when tested on a stationary Gaussian vortex (see chapter 5) on a grid of 60×90 points. Furthermore, Charonko et al. (2010) found that, when sufficiently sampled, different integration techniques all give adequate results, even for different inputs (e.g. neglecting parts in equation 4.3). Based on these findings, the Poisson approach was selected for the following analyses.
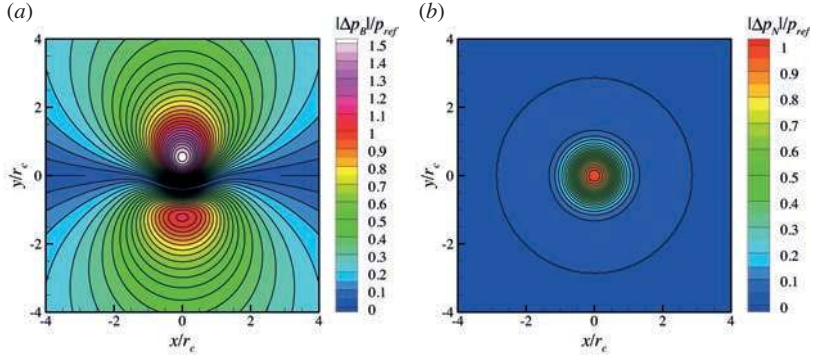
Figure 4.1: Boundary condition performance for a advecting Gaussian vortex. $U_a = 1\ WS/\Delta t$, $V_\theta = 0.5\ WS/\Delta t$, $r_c = 8\ WS$, OF = 75%, $\alpha = 0°$, $\beta = 0°$. (*a*) Difference between the Bernoulli pressure (equation 4.10) and the analytic pressure, Δp_B. (*b*) Difference between pressure from equation 4.13 and the analytic pressure, Δp_N. See chapter 5 for details on the Gaussian vortex

4.2.3 Boundary conditions

Boundary conditions are enforced on all edges of the pressure evaluation domain and consist of a reference boundary condition in a point or domain (pressure is prescribed) and Neumann conditions (pressure gradient is prescribed) on the remaining edges. The Neumann boundary conditions make use of equation 4.1 and are implemented using ghost-points. The reference boundary condition ideally would be placed in the inviscid outer-flow, where the Bernoulli equation can be used (i.e. incompressible, steady, irrotational and inviscid part of the flow),

$$p + \frac{1}{2}\rho\left(\mathbf{u}\cdot\mathbf{u}\right) = p_\infty + \frac{1}{2}\rho V_\infty^2. \tag{4.10}$$

However, due to the limited measurement domain of PIV, the boundary conditions need to be enforced within the disturbed flow domain. Starting from the line integral of the momentum equations (equation 1.1) and assuming irrotational and inviscid flow without body forces gives

$$\int_A^B \left\{ \rho\frac{\partial\mathbf{u}}{\partial t} + \nabla\left(\rho\frac{\mathbf{u}\cdot\mathbf{u}}{2} + p\right)\right\}\mathrm{d}s = 0. \tag{4.11}$$

Now using the Reynolds decomposition together with the assumptions of purely advective perturbations ($\mathrm{D}\mathbf{u}'/\mathrm{D}t = 0$) and a small mean velocity gradient, the acceleration can be rewritten as

$$\frac{\partial \mathbf{u}}{\partial t} = \frac{\partial \mathbf{u}'}{\partial t} \approx -\left(\overline{\mathbf{u}} \cdot \nabla\right)\mathbf{u}' \approx -\nabla\left(\mathbf{u}' \cdot \overline{\mathbf{u}}\right). \qquad (4.12)$$

The reference pressure can then be computed with

$$p + \frac{1}{2}\rho\left(\overline{\mathbf{u}} \cdot \overline{\mathbf{u}} + \mathbf{u}' \cdot \mathbf{u}'\right) = p_\infty + \frac{1}{2}\rho V_\infty^2. \qquad (4.13)$$

This expression can be seen as an extended version of the Bernoulli equation that it is corrected for the unsteady advective perturbations. The improvement of this formulation over the standard Bernoulli is shown in figure 4.1, where they are compared on an advecting Gaussian vortex (see chapter 5). Figure 4.1(*a*) clearly shows that the Bernoulli pressure (equation 4.10) does not work and shows large differences with the analytic pressure over the complete domain. These differences are mainly due to the fact that the velocity field is not steady and correspond to the inclusion of the $\mathbf{u}' \cdot \overline{\mathbf{u}}$ term. With the acvective velocity in *x*-direction the error should resemble the *u*-component of velocity, which is readily apparent when comparing figure 4.1(*a*) with figure 5.3(*a*). Figure 4.1(*b*) shows that the pressure from equation 4.13 only gives a difference in the rotational core of the vortex (cf. figure 5.3(*c*)), which is expected given the assumption of irrotational flow. Approximately one vortex radius from the center the error has dropped below $5\% p_{ref}$ and when the distance is larger than three vortex radii from the center the error has become negligible ($\Delta p_N < 0.01\% p_{ref}$).

4.3   Frequency response

A key feature of an experimental technique used to measure turbulent flow is its frequency response. The frequency response of the measurement procedure and subsequent data-analysis are affected in both space and time by truncation and precision errors. The influence of the truncation error is estimated using (simple) theoretical considerations. The influence of the precision error is estimated using linear error propagation.

Although we set out to start from a velocity field with its corresponding uncertainty, we need to know how PIV filters the velocity field and the noise on it, in order to know what the starting point of the pressure derivation is. PIV acts similarly to a moving average (see e.g. Schrijer & Scarano 2008, who also show improvements can be achieved with iterative schemes), resulting in a response (figure 4.2) to a 2D signal as given by

$$T_{\mathrm{PIV,2D}} = \mathrm{sinc}^2\left(\frac{WS}{\lambda_{\mathbf{x}}}\right) \tag{4.14}$$

where $T_{\mathrm{PIV,2D}}$ denotes the transfer function of PIV to a 2D signal, $\mathrm{sinc}\,(x) = \sin(\pi x)/\pi x$, WS is the interrogation window size, and λ_x is the spatial wavelength of the input signal (flow structure). Foucaut et al. (2004) show that noise is also affected by this low-pass filter behaviour.

PIV also has a limited temporal response, which is related to the laser pulse time separation, δt, and restricts the frequencies of flow phenomena that can be captured in individual velocity fields. This, however, is generally less restrictive than the limitation by the acquisition frequency ($\Delta t \geq \delta t$) and we will therefore focus on the influence of the acquisition frequency.

The current implementation of the determination of the pressure gradient field involves taking central finite differences. These central finite differences act as a low-pass filter due to the truncation error (see e.g. Foucaut & Stanislas 2002), with a response given in equation 4.15 (figure 4.2).

$$T_{\mathrm{CD}} = \mathrm{sinc}\left(\frac{2h}{\lambda_x}\right) \tag{4.15}$$

where T_{CD} denotes the transfer function of the central finite differences, h is the grid-spacing. When applied in time the filter response is the same, i.e. replace h with Δt and λ_x with λ_t.

A numerical test and theoretical analysis indicates also that the Poisson solver acts as a low-pass filter with a amplitude response as given in equation 4.16 (figure 4.2).

$$T_{\mathrm{PS}} = \frac{1 + \cos\left(\pi\frac{2h}{\lambda_{\mathbf{x}}}\right)}{2 \cdot \mathrm{sinc}\left(\frac{2h}{\lambda_{\mathbf{x}}}\right)} \tag{4.16}$$
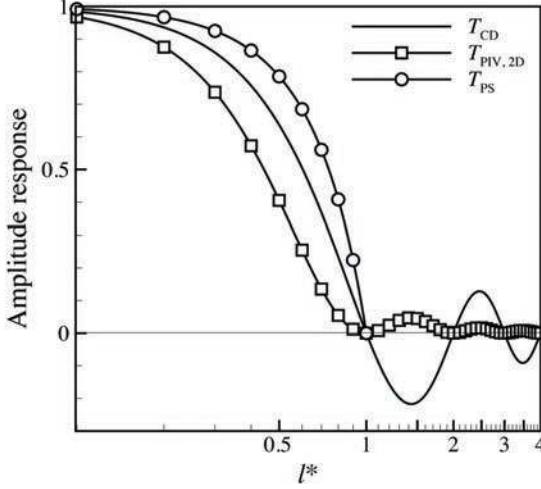
Figure 4.2: Amplitude response of PIV, central finite differences (CD) and the Poisson solver (PS). PIV: $l^* = WS/\lambda_x$; CD and PS: $l^* = 2h/\lambda_x$. PS is shown till $l^* = 1$, which is the Nyquist limit of PS and CD.

where T_{PS} denotes the transfer function of the Poisson solver.

For the pressure derived using the Eulerian form of the pressure gradient this means the filter due to the central finite differences acts in space and time separately and the filter of the Poisson solver in space. When using the Lagrangian form of the pressure gradient, the low-pass filter due to the central finite differences only acts in time and the filter of the Poisson solver in space. However, for the Lagrangian approach, the reconstruction of the trajectory of the fluid parcel path also has an additional effect on the spatial frequency response (see equation 4.6).

Violato et al. (2011) state the temporal limitation of a Eulerian approach to be related to the acceleration being measured on the same structure, leading to the expression given by

$$\Delta t_{\mathrm{Eul}} < \frac{1}{4}\frac{\lambda_x}{U_a} \qquad (4.17)$$

where Δt_{Eul} is the time separation between consecutive velocity fields

for the Eulerian approach, λ_x is the spatial wavelength, and U_a is the advective velocity.

However, this is only a part of the terms needed for the pressure gradient (see equation 4.1) and therefore does not state how strong the impact of this improper sampling will be. Following similar reasoning, i.e. a vortex should not exceed half a turn during the evaluation of the material acceleration, an equivalent expression can be derived for the temporal limitation of the Lagrangian approach,

$$\Delta t_{\text{Lag}} < \frac{1}{4}\frac{2\pi r}{V_\theta} \qquad (4.18)$$

where Δt_{Lag} is the time separation between consecutive velocity fields for the Lagrangian approach, r is the radius, and V_θ is the tangential velocity.

Here the expression is linked directly to the pressure gradient and its effect is expected to influence the complete domain. Also the domain should be large enough for the fluid path to be reconstructed. However, it is not possible to accurately capture these effects in simple theoretical considerations and therefore they will be assessed on a synthetic flow field in §5.

To have an estimate for the sensitivity to noise (precision error) of both approaches we follow a linear error propagation procedure as laid down by Kline & McClintock (1953) (see e.g. Stern et al. 1999, for a more thorough exposition). The error is assumed to be uncorrelated and to have a normal distribution. The error on a single sample can be estimated by the RMS value of the noise of the measurement tool and the error on a derived quantity can then be estimated as the root of the sum of the square of the uncertainties of the samples where it was derived from multiplied by their respective sensitivity. The noise propagation from the velocity field to the pressure field for the Eulerian form gives

$$\varepsilon_{p_{\text{Eul}}} \propto \varepsilon_u \sqrt{\frac{h^2}{2\Delta t^2} + |\nabla u|^2 h^2 + \frac{|\mathbf{u}|^2}{2}} \qquad (4.19)$$

where $\varepsilon_{p_{\text{Eul}}}$ is the (estimated RMS) error for the pressure based on the Eulerian approach, ε_u is the noise on the velocity, h is the grid spacing, Δt is the velocity field time separation, $|\nabla u|$ is the magnitude of the

gradient of the streamwise component of the velocity, and $|\mathbf{u}|$ is the velocity magnitude.

For the estimation of the noise sensitivity of the Lagrangian method, the fluid path reconstruction is simplified and taken to be linear (i.e. equation 4.6 and equation 4.7 are only used once). The result of the noise propagation then is

$$\varepsilon_{p_{\text{Lag}}} \propto \varepsilon_u \sqrt{\frac{h^2}{2\Delta t^2} + \frac{|\nabla u|^2 h^2}{2}} \qquad (4.20)$$

where $\varepsilon_{p_{\text{Lag}}}$ is the error for the pressure based on the Lagrangian approach.

These results indicate that when the (advective) velocity of the flow is small (with respect to the other terms in equation 4.19 and equation 4.20) both methods will react similarly to noise, whereas when the (advective) velocity is large the Eulerian approach will suffer, while the Lagrangian approach remains insensitive.

Due to the nonlinearity (with respect to the velocity field) of the pressure gradient determination, the exact behaviour of both methods is not available. Also the noise propagation procedure is limited to uncorrelated noise, whereas Foucaut et al. (2004) show that the (spatial) scales in the noise are effected by the PIV processing, especially apparent when using higher overlap-factors (OF). Furthermore the filtering effect of PIV is known to be different for 1D and 2D signals (see e.g. Schrijer & Scarano 2008).

Nevertheless, the considerations presented in this section provide a good indication of the parameters that will influence the performance of the pressure determination from PIV and what effect they may have. In summary, the Eulerian approach is expected to be more sensitive to noise and advective motion, whereas the Lagrangian should have difficulties capturing rotational flow, because this complicates the flow path reconstruction.

To substantiate and quantify these theoretical considerations on the performance of pressure determination, different methods are applied to a synthetic flow field, where the input velocity field has a known pressure distribution.

Chapter 5

Performance assessment

Vortices are arguably the most relevant flow structures occurring in practise, likely to be encountered in many fluid dynamic studies where pressure is of interest (e.g. separated flow, bluff body flows). The advection of a Gaussian vortex is taken to serve as an theoretical test-case for the pressure evaluation procedures. The analytic expression for the velocity field is used to generate synthetic PIV velocity fields and the theoretical pressure field is used as a reference to validate the pressure field computed from the synthetic PIV velocity fields. In the simulated experiments the influence of resolution in space and time is considered, as well as noise and spatial filtering caused by PIV, and the effects of 3D (out-of-plane) flow.

5.1   Synthetic flow field

The synthetic flow field consists of a linear combination of a Gaussian vortex and a uniform velocity field in x-direction, U_a (corresponding to the advection velocity of the vortex). The flow field relative to the vortex centre is described by the tangential velocity, V_θ, in a cylindrical polar coordinate system aligned with the vortex axis and moving with the vortex. The radius where V_θ reaches its maximum, V_p, is defined as the core radius, r_c (see figure 5.1). The velocity distribution and corresponding pressure distribution (relative to $p_\infty = 0$) are given in
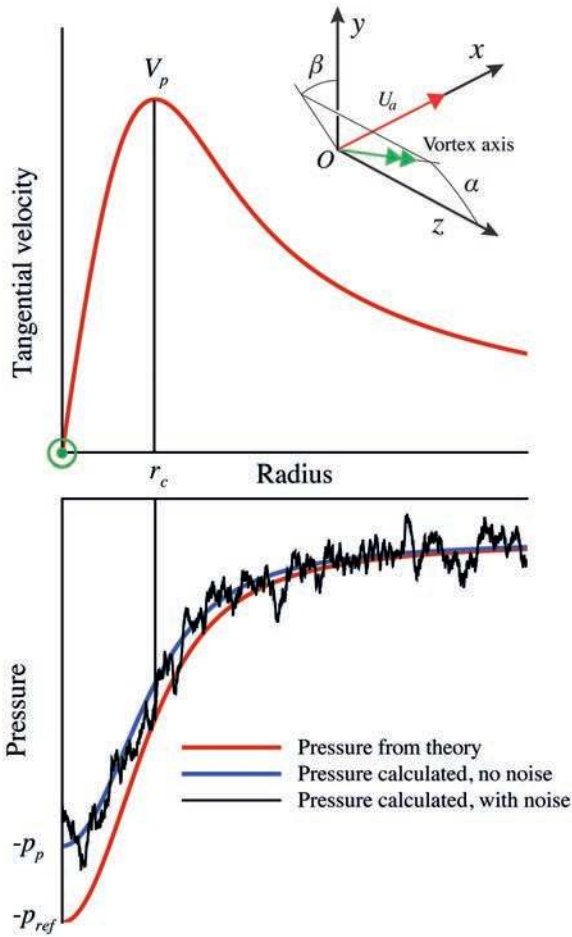
Figure 5.1: Synthetic tangential velocity distribution and corresponding pressure distributions.

equation 5.1 and 5.2,

$$V_\theta = \frac{\Gamma}{2\pi r} \left(1 - e^{-\frac{r^2}{c_\theta}} \right) \tag{5.1}$$

where Γ is the circulation, $c_\theta = r_c^2/\gamma$, and $\gamma = 1.256431$ is a constant to have V_p at r_c. The corresponding pressure distributions is

$$p = -\frac{1}{2}\rho V_\theta^2 + \int_r^\infty V_\theta(s)\, \omega_z(s)\, \mathrm{d}s \tag{5.2}$$

where ρ is the density. The first term on the right hand side is the irrotational contribution to the pressure where the second term is the contribution of the rotational part. The second term can be evaluated as

$$\int_r^\infty V_\theta(s)\, \omega_z(s)\, \mathrm{d}s = -\frac{\rho\Gamma^2}{4\pi^2 c_\theta} \left(E_1\left(\frac{r^2}{c_\theta}\right) - E_1\left(\frac{2r^2}{c_\theta}\right) \right), \tag{5.3}$$

where E_1 is the exponential integral defined as

$$E_1(x) = \int_x^\infty \frac{e^{-t}}{t}\, \mathrm{d}t, \tag{5.4}$$

and the minimum pressure is $\lim_{r\to 0} p = -\rho\Gamma^2 \ln 2/\left(4\pi^2 c_\theta\right) = -p_{ref}$.

3D flow is simulated by tilting the vortex-axis at an angle with the *x-y*-plane, α, where the orientation of this angle with respect to the *y*-direction is set by a second angle, β (see figure 5.1).

5.2 Numerical implementation

Velocity volumes were created by mapping equation 5.1 onto a cartesian grid (with the vortex axis placed at the centre of the domain) and adding the U_a, resulting in a grid with values for the u, v, and w components of velocity and corresponding pressure. The same procedure is followed to create velocity volumes for Δt and $-\Delta t$, where the vortex axis is moved the corresponding distance along the advection direction (i.e. $U_a \Delta t$ and $-U_a \Delta t$).

Nine random noise volumes were created and used in three sets of three (each time one for $-\Delta t$, 0 and Δt). In this way we assured that the

effects of varying parameters is not influenced by the use of different noise volumes (from case to case) and, by using three sets, we reduce the influence of having a specific response to a single noise volume set.

To account for the filtering effect PIV has on the velocity field and the noise in the velocity field (see Foucaut et al. 2004), the velocity volume and separate random noise volumes were filtered using a moving-average filter over the interrogation window-size (*WS*) simulating an overlap-factor (OF) of 75%. After filtering the volumes were cropped to avoid end-effects of the filtering procedure. The final volumes were $257 \times 257 \times 33$ points, representing a volume of $65 \times 65 \times 9$ independent *WS*. The thickness of these volumes was sufficient to reconstruct 3D paths for the 3D flow assessment. For the lower OF values a subset of this velocity volume was taken. For each case, the noise level was scaled to give the desired root-mean-square (RMS) values, ε_u, as a percentage of the maximum (theoretical) velocity occurring in the flow field, in line with PIV-practise.

In the current analysis, influences on PIV accuracy due to acceleration and flow-field curvature were not taken into account in the modelling. Hain & Kähler (2007) show that these can have significant effects on the accuracy of PIV. Despite this omission, the current analysis should allow to find the range in which pressure determination from PIV is possible. Only when the effects of acceleration and flow-field curvature are large, like in strong vortices, the actual pressure results derived from PIV are likely to be worse than this analysis will indicate.

From the velocity fields, the pressure gradient fields were determined using either the Eulerian or Lagrangian approach and subsequently integrated using the Poisson approach, with Dirichlet conditions on the lower side of the domain and Neumann conditions on the remaining edges, see figure 5.2.

The resulting pressure fields were assessed in two different ways. First, the peak response was determined by taking the ratio of the peak calculated pressure, p_p, and the peak of the theoretical pressure, p_{ref} (see figure 5.1). Second, the noise response, ε_p, was determined by taking the (spatial) RMS of the difference between the pressure calculated from the velocity field with noise and the pressure calculated from the velocity field without noise (if the theoretical pressure is used, the peak response will influence the RMS, which is unwanted). Each value of
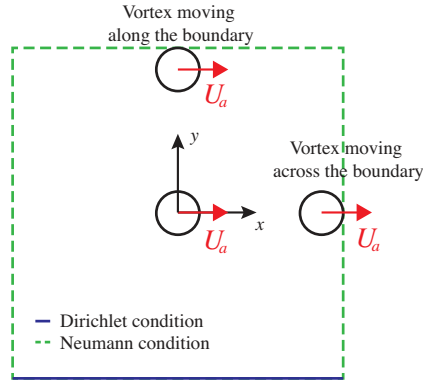
Figure 5.2: Schematic of the computational domain. Indicated are the primary vortex location, the vortex moving along the boundary of the domain, and the vortex moving across the boundary of the domain.

the noise response presented is an average of the results of the three sets of noise used.

To investigate the effects of the vortex moving along or across the boundary of the domain (see figure 5.2 for a schematic representation), the vortex centre was placed at different distances from the boundary (ranging from the centre to the boundary of the domain). The influence is determined by taking the difference between the pressure determination for a stationary vortex and an advecting vortex for each location. The maximum perturbation of all distances is then taken to represent the influence of that advection velocity.

5.3 Results

Figure 5.3 shows an example of the input for and the result from the calculations. Contours of velocity are shown in 5.3(*a*) and 5.3(*b*). The effect of addition of noise is clearly present when comparing the contours to the overlaid black lines that correspond to the analytic velocity field. The corresponding vorticity field in figure 5.3(*c*) also demonstrates this clearly. The outer overlaid black line indicates that the analytic vortic-
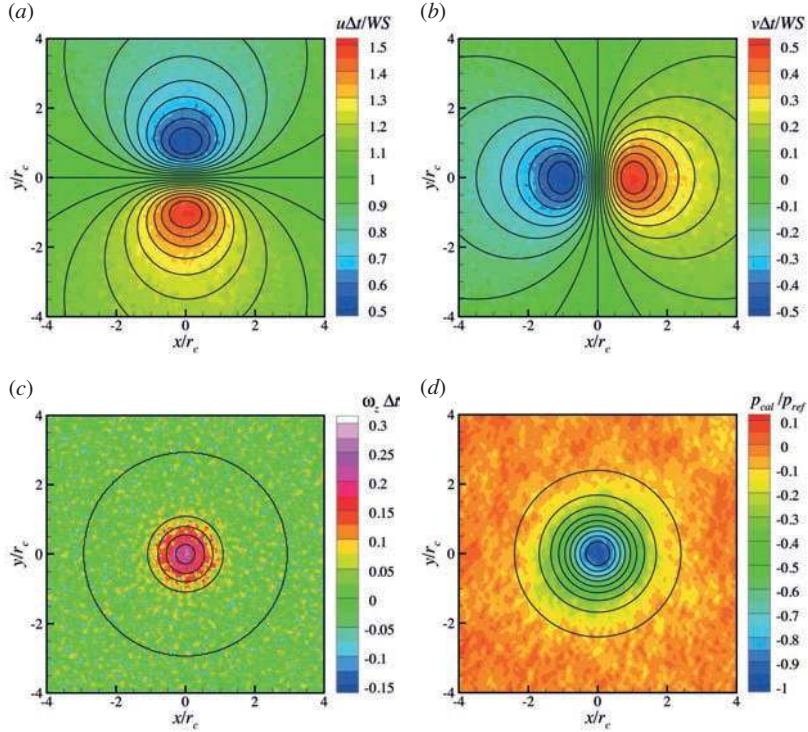
Figure 5.3: Example of the velocity field, vorticity field, and pressure field. Overlaid are black lines of the corresponding analytic field. $U_a = 1$ $WS/\Delta t$, $V_\theta = 0.5$ $WS/\Delta t$, $r_c = 8$ WS, OF = 75%, $\alpha = 0°$, $\beta = 0°$, $\varepsilon_u = 1\%U_{max}$. (a) u-component of velocity. Overlay from 0.55 to 1.45 in steps of 0.05. (b) v-component of velocity. Overlay from -0.45 to 0.45 in steps of 0.05. (c) Out-of-plane vorticity, ω_z. Overlay from 0 to 0.2 in steps of 0.05. (d) Pressure field from Eulerian pressure gradient. Overlay from -0.9 to -0.1 in steps of 0.1.

ity is negligible ($\omega_z \Delta t < 0.01\%$) for radii larger than three vortex core radii. Figure 5.3(d) shows the resulting pressure field obtained by integrating the Eulerian pressure gradient. The noise clearly has an effect on the pressure field, but the signature of the pressure of the vortex is still present.

Figure 5.4-5.6 show the peak and noise responses for different spatial and temporal resolutions. The temporal resolution is split into two contributions, one related to the advection of the vortex and one related to the strength of the vortex. The variations were taken with respect to a noncritical base-line (see figure 5.3).

Figure 5.4 shows the variation of the peak response and noise response with the spatial resolution. The trend for the peak response in figure 5.4(a) is in good agreement with the trend in figure 4.2, showing an increase in modulation as the ratio WS/r_c increases. The Eulerian and Lagrangian approach perform nearly identical. Increasing the OF shows significant improvement for poor spatial resolutions (big WS). However, this improvement is limited, since increasing OF improves the description of the signal (sampling), but does not overcome the filtering effects of the moving-average behaviour of PIV. As the spatial resolution increases the improvement obtained with higher OF, becomes less pronounces. The results for 50% and 75% overlap are very similar over the complete range investigated and for WS/r_c smaller than 0.5 their modulation is smaller than 10% (peak response > 0.9). For $WS/r_c < 0.25$ all OF give a modulation of smaller than 5% (peak response > 0.95). This indicates that when sampling at a spatial frequency ten times higher than the spatial frequency in the flow ($WS/\lambda_x < 0.1$, $\lambda_x \approx 2r_c$) the modulation will be smaller than 5% and that when sampling at a spatial frequency five times higher ($WS/\lambda_x < 0.2$) the modulation for 50% and 75% OF is smaller than 10%. The noise response is hardly affected by changes in spatial resolution or OF, see figure 5.4(b). The Eulerian approach has a higher value of noise, $\varepsilon_p \approx 4.5\% p_{ref}$, than the Lagrangian approach, $\varepsilon_p \approx 3.5\% p_{ref}$.

The response to change in temporal resolution is divided in two influences, response to an advective velocity, U_a, and response to the pean tangential velocity, V_p, of the vortex. Figure 5.5 shows the influence of the advective velocity on the peak response and noise response. Changing the advective velocity has no influence for the Eulerian ap-
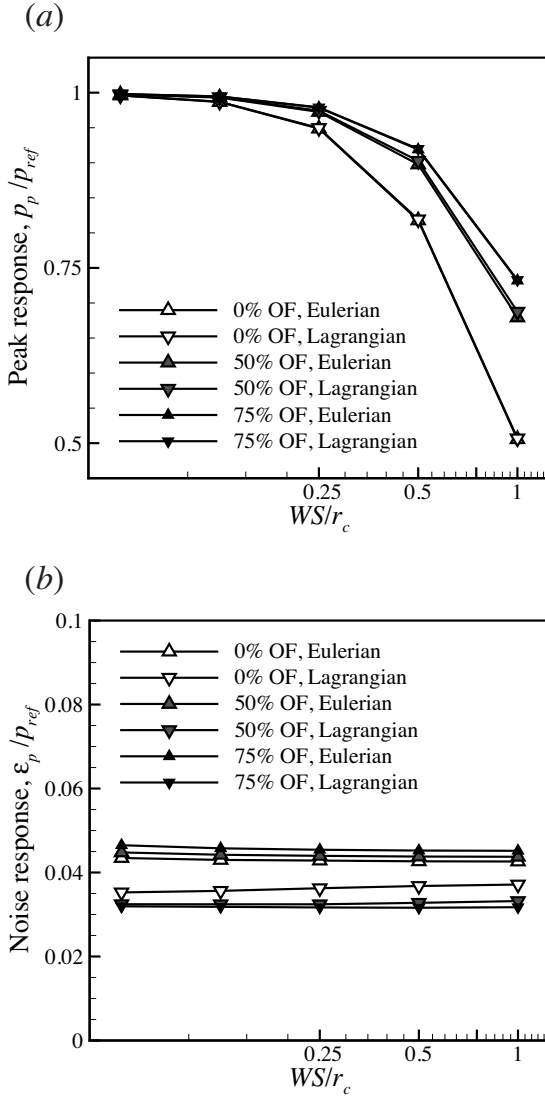
(*a*)

(*b*)

Figure 5.4: Influence of spatial resolution on peak and noise response. $U_a = 1\ WS/\Delta t$, $V_\theta = 0.5\ WS/\Delta t$, $\alpha = 0°$, $\beta = 0°$; for the noise response: $\varepsilon_u = 1\% U_{max}$. (*a*) Peak response. (*b*) Noise response.
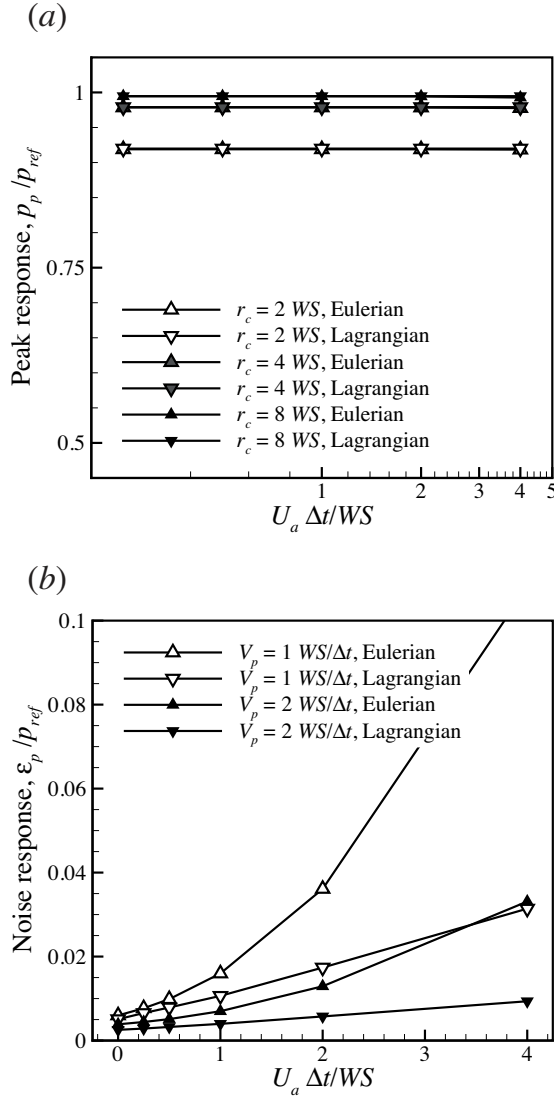
(*a*)

(*b*)

Figure 5.5: Influence of advective velocity on peak and noise response. Unless indicated otherwise: $V_\theta = 0.5\ WS/\Delta t$, $r_c = 8\ WS$, OF = 75%, $\alpha = 0°$, $\beta = 0°$; for the noise response: $\varepsilon_u = 1\% U_{max}$. (*a*) Peak response. (*b*) Noise response.
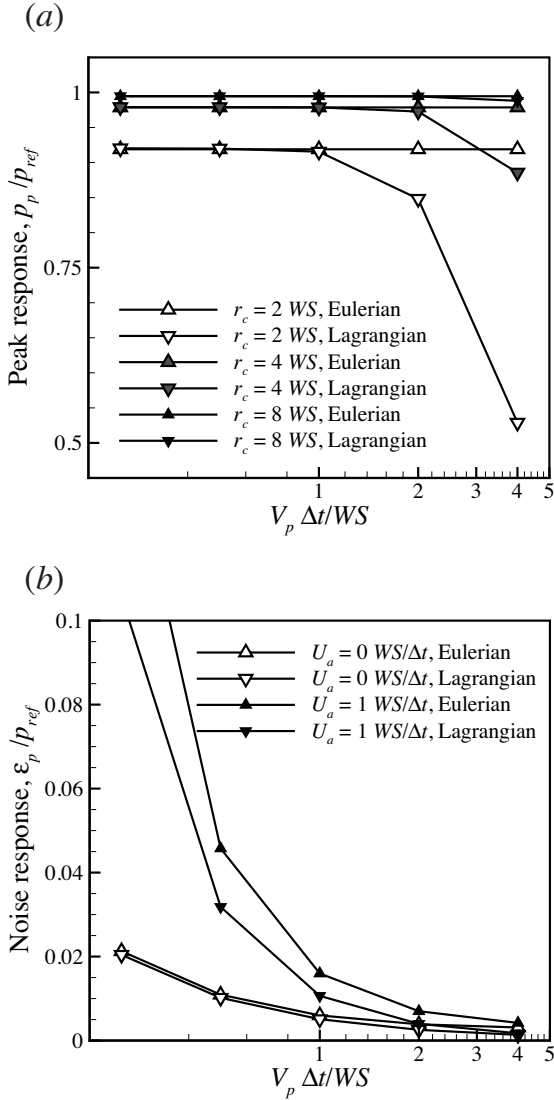
(a)

(b)

Figure 5.6: Influence of tangential velocity on peak and noise response. Unless indicated otherwise: $U_a = 1\,WS/\Delta t$, $r_c = 8\,WS$, OF = 75%, $\alpha = 0°$, $\beta = 0°$; for the noise response: $\varepsilon_u = 1\%U_{max}$. ($a$) Peak response. ($b$) Noise response.

proach and the Lagrangian approach, their response is identical, see figure 5.5(*a*). This response is expected for the Lagrangian approach and although this seems in contrast with equation 4.17 for the Eulerian approach, it can be explained. Since the flow is 2D and the acceleration is completely absent in the 2D part of equation 4.3, the only way that this improper time sampling can affect the results is via the acceleration at the boundaries of the domain. This influence will be covered later. Figure 5.5(*b*) shows the noise response to a change in advective velocity. The Eulerian approach is affected more by the noise than the Lagrangian approach. The Eulerian approach shows a trend with increasing advective velocity that agrees well with equation 4.19. It is approximately a quadratic increase, since $\varepsilon_u \propto U_a$ (ε_u is given in $\%U_{max}$, where $U_{max} = U_a + V_p$) and the square root term also is $\propto U_a$. The Lagrangian approach shows a linear increase with increasing advective velocity, which is in good agreement with equation 4.20, where only ε_u is proportional to U_a.

Figure 5.6 shows peak responses and noise responses for changes in tangential velocity, V_p. The peak response of the Eulerian approach is unaffected by a change in V_p, whereas the Lagrangian approach drops off at different values of V_p for different r_c (figure 5.6(*a*)). Based on the equation 4.18 we expect a decrease of the Lagrangian approach for increasing V_θ/r. When plotted with a measure for the vortex turnover-time, $V_p\Delta t/2\pi r_c$ (figure 5.7(*a*)), a drop off for $V_p\Delta t/2\pi r_c > 0.1$ is clearly visible. For temporal resolutions higher than $V_p\Delta t/2\pi r_c \approx 0.1$ no significant effect is present. This means that for a temporal resolution ten times higher than the Lagrangian time scale (vortex turnover time, $V_p\Delta t/2\pi r_c < 0.1$) the Lagrangian approach will work properly. For poorer temporal resolutions severe modulation is expected. Figure 5.6(*b*) shows an unexpected decreasing trend for the noise responses of the Eulerian and Lagrangian approach with increasing tangential velocity. However, it can be shown that $p_{ref} \propto V_p^2$ and therefore $\varepsilon_p/p_{ref} \propto 1/V_p$, which explains the trend observed.

Figure 5.7(*b*) shows a linear behaviour of the noise on the pressure with increasing noise on the velocity field, which is in agreement with equation 4.19 and 4.20. For $U_a = 0\ WS/\Delta t$ the Eulerian and Lagrangian approach have similar noise responses, when there is an advective velocity the Eulerian approach performs worse, see figure 5.5(*b*).
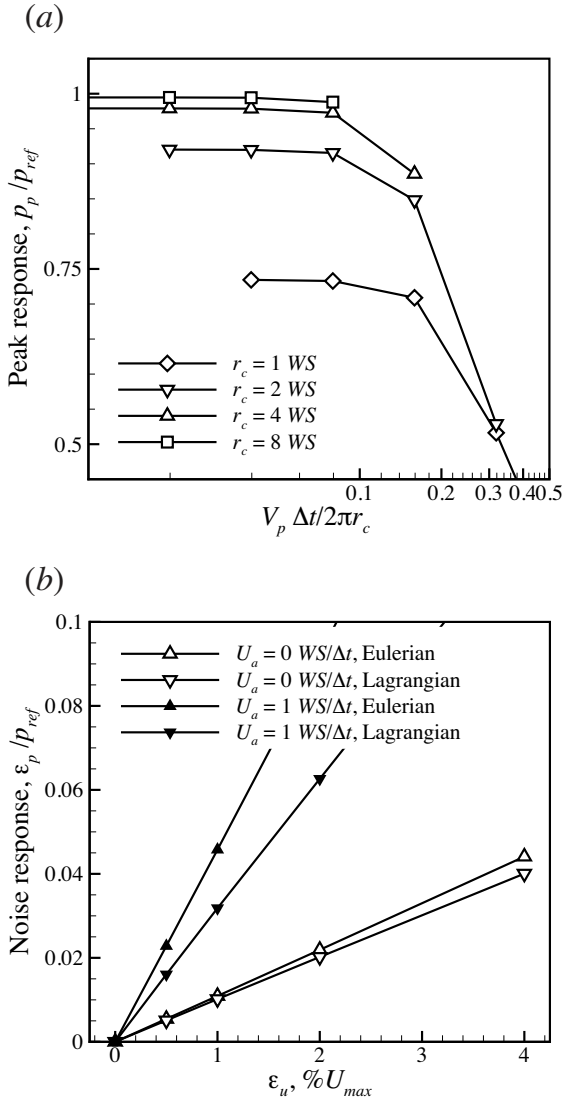
(a)

(b)

Figure 5.7: Influence of vortex turnover time and noise level. Unless indicated otherwise: $U_a = 1\ WS/\Delta t$, $V_\theta = 0.5\ WS/\Delta t$, $r_c = 8\ WS$, OF = 75%, $\alpha = 0°$, $\beta = 0°$; for the noise response: $\varepsilon_u = 1\%U_{max}$. (a) Peak response of the Lagrangian approach with vortex turnover time. (b) Noise response with noise level.
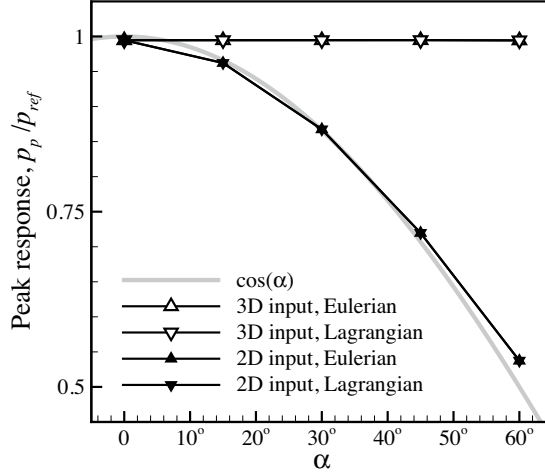
Figure 5.8: Influence of the inclination angle of the vortex on the peak response. $U_a = 1 \; WS/\Delta t$, $V_\theta = 0.5 \; WS/\Delta t$, $r_c = 8 \; WS$, OF = 75%, $\beta = 0°$.

Figure 5.8 shows the influence of the angle between the vortex axis and the plane-normal, α, for 2D input and 3D input. The 2D input is a subset of the 3D input without the out-of-plane components, which simulates planar and stereo-PIV. The reader should note that although stereo-PIV does give the out-of-plane velocity component, the out-of-plane velocity gradient is needed to make use of the out-of-plane velocity component (see equation 4.3), hence making it equivalent to planar-PIV for pressure determination. It is clear that the peak response is very similar to $\cos(\alpha)$. No effect associated to β was found.

As indicated earlier the Eulerian approach is expected to suffer from the limitation given in equation 4.17 on the edges of the domain. The maximum influence was found to be located at the boundaries and the influence propagated reciprocally with the distance from the boundary into the domain. Figure 5.9 and figure 5.10 show the results from the assessment of the edge effects. Figure 5.9 shows the error introduced
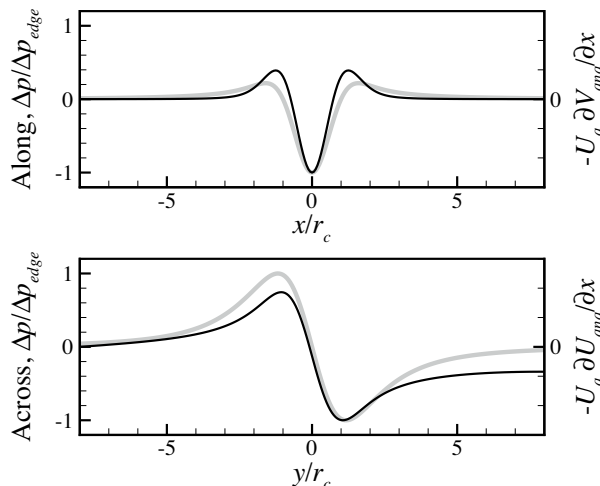
Figure 5.9: Edge effects. Pressure error for the Eulerian approach on the boundary of the domain shown in *black*. Analytic Eulerian acceleration shown in *grey*. *Top*: vortex moving along a boundary. *Bottom*: vortex moving across a boundary. Unless indicated otherwise: $U_a = 1$ WS/Δt, $V_\theta = 0.5$ WS/Δt, $r_c = 8$ WS, OF = 75%, $\alpha = 0°$, $\beta = 0°$.

along the edge together with the corresponding acceleration for a vortex moving along the boundary (top) and for a vortex moving across a boundary (bottom). The error is clearly related to the acceleration.

To quantify the influence of U_a and r_c the maximum deviation due to the edge effect is determined and plotted with $U_a \Delta t / r_c$. For the Eulerian approach the edge effect error shows a rapid increase of the error starting at $U_a \Delta t / r_c \approx 0.2$, which is in line with equation 4.17, for both the case where the vortex moves along the boundary (figure 5.10(a)) and the case where the vortex moves across the boundary (figure 5.10(b)). The Lagrangian approach reacts as expected with only a minor influence for the case where the vortex moves across the boundary (figure 5.10(b)), which can be attributed to the switch to the forward/backward scheme at the boundary.
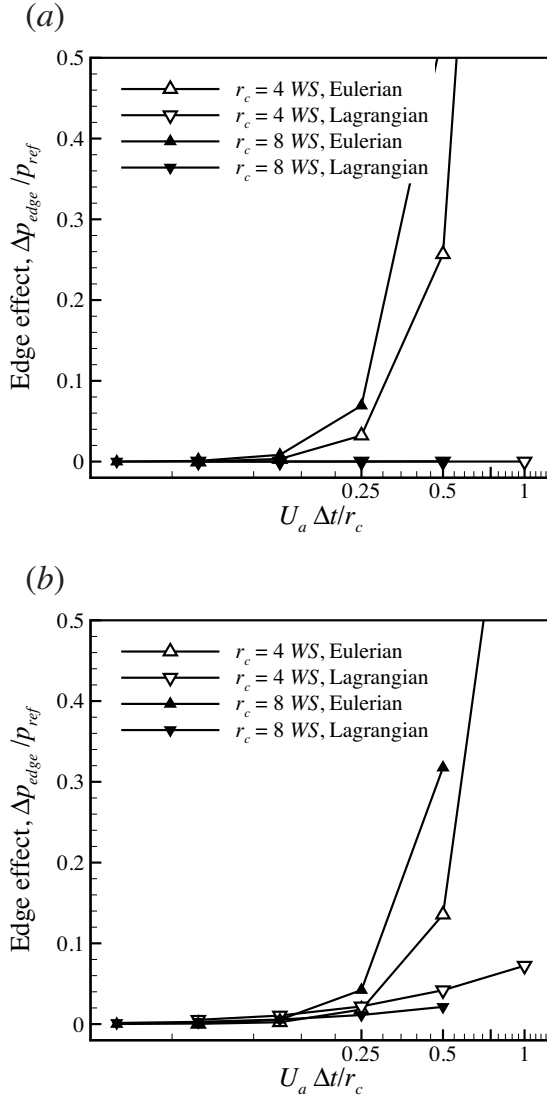
(*a*)

(*b*)

Figure 5.10: Influence of advective velocity on the edge effects. $V_\theta = 0.5\ WS/\Delta t$, OF = 75%, $\alpha = 0°$, $\beta = 0°$. (*a*) Absolute maxima of the error on the edge for a vortex moving along a boundary. (*b*) Absolute maxima of the error on the edge for a vortex moving across a boundary.

5.4   Summary

Although the present evaluation is not directly comparable to the results
of Charonko et al. (2010), since they did not split the influences of trun-
cation and precision effects, the trends of the peak and noise responses
combined show similar trends in their results.

Successful determination of pressure from PIV data needs to com-
ply with a number of criteria. For both approaches it applies that the *WS*
should be sufficiently small with respect to the flow structures. A larger
OF does increase the quality of the pressure determination, but the ef-
fect of OF is less pronounced when the *WS* is sufficiently small. For
spatial sampling frequencies larger than ten times the spatial frequency
(taking $\lambda_x \approx 2r_c$) in the flow ($WS/\lambda_x < 0.1$) the peak modulation is less
than 5%. For spatial sampling frequencies larger than five times the
spatial frequency in the flow ($WS/\lambda_x < 0.2$) the peak modulation is less
than 10% for OF or 50% and 75%.

Complete 3D velocity measurements are needed to properly capture
the pressure in 3D flow. Omitting out-of-plane components results in a
peak response error that behaves like $\cos(\alpha)$, where α is the angle of
the vortex axis with the measurement plane.

Reducing the measurement noise on the velocity fields directly im-
proves the pressure determination for both approaches.

The Eulerian approach suffers more from measurement noise than
the Lagrangian approach, especially when advection velocity is present,
and is furthermore limited by the advection of flow structures over
the boundary. The time separation between subsequent velocity fields
needs to be sufficiently small to correctly capture the acceleration on the
boundaries. Time separation should be $\Delta t < 0.2r_c/U_a$, which means
that the acquisition frequency needs to be ten times larger than the
largest frequency at a given point in the flow (i.e. the Eulerian time
scales), $f_{acq} > 10 \times f_{flow}$ ($\lambda_x \approx 2r_c$).

The Lagrangian approach is limited by the turn over time of the
structures in the flow. The time separation needs to be sufficiently
small to correctly capture the pressure correctly. The time separation
should be $\Delta t < 0.1 \times 2\pi r_c/V_p$, which means that the acquisition fre-
quency needs to be larger than ten times the turnover frequency in the
flow (i.e. the Lagrangian time scales), $f_{acq} > 10 \times f_{turnover}$.

Chapter 6

Experimental arrangement

6.1 Experimental setup and conditions

Experiments were performed in a low-speed, open-jet wind-tunnel at the Aerodynamics laboratory at Delft University of Technology. The tunnel outlet has dimensions 40 cm × 40 cm. A square-section cylinder with dimension 30 mm × 30 mm ($D \times D$) and 34.5 cm in span was fitted with endplates and positioned in the middle of the free-stream. The geometric blockage was 6.5%. The nominal free-stream velocity, U, was 4.7 m s^{-1} (nominal dynamic pressure, $q = 13.5$ Pa), giving Reynolds number $Re_D = UD/v = 9,500$. The main vortex shedding frequency was $f_s = 20$ Hz, corresponding to a Strouhal number of $St = f_s D/U = 0.13$, which is in good agreement with the results of Okajima (1982), who found $St = 0.13$ for $10^4 < Re_D < 2 \times 10^4$. The free-stream turbulence intensity was assessed by hot-wire-anemometry and was approximately 0.1%. These experimental conditions are summarised in table 6.1. Additional experiments were performed at $U = 3.0$ m s^{-1} and $U = 9.7$ m s^{-1}, resulting in $Re_D = 6,000$ and $Re_D = 19,000$, respectively. These additional experiments are used for describing square cylinder pressure. The conditions for the experiments used for this description are listed in table 6.2.

The cylinder was instrumented with two flush mounted pressure transducers (figure 6.2) located in close proximity to midspan of the model to provide reference values for the pressure signals extracted
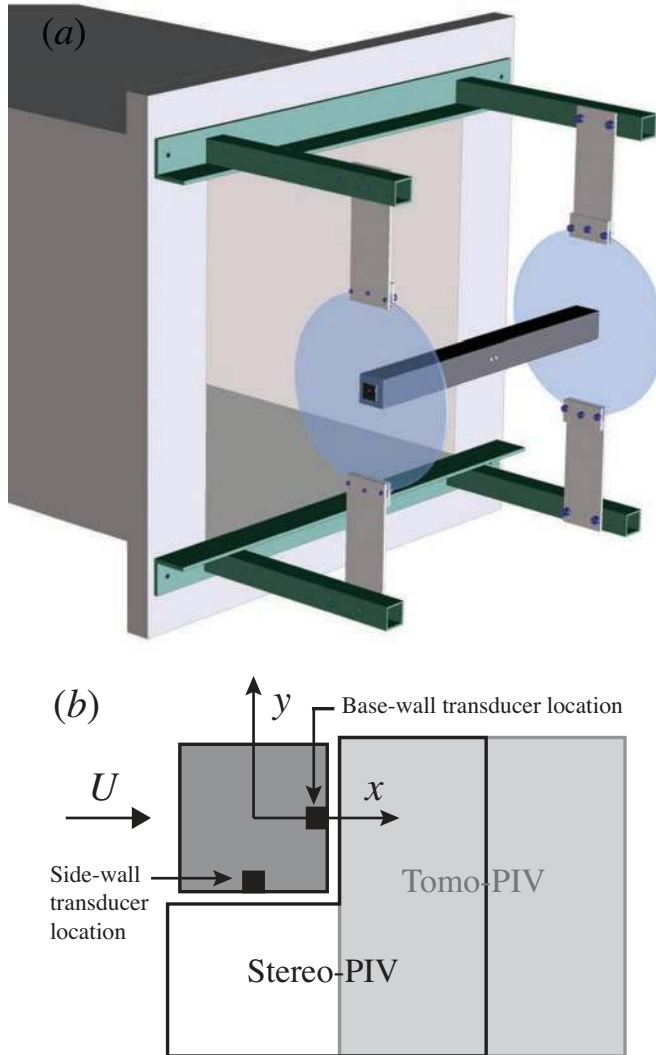
Figure 6.1: Schematic drawings of the tunnel exit with installed model and the fields-of-view, x- and y-directions and pressure transducer locations. (*a*) tunnel exit with installed model (courtesy of F.J. Donker Duyvis) (*b*) fields-of-view.

Table 6.1: Experimental conditions for experimental assessment

Variable	Value	uncertainty
Free-stream velocity, U	4.7 m s^{-1}	$\pm$ 2%
Free-stream turbulence intensity	0.1% U	–
Tunnel dimension	400 mm	–
Cylinder dimension, D	30 mm	–
Blockage	6.5%	–
Cylinder length	345 mm	–
Reynolds number, Re_D	9,500	$\pm$ 2%
Dynamic pressure, q	13.5 Pa	$\pm$ 2%
Vortex shedding frequency, f_s	20 Hz	$\pm$ 1%
Strouhal number, St	0.13	$\pm$ 2%

from the PIV data. For the stereo-PIV one transducer was located at the bottom and one at the base and for the tomo-PIV setup both transducers are located at the base on either side of the measurement-volume. For comparison separate pressure measurements were performed with both transducers located at the side-wall on either side of the measurement location. Figure 6.1 shows the transducer locations as well as the field-of-view used for the stereo-PIV and tomo-PIV setup.

The pressure transducers, Endevco 8507-C1, have a range of 1 psi

Table 6.2: Experimental conditions for square cylinder pressure

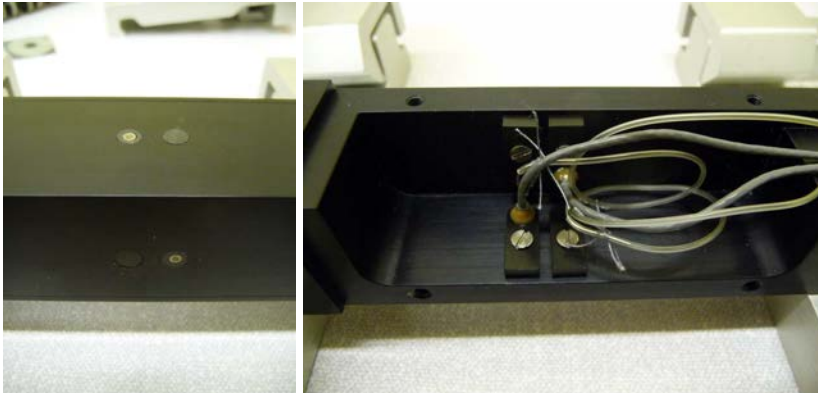| Parameter	Re_D			ε
	6,000	9,500	19,000	<3%
q, Pa	5.3	13.2	56.0	0.3
U, m s^{-1}	3.0	4.7	9.7	<3%
f_s, Hz	12.3	20.0	41.6	<1%
St	0.124	0.128	0.128	<3%

Figure 6.2: Pressure transducer assembly. *Left*: flush mounting of the pressure transducers. *Right*: internal layout of connections

(6,895 Pa), and a typical sensitivity of 175 mV psi^{-1} (25 μV Pa^{-1}), with a sensitivity-change related to temperature of less than 0.2% under current operating conditions. They were calibrated, using a closed system with a U-tube, against a Mensor DPG 2001 (range 0.5 psi; 3,447 Pa, uncertainty 0.010% full scale). Signal recording was performed using a National Instruments data acquisition system (consisting of: PCI-6250, SCXI-1001, SCXI-1520, and SCXI-1314) operating at 10 kHz (bandwidth (-3 dB): 20 kHz). The resulting noise-level was 4 μV$_{RMS}$ resulting in a resolution of 0.3 Pa (twice the RMS-level). The zero-drift for each run was less than 2 μV. Unless stated otherwise the pressure signals are unfiltered (and not corrected for the effects of wind-tunnel blockage). The pressure measurement on the side of model suffered from laser-influences. The laser-influence was removed by deleting erroneous points and filling the gaps by interpolation. The signal was subsequently low-pass filtered with a second order fit (robust Loess) over 25 points. The power-spectrum was checked against a pressure measurement without laser-interference and was confirmed to be unchanged for frequencies up to 400 Hz.

6.2 PIV-setup

A high-repetition-rate PIV-system in a stereo-PIV and tomo-PIV setup, see figure 6.3, was used to capture the flow. Flow seeding was provided by a Safex smoke generator, which delivered droplets of about 1 μm in diameter. The measurement plane was illuminated by a Quantronix Darwin-Duo laser system with an average output of 80 W at 3 kHz at a wavelength of 527 nm. The typical energy per pulse was 16 mJ at 2.7 kHz. The laser-pulse separation was 90 μs. Images were acquired by Photron Fastcam SA1 cameras (two for the stereo setup and four for the tomographic setup) with a 1,024 $\times$ 1,024 pixels sensor (pixel-pitch 20 μm), recording image-pairs at 2.7 kHz, equipped with Nikon lenses with focal length 60 mm and aperture set at 2.8 (top cameras in tomo-setup at 5.6). One camera was positioned normal to the image plane. The other cameras were mounted with adapters such that the Scheimpflug criterion was met. A total of 5,456 image-pairs, spanning just over two seconds, was captured for the stereo-PIV setup and a total of 2,728 image-pairs, spanning just over one second, was captured for the tomo-PIV setup. Synchronization between the cameras, laser, and image acquisition was accomplished by a LaVision programmable unit in combination with a high-speed controller, both controlled through DaVis 7.2 software. Particle image pairs were processed using DaVis 7.4 software. This software was also used for self-calibration, which corrects the misalignment of the calibration plate with the laser sheet (see Wieneke 2005, 2008). For the stereo-PIV setup the self-calibration process corrected the misalignment to within 0.01 pixels and for the tomo-PIV setup to within 0.07 pixels. Particle images were preprocessed by subtracting the time-minimum and applying a 3$\times$3 Gaussian filter. The vector fields were processed with a median test (see e.g. Westerweel & Scarano 2005) combined with a multiple correlation peak check. Remaining spurious vectors were removed and replaced using linear interpolation. The total number of spurious vectors was less than 2% for both data-sets.

An overview of the main PIV settings used in this investigation is given in table 6.3. For the stereo-PIV the field-of-view (FOV) was captured with a digital resolution of 15.7 pix mm^{-1}. The laser light sheet thickness was approximately 1 mm. The final interrogation window-
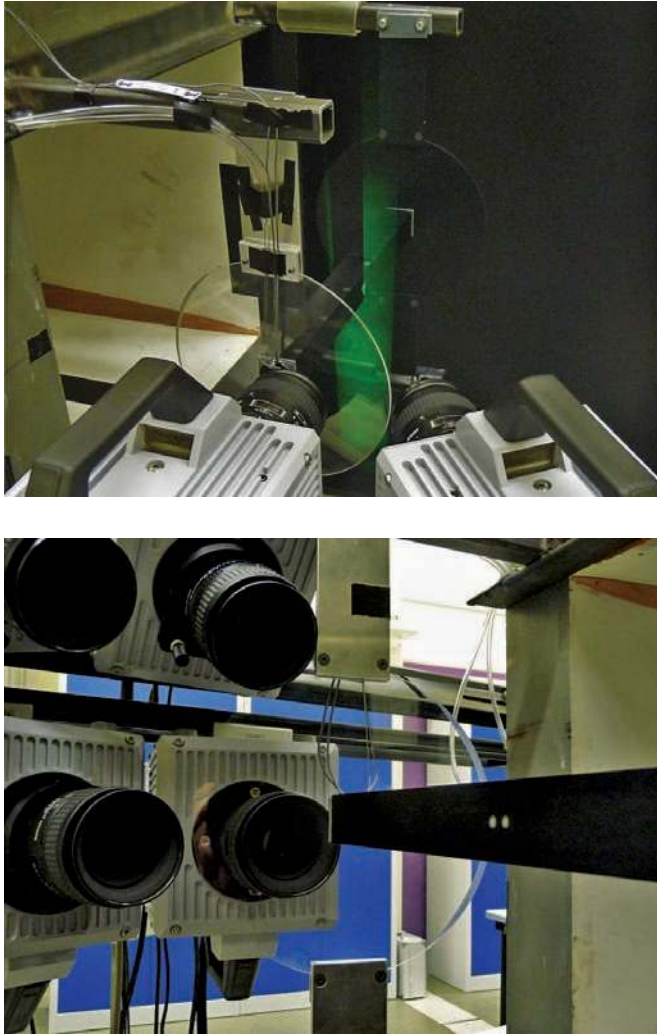
Figure 6.3: Photograph showing the experimental arrangements. *Top* Stereo-PIV setup. *Bottom* Tomo-PIV setup.

Table 6.3: Main PIV settings

	Stereo-PIV	Tomo-PIV
Number of cameras	2	4
Lenses	Nikon 60 mm	Nikon 60 mm
Aperture setting, $f_\#$	2.8	2.8 & 5.6
Angle between cameras	32°	30°×30°
Digital resolution, $1/\kappa$	15.7 pix mm^{-1}	14.3 pix mm^{-1}
Magnification error[a], $\varepsilon_\kappa/\kappa$	$< 0.1\%$	$< 0.1\%$
Acquisition frequency, f_{acq}	2.7 kHz	2.7 kHz
Laser sheet thickness	1 mm	4 mm
Laser pulse time sep., δt	90 μs	90 μs
Laser pulse t-sep. error[b], $\varepsilon_{\delta t}/\delta t$	0.2%	0.2%
Velocity field time sep., Δt	370 μs	370 μs
Initial interrogation area	32×32 pix	32×32×32 pix
Final interrogation area	16×16 pix	16×16×16 pix
Overlap factor	50%	50%
Vector field size	118×125	$99 \times 110 \times 7$
Dynamic velocity range[c]	130	110

[a] l_c=10 mm, $\varepsilon_{l_c} = 0$, ε_{n_c} based on calibration misalignment
[b] using the laser pulse width, $\varepsilon_{\delta t} = 0.2\,\mu$s
[c] ratio of maximum pixel displacement with ε_{cc} (see Adrian 1997)

size was varied between 16×16 pixels and 128×128 pixels and the OF between 0% and 75% resulting in vector grids of 236×250 vectors to 14×15 vectors (after cropping), for 16×16 pixels with 75% OF and 128×128 pixels with 50% OF, respectively. The additional experiments at $Re_D = 6,000$ and $Re_D = 19,000$, had $\delta t = 130\,\mu$s and $\delta t = 45\,\mu$s, respectively.

For the tomo-PIV the illuminated volume was 70 mm $\times$ 70 mm $\times$ 4 mm. It was captured with a digital resolution of 14.3 pix mm^{-1}. The final interrogation volume-size of $16 \times 16 \times 16$ voxels with an OF of 50% gave a vector grid of $99 \times 110 \times 7$ vectors (after cropping) with vector-spacing of 0.56 mm.

6.3   Pressure determination

For the assessment of the pressure determination a total of 2728 ve-
locity fields were used to determine the pressure, spanning just over a
second, for both the stereo-PIV and tomo-PIV configurations. The in-
plane pressure gradient was determined using either the Lagrangian or
the Eulerian formulation. The pressure field was obtained by the Pois-
son integration approach with a Dirichlet condition on the lower edge
of the domain and Neumann conditions on the remaining edges. For
the description of square cylinder pressure in chapter 8, pressure was
determined for stereo-PIV configuration using all 5,456 velocity fields.
Pressure (co-)spectra were determined by dividing one second of pres-
sure data in seven blocks with 50% overlap and averaging the spectra
obtained from these blocks.

6.4   Phase-averaging procedure

Although naturally occurring quasi-periodic flows make it more diffi-
cult to fix an unambiguous reference time variation (Lyn & Rodi 1994),
phase information was deduced from the pressure signal taken from the
side-wall transducer. The signal was low-pass filtered with a second
order fit (robust Loess) with a kernel of 100 points (see figure 6.4(a)),
giving it an estimated cut-off frequency of 100 Hz with frequencies
below 50 Hz unaffected. The discrete time analytic signal was recon-
structed using the Hilbert transform (see §2.2.3) and the phase-angle ϕ
was determined (see Huang et al. 1998, and figure 6.4(b)), and divided
into 20 phase-bins. Each phase-bin contained of the order 250 images.
The average instantaneous frequency varied 10% during the cycle, and
had a spread of 20% within each bin. Similar phase-averaging results
were obtained when velocity was used as a reference.

6.5   Uncertainty assessment

To establish the validity of the measured results, a detailed uncertainty
analysis was carried out. The root-mean-square (RMS) uncertainties
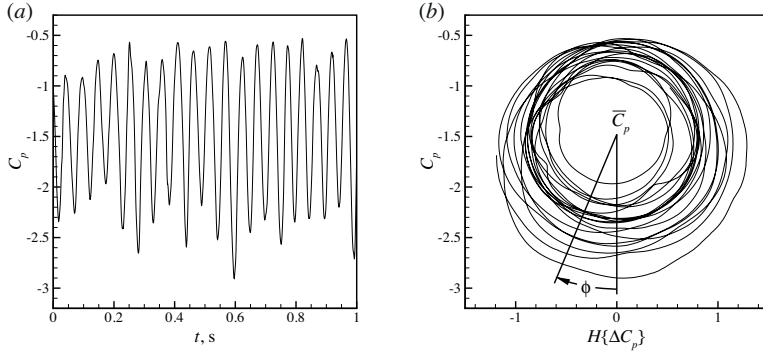in the statistical quantities, such as time-averaged velocity, Reynolds-

Figure 6.4: Determination of the phase variable $\phi(t)$. (*a*) low-pass filtered pressure signal time-series, C_p, (*b*) complex discrete analytic signal, where $\Delta C_p = C_p - \overline{C_p}$. The vertical axis represents the real part and the horizontal axis the imaginary part of the complex discrete analytic signal.

averaged normal stresses, and Reynolds-averaged shear stress, due to a finite number of samples, were determined following the work of Benedict & Gould (1996) (see §2.3) considering 5,456 velocity vector fields. The same approach was used to determine the RMS uncertainties on the phase-averaged and fluctuating phase-averaged velocity by assuming 250 velocity fields per phase-bin.

In addition, each instantaneous velocity vector is affected by measurement error and therefore has an associated RMS measurement uncertainty ε_u. Similarly, each velocity gradient has a RMS uncertainty (e.g. $\varepsilon_{du/dx}$). The magnitudes of these uncertainties in PIV are much more difficult to estimate than for the time-averaged and phase-averaged properties. They depend on a wide range of parameters, such as final interrogation window size, correlation mapping, magnification, particle image density, uncertainties on the particle displacements, the laser pulse separation, calibration procedure etc.

To estimate the uncertainty on the instantaneous velocity, velocity gradient, and vorticity quantities, a linear uncertainty-propagation analysis was used see §2.3 and §3.4. This analysis is limited, only gives a

Table 6.4: Uncertainty analysis for PIV-results, $Re_D = 9{,}500$.

	$\varepsilon(\%)$		$\varepsilon(\%)$		$\varepsilon(\%)$
$\overline{u}/U$	1.0	$\langle u\rangle/U$	3.8	u/U	1.5
$\overline{v}/U$	1.1	$\langle v\rangle/U$	3.5	v/U	1.5
$\overline{w}/U$	0.5	$\langle w\rangle/U$	3.4	w/U	2.1
$\overline{\omega_z}/\overline{\omega}_{max}$ †	0.9	$\langle\omega_z\rangle/\overline{\omega}_{max}$ †	3.5	$\omega_z/\overline{\omega}_{max}$ †	1.6
$\overline{u'u'}/U^2$	1.0	$\langle\hat{u}\hat{u}\rangle/U^2$	3.3		
$\overline{v'v'}/U^2$	1.3	$\langle\hat{v}\hat{v}\rangle/U^2$	2.8		
$\overline{w'w'}/U^2$	0.2	$\langle\hat{w}\hat{w}\rangle/U^2$	2.5		
$\overline{u'v'}/U^2$	0.5	$\langle\hat{u}\hat{v}\rangle/U^2$	1.5		

† $\overline{\omega}_{max} = 54\,U/D$, located in the shear-layer.

(linear) estimate of the uncertainty. However, this analysis gives an indication of the (order of magnitude) of the uncertainty. The results presented here are applicable to the streamwise component and the magnitude of the error on the crossflow velocity is taken to be the same as the streamwise component. Based on results from undisturbed flow for the stereo-PIV setup (with the model removed), uncertainty in determination of the cross-correlation peak location was found to be $\varepsilon_{cc} = 0.1$ pixel. A summary of the uncertainties for $Re_D = 9{,}500$ are provided in table 6.4. Due to the nature of the stereoscopic reconstruction, the out-of-plane velocity is very sensitive to misalignment in regions of strong spatial gradients of in-plane velocity. Despite correction for misalignment as described earlier, the out-of-plane velocity values in the initial shear-layer are likely to be affected by the remaining misalignment error. Finally, the uncertainty due to a limited number of vortex shedding cycles is estimated assuming a maximum deviation of half a cycle with respect to the number of cycles measured. This results in an uncertainty of 1.3%.

Chapter 7

Experimental assessment

The flow around a square cylinder at a Reynolds number of 9,500 was found to be predominantly 2D along the side-wall of the cylinder, whereas the wake flow was found to have considerable 3D fluctuations, see §8 for more details (see also de Kat et al. 2009*a*,*b*). Applying both stereo-PIV and tomo-PIV to the square cylinder problem, we will describe the performance of pressure evaluation under 2D and 3D flow around a square cylinder and how it connects to the theoretical performance estimation and the numerical assessment of the preceding chapters. First we present the results from stereo-PIV to show what accuracy the pressure evaluation can achieve using planar PIV. Secondly, the tomo-PIV results are used to assess the influence of 3D flow effects and to what extent the pressure evaluation improves with inclusion of the 3D flow terms. Next, power spectra are presented to assess the frequencies that are captured properly by pressure-PIV. Finally the results are compared with the results from the theoretical considerations in chapter 4 and the test-case on the synthetic velocity field of chapter 5.

7.1   Pressure-PIV results

It is easy with a performance assessment on a synthetic flow to isolate different influences, but it poses considerable difficulty with experimental results, where one has to deal with multiple responses at once (e.g. noise and signal). Therefore we will change the approach with respect

to the approach taken in chapter 5. The pressure signals from pressure-PIV are compared with pressure signals from the pressure transducer measurements. The signal from the pressure transducer measurement is taken as reference, p_{ref}. Using this reference signal, the mean response, $\overline{p}/\overline{p}_{ref}$, will give information on how well the time-averaged value of the pressure signals correspond. A poor mean response implies that there also will be a poor instantaneous response. With a good mean response, then with the RMS response, σ_p/σ_{ref}, and the correlation between the signals gives an indication of how well the fluctuations around the mean are captured. The better the fluctuations are captured the better the instantaneous description of the pressure signal.

In the absence of noise, the RMS response is a measure for the peak response. In the presence of measurement noise, however, the RMS response gives the combination of the peak response and the noise response. Therefore, the RMS response alone is not a good measure to make statements about the quality of the instantaneous description of the pressure. The correlation value between the pressure signals from pressure-PIV and from the pressure transducers gives an indication of how well the signals are aligned in time. It, however, does not provide any insight into the amplitude behaviour. Combining the RMS response and correlation values between the signals, statements can be made about the quality of the instantaneous description of the pressure signal.

7.1.1   Stereo-PIV

A typical result for stereo-PIV is shown in figure 7.1, where the relation between separated high vorticity regions and low pressure regions is illustrated, especially apparent along the bottom side of the square cylinder. In the wake the relatively large low pressure region can be associated to the formation of a Von Kármán vortex, which is more clearly visible when considering phase-averaged results (see chapter 8 or e.g. van Oudheusden et al. 2005, de Kat et al. 2010).

Figure 7.2 shows pressure signal time-series extracted from the pressure fields derived from stereo-PIV using the Eulerian approach compared to the pressure transducer signals. The signals for the side-wall (figure 7.2, top) are in good agreement and show a clear periodic com-
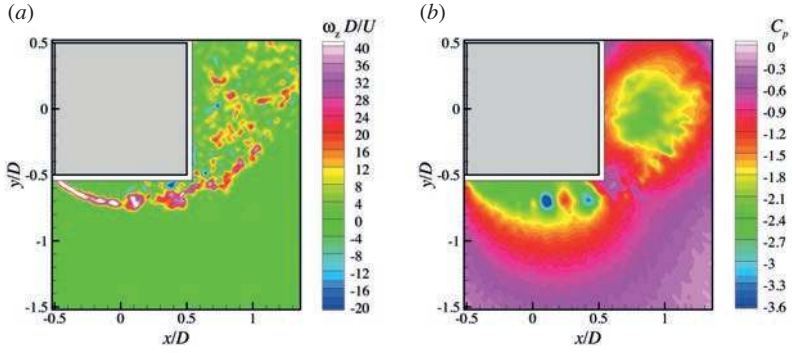
Figure 7.1: Example of the stereo-PIV results. (*a*) out-of-plane vorticity. (*b*) pressure field.
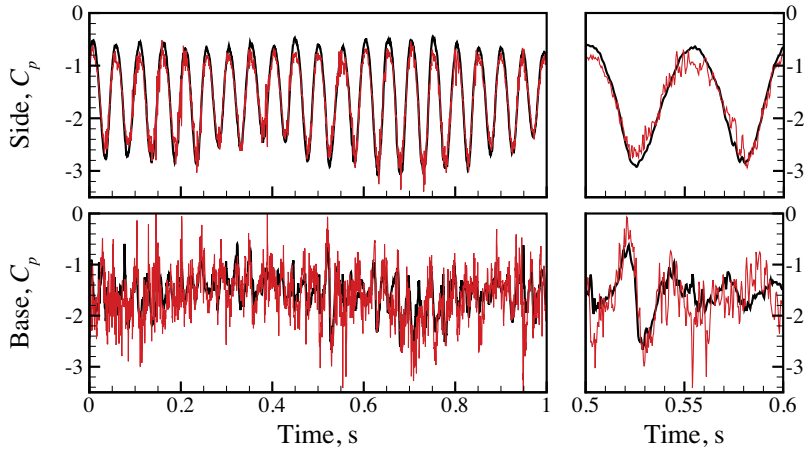

Figure 7.2: Pressure signal time-series from stereo-PIV. The pressure signal from PIV is shown in *red*. The pressure transducer signal is shown in *black*. *Top*: side-wall signals. *Bottom*: base-wall signals. *Left*: full time-series. *Right*: 0.1 s sub-set of the time-series.

ponent as a consequence of the Von Kármán vortex shedding, whereas
the signals for the base-wall (figure 7.2, bottom) show a fair agreement
and the periodicity is less evident. To quantify the agreement between
the signals and to investigate the effects of spatial and temporal reso-
lution, the mean and RMS responses as well as the cross-correlation
values with respect to the pressure transducer signal are shown in fig-
ures 7.3-7.5 and 7.6-7.8 for the side and base-wall, respectively. As a
comparative reference (to indicate spanwise coherency), values deter-
mined from pressure transducers on either side of the PIV domain are
indicated in grey. The mean and RMS responses of these transducers
are compared with each other, taking each as the reference for the other,
which results in two values for the mean and RMS response. Also the
correlation between the two pressure transducer signals is determined.

Figure 7.3 shows the mean response for the side-wall pressure sig-
nal obtained from stereo-PIV. The relative mean responses of the trans-
ducers with respect to each other have a difference of about 1% with re-
spect to the ideal response. This small difference could be due to small
spanwise differences in the flow or a small difference in the response of
the transducers. The influence of spatial resolution, figure 7.3(*a*), shows
that both the Eulerian and the Lagrangian approach react similar and are
within 5% for all *WS* and OF. At the highest spatial resolution (small
WS) the response is an over-expression of 5%, whereas the response at
the lowest spatial resolution (big *WS*) results in a 5% reduction of the
mean response. The main contributor to the mean pressure is the curved
flow (i.e. the mean advective part, fluctuation play a smaller role), the
reduction in mean response can be attributed to the spatial filtering of
the flow curvature, but the effects are limited. The influence of temporal
resolution, figure 7.3(*b*), shows a clear difference between the Eulerian
and the Lagrangian approach. The Eulerian approach is hardly affected
by a change in temporal resolution, since the flow along the side-wall of
the square cylinder is predominantly 2D and there are no vortical struc-
tures passing the pressure evaluation domain close to the location the
pressure is extracted, which agrees well with the findings for pressure
determination on the advecting vortex in chapter 5. The Lagrangian
approach shows a distinct drop off for $\Delta t\, U/D > 0.1$. The structures
next to the side of the square cylinder (figure 7.1 shows two structures
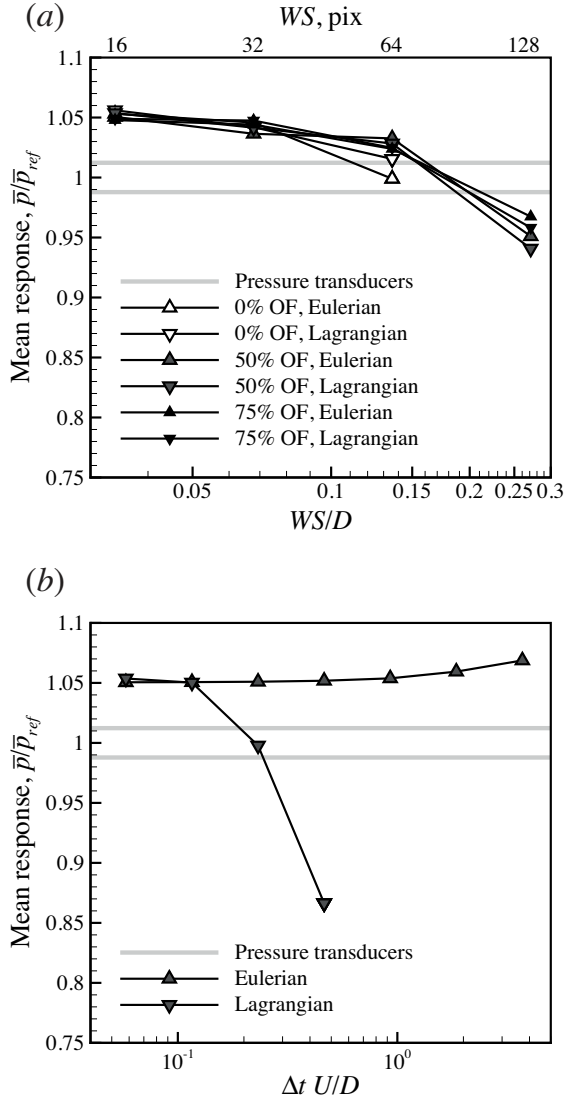that are stronger than average) have an average maximum vorticity of

Figure 7.3: Mean response to spatial and temporal influences on the side-wall pressure signal from stereo-PIV. (*a*) Influence of spatial resolution. (*b*) Influence of temporal resolution.

around 30 U/D, resulting in a vortex turnover time (assuming a Gaussian vortex) of $\Delta t\, U/D \approx 0.3$, which shows that the drop off of the mean response is linked to the turnover time of the vortical structures along the side of the square cylinder. Where a drop off of peak response is expected to be linked with the vortex turnover time, this shows that the vortex turnover time has a significant effect on the mean response as well.

Figure 7.4 shows the RMS response for the side-wall pressure signal. The relative RMS responses of the pressure transducers are virtually identical (a difference of $< 0.5\%$, the two lines indicating them have even merged into one line). In figure 7.4(a) the influence of the spatial resolution on the RMS response. The RMS response of the Eulerian and Lagrangian approaches both perform very similar and no significant differences can be found. For high spatial resolutions (small *WS*) all OF give similar results, having a RMS response of 0.9. For lower spatial resolutions and 75% OF the response stays nearly the same, whereas for 50% and 0% OF the RMS response drops to ≈ 0.8 for *WS* of 128 and 64 pixels, respectively. The structures along the side of the square cylinder are of the order of 0.1 D (see figure 7.1). The drop of the RMS responses of the 0% and 50% OF seem to coincide with this length scale. The influence of the temporal resolution on the RMS response,7.4(b), shows a similar trend as the mean response (compare with figure 7.3(b)), having a almost constant value for the Eulerian approach and a drop off for $\Delta t\, U/D > 0.1$ for the Lagrangian approach. There is a slight increase (about 5%) in the RMS response for the Eulerian approach for lower temporal resolutions (large Δt) with respect to the value of 0.9 the RMS has for the highest temporal resolution. No clear explanation for this little increase can be found at present, but perhaps the flow along the side of the cylinder is dominated by spatial curvature of the fluid flow and affected less by the time dependent term, see 4.1, and by omitting the time dependent term the results becomes more accurate. The drop off of the Lagrangian approach for the RMS response is expected and can be explained by the estimate of the vortex turnover time of the structures along the side of the square cylinder, which is $\Delta t\, U/D \approx 0.3$ (see previous paragraph).

The RMS response gives an indication of the correctness of the magnitude of the amplitude of the fluctuations. To check whether the
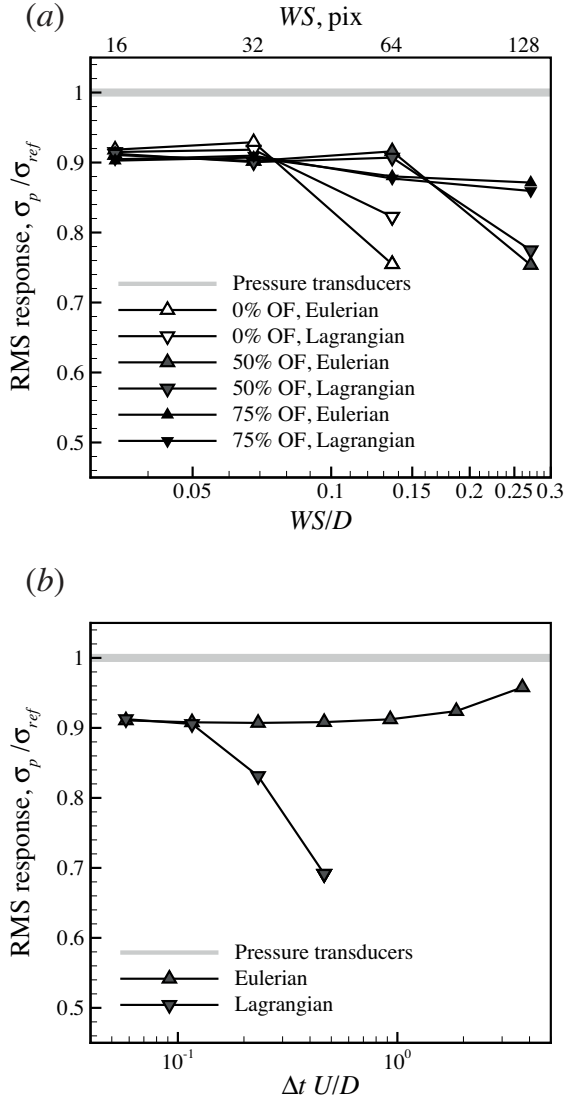
Figure 7.4: RMS response to spatial and temporal influences on the side-wall pressure signal from stereo-PIV. (*a*) Influence of spatial resolution. (*b*) Influence of temporal resolution.
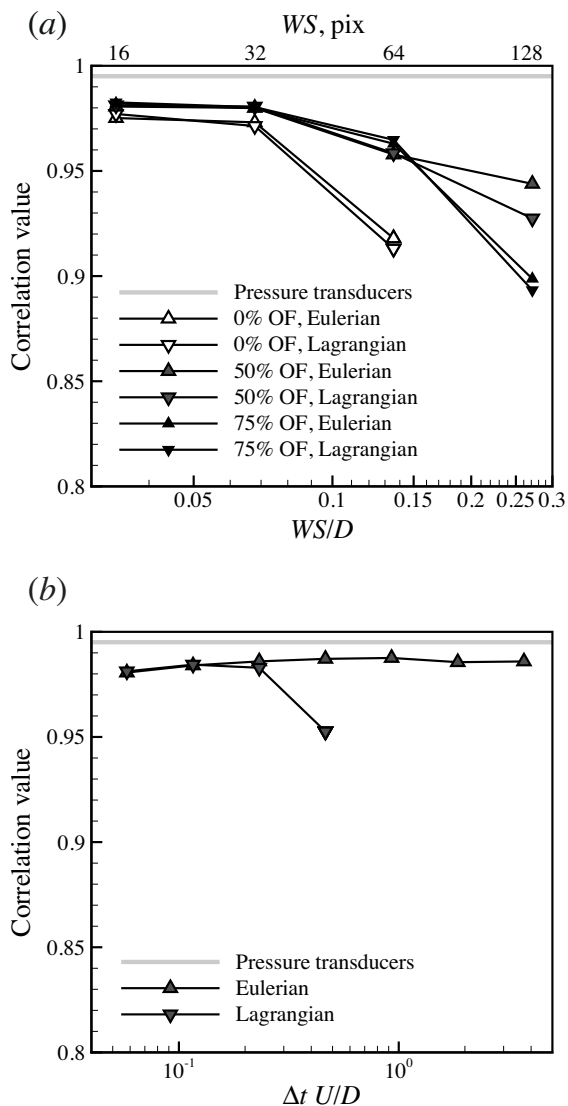
Figure 7.5: Correlation values for the spatial and temporal influences on the side-wall pressure signal from stereo-PIV. (*a*) Influence of spatial resolution. (*b*) Influence of temporal resolution.

fluctuations occur at the same time we need to look at the correlation between the signals. Figure 7.5 shows the correlation values between the signals from pressure-PIV and the pressure transducer. The influence of the spatial resolution, shown in figure 7.5(*a*), displays the same trend as the mean and RMS responses, decreasing in value for decreasing spatial resolution (bigger *WS*) and small differences are found between the Eulerian and the Lagrangian approach. The best results are found for *WS* with sides of 16 or 32 pixels and an OF of 50% or 75%. The results for an OF of 0% are lower in all cases. The difference between the 50% and 75% OF is less obvious. For a *WS* side of 64 the 75% OF has a slightly better correlation value, but for a *WS* with side 128 pixels the 50% OF has better correlation value than the 75% OF. The 50% OF for this *WS* also has a lower RMS response, which could indicate a stronger modulation (loss of amplitude response), but less noise (loss of correlation). The influence of the temporal correlation, figure 7.5(*b*), shows that the correlation for the Lagrangian approach drops off at a slightly later stage than the drop off of the mean and RMS responses, at $\Delta t\, U/D \approx 0.2$ versus $\Delta t\, U/D \approx 0.1$ for the mean and RMS responses.

The flow along the side of the square cylinder is predominantly 2D (see chapter 8), which can also be inferred from RMS response relative to each other and the correlation between the pressure transducers on either side of the measurement domain (both approximately 1). The preceding results can therefore be taken to be representative for the performance of pressure from stereo-PIV in 2D flow (planar-PIV would give similar results, since the third component of velocity is useless unless the out-of-plane component of the velocity gradient is also available). We now turn our attention to the performance of pressure from stereo-PIV in 3D and we look at the responses for the pressure signals at the base of the square cylinder.

Figure 7.6 shows the mean response for the base-wall pressure signals. Interestingly the mean response is larger than unity and is increasing with increasing *WS*, see figure 7.6(*a*). This suggests that the signal is influenced by noise (measurement noise or incorrect capturing of the pressure gradient). Nevertheless, the mean responses for the different OF converge to a deviation of approximately 10% from the reference value for $WS/D \approx 0.035$ (*WS* with sides of 16 pixels). The difference in response between the OFs is more evident than for the side-wall mean
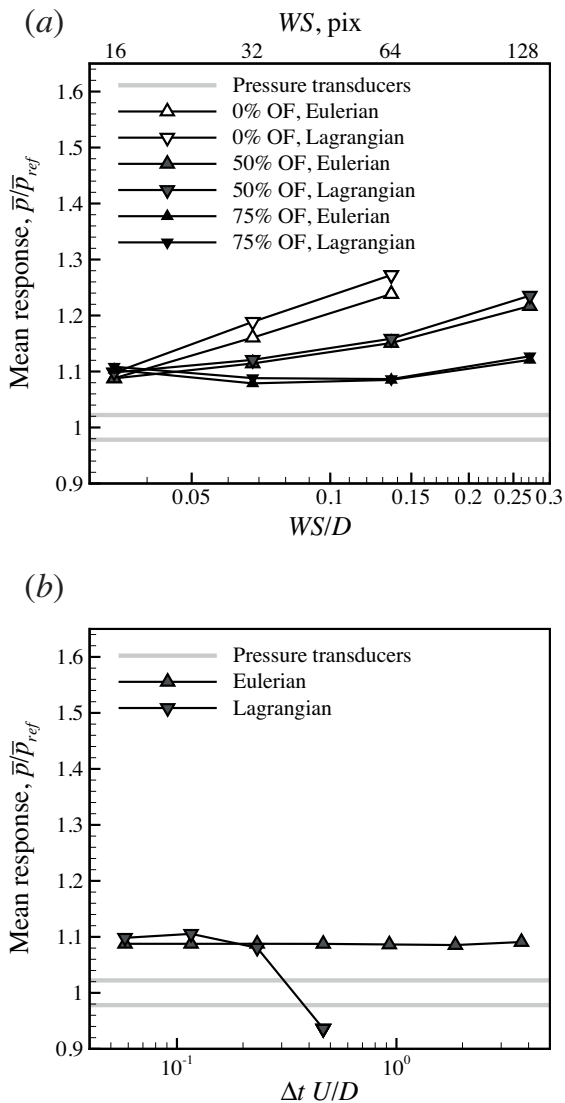
Figure 7.6: Mean response to spatial and temporal influences on the base-wall pressure signal from stereo-PIV. (*a*) Influence of spatial resolution. (*b*) Influence of temporal resolution.

response, where there was no discernible difference (see figure 7.3(*a*)). As expected 0% OF performs worse than 50% that in its turn performs worse than 75% OF. The vortical structures in the wake near the base go down to sizes of approximately 0.05*D*, which would explain the similar responses of the different OF for *WS*/*D* < 0.05. Figure 7.6(*b*), shows the influence of the temporal resolution, which is very similar to that of the side-wall mean response (figure 7.3(*b*)). The Eulerian approach is not affected by the temporal resolution, having a difference of approximately 10% with the reference. The Lagrangian approach drops off at $\Delta t U/D \approx 0.25$, which agrees with the vortex turnover time corresponding to $\Delta t\, U/D \approx 0.6$ (structures next to the base of the square cylinder have a peak vorticity of approximately 15 *U*/*D* and again assuming a Gaussian vortex). For better resolutions than $\Delta t\, U/D \approx 0.25$ (smaller Δt) the Lagrangian approach also has difference of approximately 10% with the reference.

Figure 7.7 shows the RMS response for the base-wall pressure signals. Like the mean response they show that the pressure from stereo-PIV is over-predicts the response with respect to the reference. The response with the spatial resolution in figure 7.7(*a*) shows that the results for the different OF converge to a deviation of approximately 50% with respect to the reference for *WS*/*D* ≈ 0.035 (*WS* with sides of 16 pixels). From that point the deviation from the reference for 0% OF increases with decreasing resolution (increasing *WS*), the deviation for 50% OF stays almost the same, only increasing for the coarser resolutions (*WS*/*D* > 0.15), and the deviation for 75% OF even decreases a bit with decreasing resolution. The influence of the temporal resolution, figure 7.7(*b*), shows that the deviation for the Eulerian approach first decreases slightly and for $\Delta t U/D > 2$ is increases significantly. The Kármán shedding gives us two vortices per cycle (one clockwise and one counter-clockwise) resulting in a frequency in the pressure fluctuations that is twice the shedding frequency, corresponding to $\Delta t\, U/D \approx 4$. The significant increase of the deviation in RMS response of the Eulerian approach is clearly linked with the Kármán shedding. The RMS response of the Lagrangian approach shows only small changes, first decreasing slightly and then slightly increasing, but not exceeding a deviation of approximately 50% for the range of measured resolutions. This is in contrast with the mean response, figure 7.6(*b*), where a clear
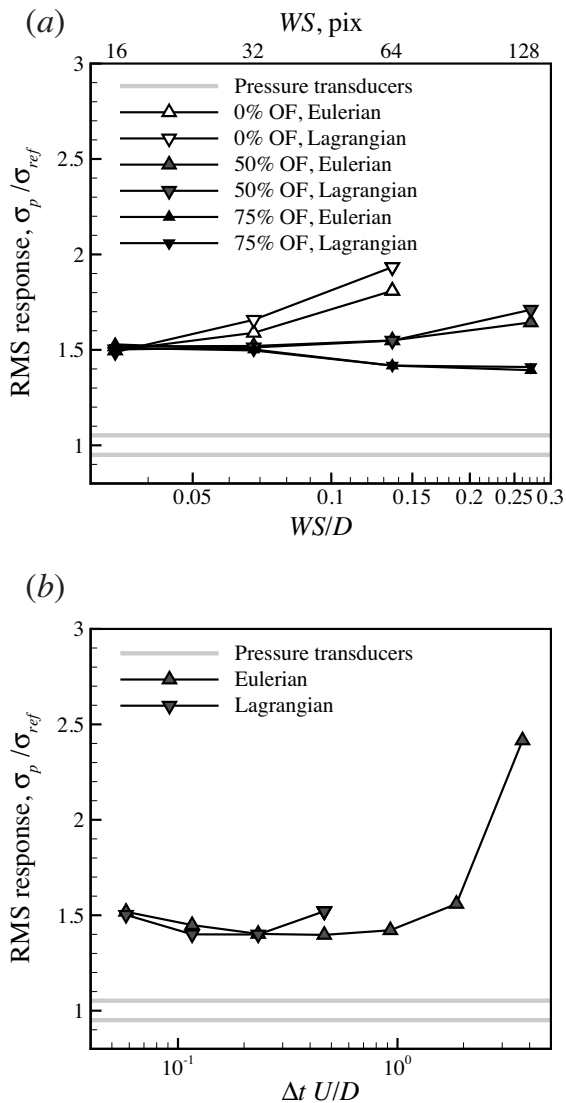
Figure 7.7: RMS response to spatial and temporal influences on the base-wall pressure signal from stereo-PIV. (*a*) Influence of spatial resolution. (*b*) Influence of temporal resolution.

departure is observed for $\Delta t\, U/D > 0.2$.

The correlation values of the pressure signals from pressure-PIV and the pressure transducers are shown in figure 7.8. The correlation between the pressure transducers on either side of the measurement plane (from the transducer setup for the tomo-PIV experiment) were found to be approximately 0.8 and are shown in grey. This is a clear difference in spanwise correlation with respect to the result for the side-wall pressure signal. The correlation is still strong, but the value decreased significantly (0.8 versus 1 for base-wall and side-wall, respectively), indicating that there is 3D flow present. Figure 7.8(*a*) shows that changing the spatial resolutions has no significant effect on the correlation. The correlation has a value of approximately 0.6 for all *WS* and OF, except for 0% OF that shows a mild decrease with increasing *WS*. The influence of the temporal resolution, figure 7.8(*b*) for the Eulerian approach shows that the correlation first increases slightly from approximately 0.57 at $\Delta t\, U/D \approx 0.05$ to 0.65 at $\Delta t\, U/D \approx 1$ and then decreases significantly for $\Delta t\, U/D > 2$. This matches with the trend for the RMS response with temporal resolution, see figure 7.7(*b*). The Lagrangian approach shows a similar increase, but drops off for $\Delta t\, U/D > 0.2$, which agrees with the observation for the mean response. This drop off is related to the vortex turnover time that corresponds to $\Delta t\, U/D \approx 0.6$.

The flow in the wake of the cylinder has a significant 3D element to it (see chapter 8) as indicated by the spanwise correlation of the base-wall pressure transducers. The results for the base-wall pressure signals from stereo-PIV give a good indication of what a strictly planar velocity input can give in pressure estimates in a 3D flow. However, the results show a few interesting trends that can only be ascribed to noise or 3D flow if we include the third direction in the input and see what the influence of adding/removing it does to the performance of the pressure determination. Therefore, we will now focus on the wake and assess the results for pressure determination from tomo-PIV.

7.1.2 Tomo-PIV

The results for the base-wall pressure signal from stereo-PIV lack the full 3D velocity information needed for correct pressure determination in a 3D flow, even for the case where pressure is determined only in
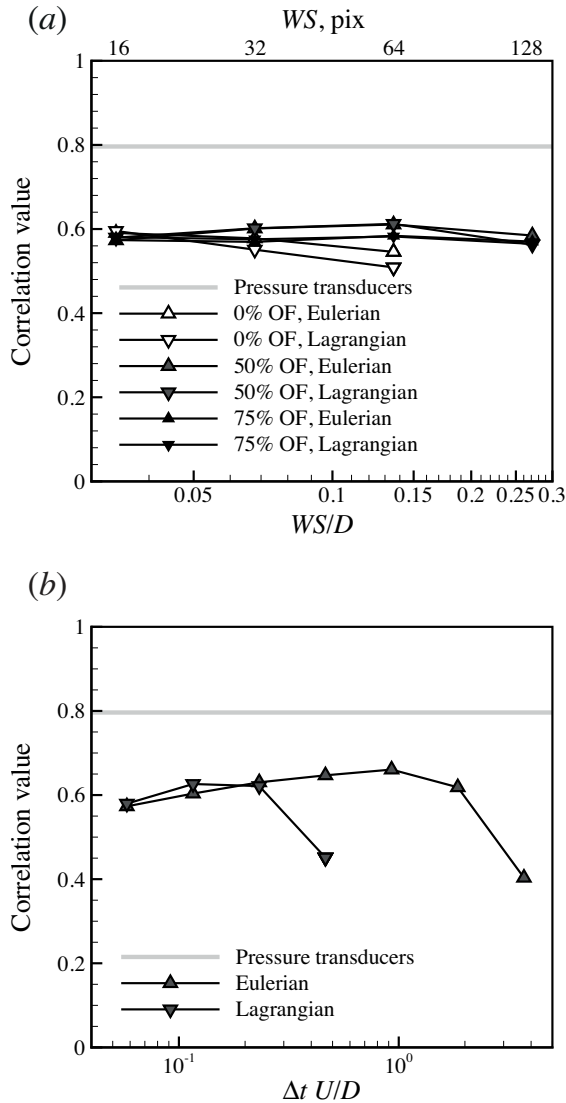
Figure 7.8: Correlation values for spatial and temporal influences on the base-wall pressure signal from stereo-PIV. (*a*) Influence of spatial resolution. (*b*) Influence of temporal resolution.
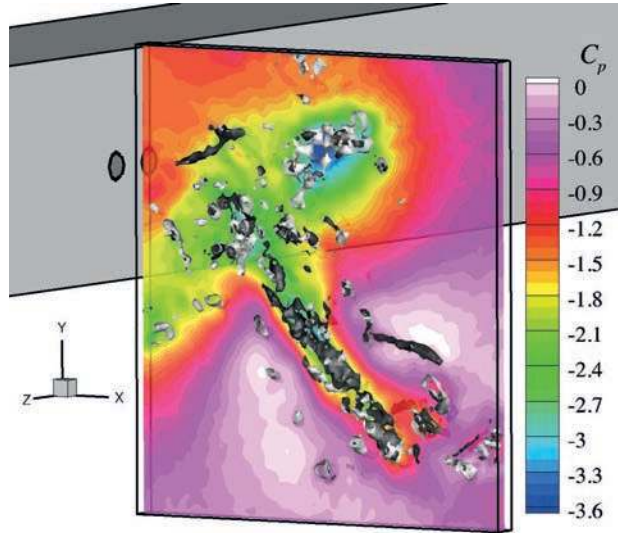
Figure 7.9: Example of the tomo-PIV results. Isosurfaces of out-of-plane vorticity are shown in *light grey*, $\omega_z = 15\, D/U$. Isosurfaces of in-plane vorticity are shown in *dark grey*, $\sqrt{\omega_x^2 + \omega_y^2} = 20\, D/U$.

a cross-sectional plane. To assess the effect of the omission of the 3D terms, tomo-PIV experiments were performed. The main difference between the Eulerian and Lagrangian approach seems be related to the temporal resolution, therefore, we focus on a single combination of interrogation volume (3D equivalent of *WS*) and OF ($16 \times 16 \times 16$ pixels and 50% OF) and investigate the influence of temporal resolution.

Figure 7.9 shows an example of the results from tomo-PIV. The isosurfaces clearly indicate the 3D nature of the flow in the wake. The mid-plane, where data is extracted to determine the planar pressure, is flooded with the corresponding pressure field (determined with the Eulerian approach and the full velocity and velocity gradient fields as input). Low pressure regions are located near the regions of high in-plane and/or out-of-plane vorticity, showing that the pressure field is influenced by the 3D nature of the flow. The locations of the base-wall
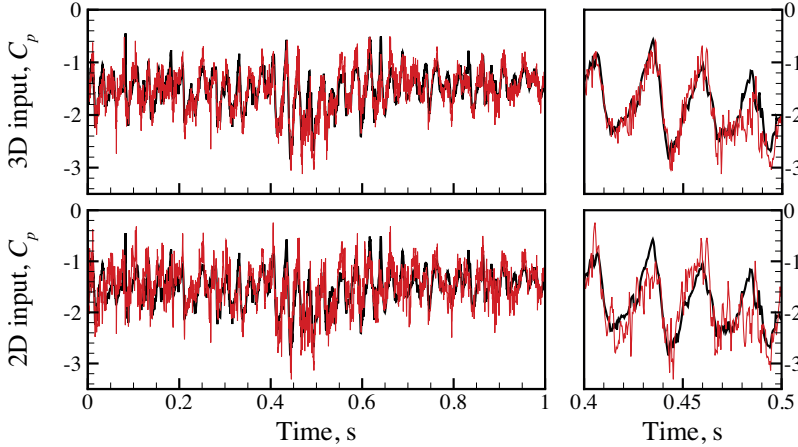
Figure 7.10: Base-wall pressure signal time-series from Tomo-PIV, Eulerian approach. The pressure signal from PIV is shown in *red*. The pressure transducer signal is shown in *black*. *Top*: 3D input. *Bottom*: 2D input. *Left*: full time-series. *Right*: 0.1 s sub-set of the time-series.

pressure transducers on either side of the measurement volume are also depicted in figure 7.9.

Figure 7.10 shows the pressure signal time-series from tomo-PIV using the Eulerian approach compared with the signal from the pressure transducer that is depicted behind the measurement volume in figure 7.9. Both results with input from the full 3D information (figure 7.10, top) and a 2D subset (figure 7.10, bottom) of the tomo-PIV data are shown. The difference between these results indicates the influence of adding or omitting the extra 3D information. They both seem to have a good agreement with the pressure transducer signal, where the signal for the 3D input seems to be in better agreement. To quantitatively assess the performance of the pressure determination and to compare the different methods (analogous to the way the stereo-PIV results were assessed) the mean response, the RMS response and the cross-correlation values are determined for different time separations, Δt, and shown in figure 7.11 and 7.12. Due to the limited thickness of the volume only the

smallest time separation gave results for the 3D Lagrangian approach. Even for this case the pressure gradient at some points could not be determined, i.e. the fluid path could not be reconstructed due to too large values of the out-of-plane velocity. In order to work with larger time separations the volume thickness should be increased.

The mean response, RMS response and correlation values for the base-wall pressure signals based on a 2D subset of the information from tomo-PIV show similar trends as the results from stereo-PIV. This is especially apparent when comparing figure 7.11(*a*) with 7.6(*b*), figure 7.11(*b*) with 7.7(*b*), and figure 7.12 with 7.8(*b*). This similarity in trends indicates that the same effects are present in both the data-sets and that the tomo-PIV data can be used to assess the influence of lack of out-of-plane information for planar- or stereo-PIV (even though for stereo-PIV the out-of-plane velocity *is* know, this is of no use since the out-of-plane gradient of both the in-plane velocity-components is needed).

The mean response in figure 7.11(*a*) shows that the results for the Eulerian approach with 2D input are constant for all temporal resolutions observed and has a difference of approximately 3% with respect to the reference signal. The Eulerian approach with 3D input shows exactly the same behaviour, but has a smaller difference of approximately 1%. The Lagrangian approach with 2D input has a difference of approximately 2% before it drops off for $\Delta t\, U/D > 0.2$. The Lagrangian approach with 3D input has a difference of approximately 4%, but it was only possible to determine the pressure gradient for one temporal resolution. The influence of the full information in does not change the mean response significantly (most likely due to the fact that the mean flow is 2D, see chapter 8). The RMS response, figure 7.11(*b*), shows a more distinct difference between the results for the 3D input and the 2D input. The Eulerian approach with 2D input shows a decrease from approximately 30% deviation at $\Delta t\, U/D \approx 0.06$ to approximately 25% deviation at $\Delta t\, U/D \approx 0.2$ and then the deviation increases significantly with decreasing temporal resolution (increasing Δt) for $\Delta t\, U/D > 0.5$. The deviation for Lagrangian approach with 2D input starts at the same value, decreases slightly and then increases significantly for $\Delta t\, U/D > 0.2$. The deviation for the Eulerian approach with 3D input starts with a deviation of just under 20% at $\Delta t\, U/D \approx 0.06$ and then increases for decreasing temporal resolution. The result for the Lagrangian ap-
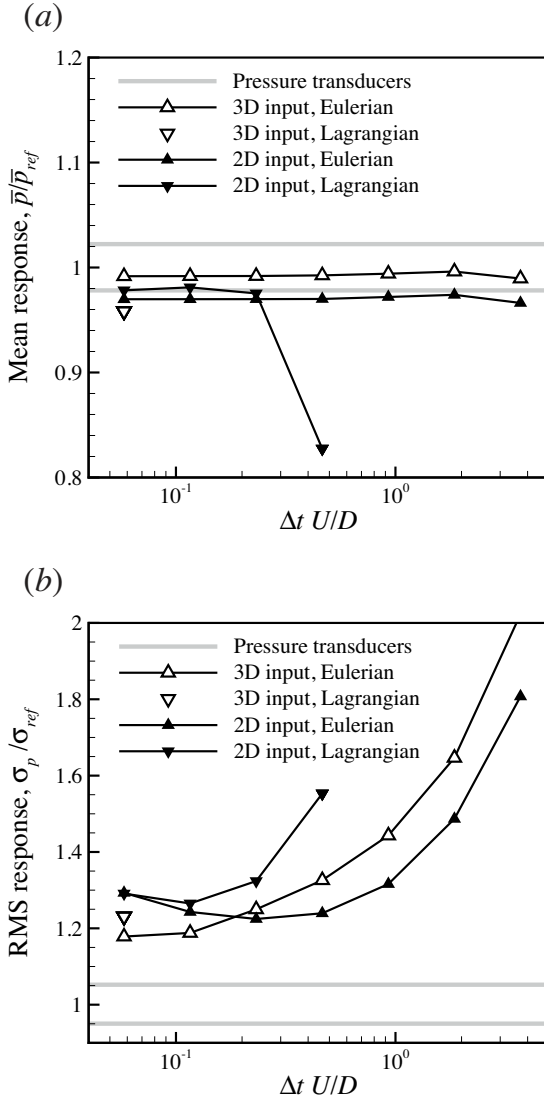
Figure 7.11: Mean response and RMS response to temporal influences on the base-wall pressure signal from tomo-PIV. (*a*) Mean response. (*b*) RMS response.
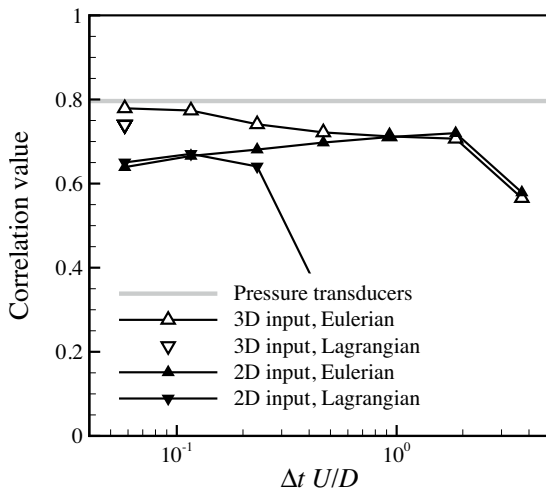
Figure 7.12: Correlation values for the temporal influences on the base-wall pressure signal from tomo-PIV.

proach with 3D input has deviation of just over 20%.

Figure 7.12 shows the correlation values with the temporal resolution. The most obvious difference that strikes the eye is that the correlation values for the 3D input at the highest temporal resolution (smallest Δt) are significantly higher than the correlation values for the 2D input. The correlation for the Eulerian approach with 3D input has a maximum correlation value of just under 0.8, which is very close to the spanwise correlation between the pressure transducers of 0.8. Starting at the highest temporal frequency ($\Delta t\,U/D \approx 0.06$) with the correlation of just under 0.8, there is a gradual decrease in correlation value to approximately 0.7 at $\Delta t\,U/D \approx 2$ and then there is an abrupt drop for $\Delta t\,U/D > 2$. The Eulerian approach with 2D input shows a gradual increase from 0.65 at $\Delta t\,U/D \approx 0.06$ to 0.7 at $\Delta t\,U/D \approx 2$ and then drops off for $\Delta t\,U/D > 2$. It has approximately the same values as the results for the 3D input for $\Delta t\,U/D > 0.5$. The Lagrangian approach with 2D input starts the same as the Eulerian approach, but drops off earlier for

$\Delta t \, U/D > 0.2$.

7.1.3   Spectral assessment

To assess the range of frequencies that can captured with pressure determination, power spectral density of the side-wall and base-wall pressure signals obtained from stereo-PIV and tomo-PIV, respectively, are determined. Figure 7.13(*a-b*)*top* shows the spectral density for the main test cases (see table 6.3) alongside with the power spectral density of the corresponding pressure transducer signal. The dynamic correlation between the PIV and corresponding pressure transducer signals are shown in figure 7.13(*a-b*)*bottom*. For the side-wall, results from the Eulerian approach are shown. The results for the Lagrangian approach are practically the same. For the base-wall, only results from the Eulerian approach are shown. The side-wall pressure shows a pronounced peak at the shedding frequency (20 Hz), while the base pressure displays a slightly less pronounced peak at double the shedding frequency. The power spectral density for the side-wall from stereo-PIV (7.13(*a*)*top*) shows an excellent agreement up to approximately 80 Hz where the pressure from PIV spectrum departs abruptly from that of the pressure transducer. The dynamic correlation (7.13(*a*)*bottom*) also shows an abrupt drop from near unity to zero in the range 50-70 Hz. This abrupt difference in amplitude (energy) and correlation can be attributed to the small 3D component in the shear-layer. De Kat et al. (2009*a*) show that, even though the flow along the side of the cylinder is predominantly 2D, the shear-layer has significant 3D fluctuations near the trailing edge of the model, which are caused by the shear-layer undergoing transition. The shear-layer has a frequency in the range of 10^2 to 10^3 Hz, which coincides with the region where the two spectra differ. The power spectral density for the base-wall from tomo-PIV (7.13(*b*)*top*) shows an excellent agreement up to 200 to 300 Hz. The dynamic correlation shows that there is good correlation between the signals before it drops to zero around 200 Hz. The small differences in the low frequency range can be ascribed to the limited number of cycles to get a good converged spectrum at these frequencies. The power spectral density that is obtained with 2D input is shown as well and shows similar agreement as the result with 3D input up to 80Hz. This
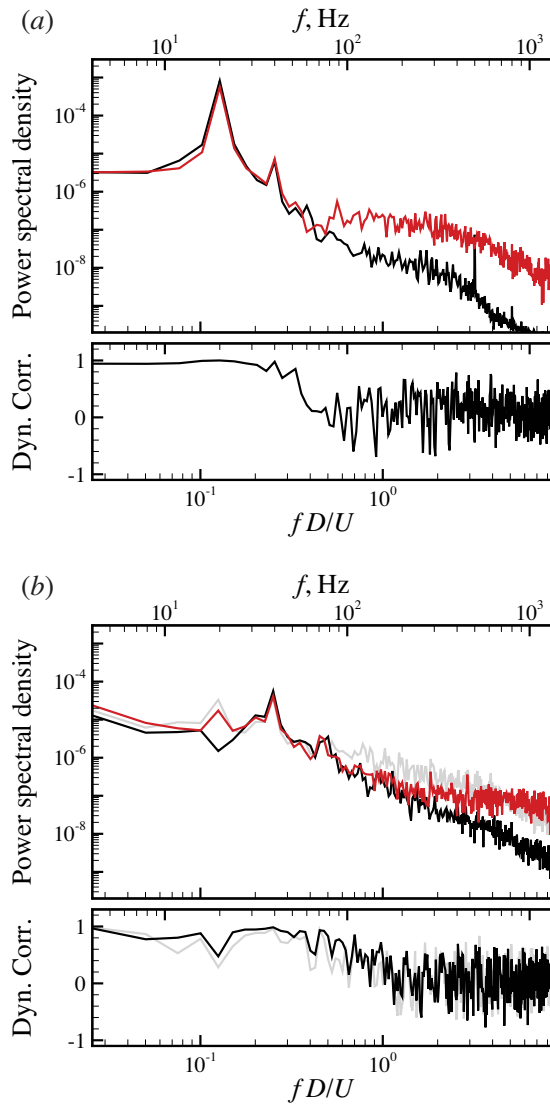
Figure 7.13: Power spectral density plots (*top*) and dynamic correlation plots (*bottom*) for the main PIV cases (see table 6.3). The spectrum for pressure from PIV is shown in *red*. The spectrum for the pressure transducer is shown in *black*. (*a*) Side wall, Stereo-PIV, Eulerian. (*b*) Base-wall, Tomo-PIV, Eulerian. Results for 2D input are shown in *grey*.

indicates that the pressure influence of the big 2D vortices are still captured correctly. Between circa 100 and 800 Hz, the results with 2D and 3D inputs display a difference, which is related to the 3D flow introduced by shear-layer transition. This range matches the range where the results from stereo-PIV perform worse for the side-wall pressure. The dynamic correlation (7.13(*b*)*bottom*) shows that the result with 2D input has a lower correlation for almost the complete frequency range than the result with 3D input.

In figure 7.14, results are shown for a larger time step ($\Delta t = 8\Delta t_{min}$, where Δt_{min} is the smallest available velocity field time separation). These results give insight into the different techniques respond to a coarser time-resolution. For comparison the results for $\Delta t = \Delta t_{min}$ are shown in grey. Figure 7.14(*a*) shows the side-wall pressure results from stereo-PIV with the Lagrangian approach. The power spectral density has changed considerably. However, the main peak is still captured correctly. The dynamic correlation shows that except for the main frequency the correlation goes down. Correlation deteriorates for lower frequencies than the dominant one (lower than 20 Hz) and the drop in correlation has moved to a lower frequency, from 50-70 Hz to 30-40 Hz. Where before this drop was associated with the 3D nature of the shear-layer transition, now, is likely to be related to the temporal resolution limitations of the technique. The value of the expected limit for this (reduced) acquisition frequency ($f_{acq}/10 \approx 33$ Hz) coincides with the location where the drop is observed. In contrast to this, the results for the Eulerian approach (not shown) are the same as the results for Δt_{min}, showing only very small changes, indicating that for the side-wall pressure the advective part is dominant and the local acceleration only plays a minor role in the flow currently investigated.

Figure 7.14(*b*) shows the base-wall pressure results from tomo-PIV. For the 3D input base-wall case, the effect of Δt is similar to the effect on the Eulerian approach for the side-wall pressure. The main differences are that the power spectral density for frequencies higher than 80 Hz are higher and thus further away from the reference. However, the dynamic correlation shows almost no change. This strengthens the indication that the local acceleration only plays a limited role in the pressure determination in the flow currently investigated.
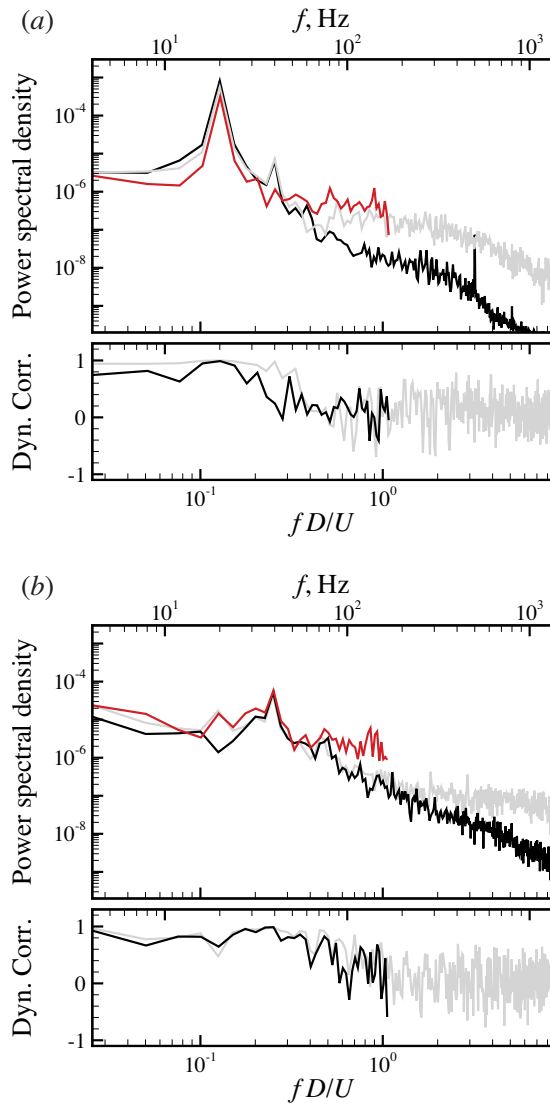
Figure 7.14: Power spectral density plots (*top*) and dynamic correlation plots (*bottom*) for $\Delta t = 8\Delta t_{min}$. The spectrum for pressure from PIV is shown in *red*. The spectrum for the pressure transducer is shown in *black*. For comparison results for $\Delta t = \Delta t_{min}$ are shown in *grey*. (*a*) Side wall, Stereo-PIV, Lagrangian. (*b*) Base-wall, Tomo-PIV, Eulerian.

7.2   Discussion

Although the experiments are not resolving all the structures in the flow (due to the limitation in spatial and temporal resolution), the results are sufficient to make statements regarding the performance of pressure determination from PIV.

The spatial resolution needed to successfully perform pressure-PIV can be inferred from the results for the predominantly 2D flow alongside of the square cylinder. For both the Eulerian and the Lagrangian approaches the restriction with respect to the spatial resolution were found to be the same. Figure 7.4(a) and 7.5(a) show that for a 50% OF and $WS/D < 0.1$ the RMS response is approximately 0.9 and the correlation value is approximately 0.98. For $WS/D < 0.2$ the RMS response is approximately 0.8 and the correlation value is approximately 0.95. Assuming $D \approx \lambda_x$ (see figure 7.1(a) where the large structure in the flow has a radius of approximately $D/2$) we get estimates of the spatial resolution of $WS/\lambda_x < 0.1$ and $WS/\lambda_x < 0.2$. In chapter 5 we found that for $WS/\lambda_x < 0.1$ the peak response was 0.95 and for $WS/\lambda_x < 0.2$ the peak response was 0.90. These values are very close, only differing 5%, and their differences are most likely caused by the presence of some 3D flow and the application of the boundary condition (equation 4.13). Therefore, It can be stated that to perform successful pressure-PIV a spatial resolution is needed that has at least more than five WS covering the structure under consideration. To improve the results and to obtain results accurate within 10% the spatial resolution has to be at least ten WS per flow structure.

The temporal resolution needed to successfully perform pressure-PIV is related to the approach used. When using the Lagrangian approach, the necessary temporal resolution is $f_{acq} > 10 \times f_{turnover}$, where $f_{turnover}$ is frequency related to the vortex turnover time, which is related to the Lagrangian time scales. This was shown in chapter 5, see figure 5.7(a), and is apparent from all the experimental results where the Lagrangian approach consistently drops off, when the temporal resolution comes closer to the resolutions corresponding to the (estimated) vortex turnover time. The Eulerian approach has a similar limitation, but now the limitation is related to the Eulerian time scale. For the Eulerian approach the results drop off when the temporal resolution approaches

the resolution corresponding to the advective frequency. This is shown for the large scale Kármán shedding, especially apparent in the correlation values for the base-wall pressure signal in figures 7.8(*b*) and 7.12. Furthermore, the spectral results for the base-wall pressure signal from tomo-PIV show a loss of coherence and a change of spectral power for $f_{flow} > 200 - 300$ Hz. This corresponds to $f_{acq}/f_{flow} > 13.5 - 9$, which is in good agreement with the requirement on the temporal resolution, $f_{acq}/f_{flow} > 10$. Spectral results for a reduced acquisition frequency show that the influence of the temporal resolution on the accuracy of the Eulerian approach is limited. Since the temporal resolution only affects the local acceleration term, this might indicate that (in the current flow problem considered) the advective term is dominant and that the local acceleration only plays a minor role.

The addition of the third component is necessary in order to successfully obtain the pressure from the velocity field in 3D flow. This is clearly shown by the correlation between the pressure-PIV results and the pressure transducer signal as well as the findings in chapter 5, where a peak response with a $\cos(\alpha)$ behaviour with the angle of the vortex axis with the measurement plane normal was found. However, the large scale structures in the wake, i.e. the Kármán vortices, are predominantly 2D (with the axis normal to the current measurement plane) and their influence is therefore already captured correctly by the planar description, as evidenced by the strong correlation (0.65) between the pressure signal from stereo-PIV and pressure transducer signal at the base-wall.

For the current flow problem, where the advective influences are small compared to the strength of the vortices, the restrictions on the Lagrangian approach (reconstruction of the fluid path) were found to be more limiting than the restrictions on the Eulerian approach (accurate estimation of the acceleration, especially near the domain edges).

The differences observed between the Eulerian approach, Lagrangian approach and the reference pressure are due to influences of 3D flow (for planar measurements) and spatial and temporal resolution, not due to measurement noise. Estimating U_a and V_p to be in the order of the freestream velocity, U ($\approx 2WS/\Delta t$), then, based on the analysis in §5 and $\sigma_u/U \approx 1.5\%$, the effect of noise is expected to be lower than 2%, which is well below the differences found due to the spatial and tempo-

ral resolution (and 3D flow).

Chapter 8

Square cylinder pressure

Now that the foundation for instantaneous planar pressure determination has been laid out, we turn our attention to the pressure around and loading on a square cylinder. For three different Reynolds numbers, time-averages, phase-averages and instantaneous pressure fields will be presented. For the phase-averaged results, side- and base-wall pressure evolution with phase will be shown. From the side- and base-wall pressure, periodic loading will be derived. Finally, instantaneous realisations are shown to see what structures contribute to the wall pressure, how they change with Reynolds number and where they originate.

8.1 Time-averaged pressure (mean loading)

Figure 8.1 shows time-averaged velocity magnitude and time-averaged pressure for $Re_D = 6,000$, 9,500, and 19,000. The velocity magnitude and pressure fields show good agreement for all Reynolds numbers and have only subtle changes with respect to one another. The saddle point in the wake was found to be located at $x/D = 1.26$, 1.09, and 1.19 for $Re_D = 6,000$, 9,500, and 19,000, respectively. This compares favourably with the results of van Oudheusden et al. (2005), who found a value of $x/D = 1.1$ at $Re_D = 10,000$. The pressure minimum in the wake was found to be $\overline{C}_p = $ -1.85, -1.84, and -1.81, for $Re_D = $ 6,000, 9,500, and 19,000, respectively. They were located at $x/D = $ 1.06, 0.95, and 1.03. The shape of the pressure and velocity results are
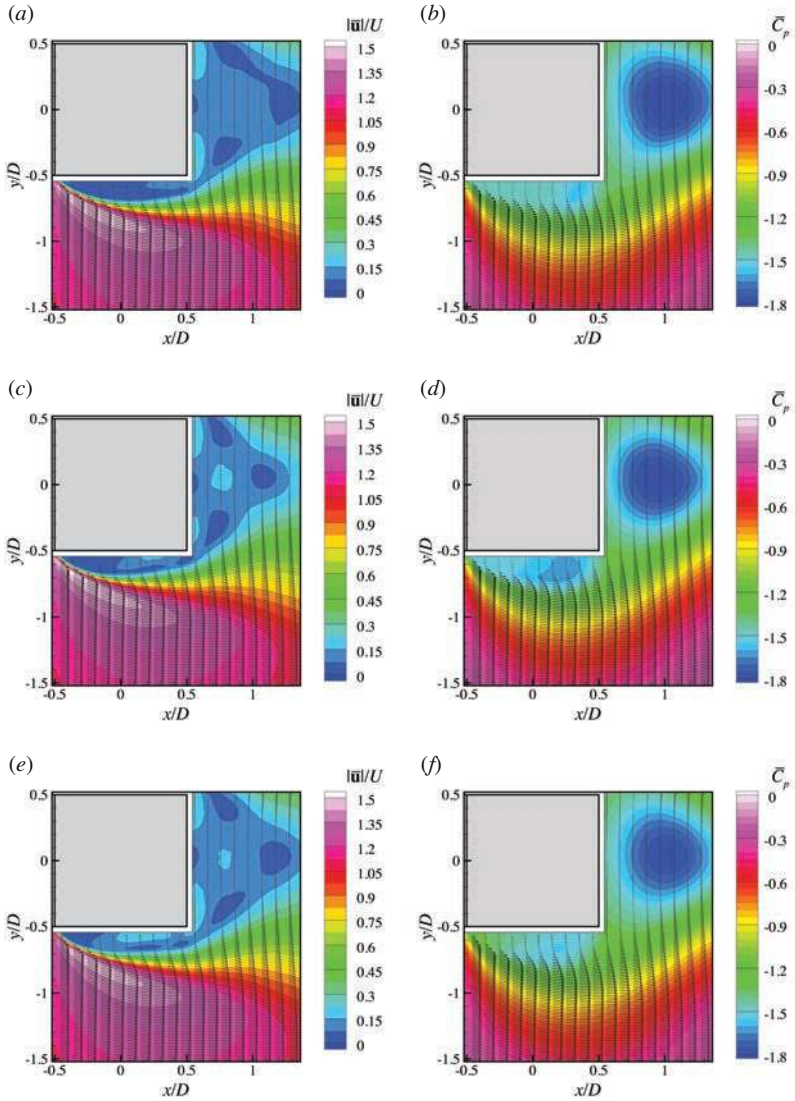
Figure 8.1: Time-averaged velocity magnitude and pressure. From *top* to *bottom*: $Re_D = 6{,}000$, $9{,}500$, and $19{,}000$. *Left* Velocity magnitude. *Right* Pressure. Each sixth vector in *x*-direction is shown.

Table 8.1: Side- and base-wall statistics for transducer and PIV

Re_D	$\overline{C}_p$ trans.	$\overline{C}_p$ PIV	$\overline{C'_p C'_p}$ trans.	$\overline{C'_p C'_p}$ PIV
Side-wall				
6,000	-1.39	-1.47	0.38	0.27
9,500	-1.51	-1.55	0.49	0.36
19,000	-1.48	-1.47	0.38	0.28
Base-wall				
6,000	-1.40	-1.43	0.11	0.29
9,500	-1.46	-1.49	0.09	0.25
19,000	-1.40	-1.44	0.09	0.19

in good agreement with van Oudheusden et al. (2007), see figure 1.7.

The biggest changes occur in the shear-layer region. The velocity shows an increasing activity in along the side of the cylinder with increasing Reynolds number, with the reversed flow near the cylinder side increasing and moving forward. Starting from $\overline{u}/U$ = -0.10 at x/D = 0.31, -0.18 at x/D = 0.24, to -0.24 at x/D = 0.17, for Re_D = 6,000, 9,500, and 19,000, respectively. The pressure field shows the pressure minimum along the side of the cylinder moving forward with Reynolds number, from x/D = 0.34, 0.24, to 0.19. The corresponding values for the pressure are $\overline{C}_p$ = -1.58, -1.65, and -1.55 for Re_D = 6,000, 9,500, and 19,000, respectively.

To verify the validity of the results, the values for mean and fluctuations of the side- and base-wall pressure obtained from PIV are compared with the values from the pressure transducers. The results are shown in table 8.1. The values for the mean pressure are in good agreement. Except for the side-wall pressure at Re_D = 6,000 (having a difference of just under 6%), differences between PIV and transducers are smaller than 3%. The pressure fluctuations for the side-wall are within 30% of each other. The pressure fluctuations for the wake differ by more than 100%. This large difference is due to the 2D method in a 3D
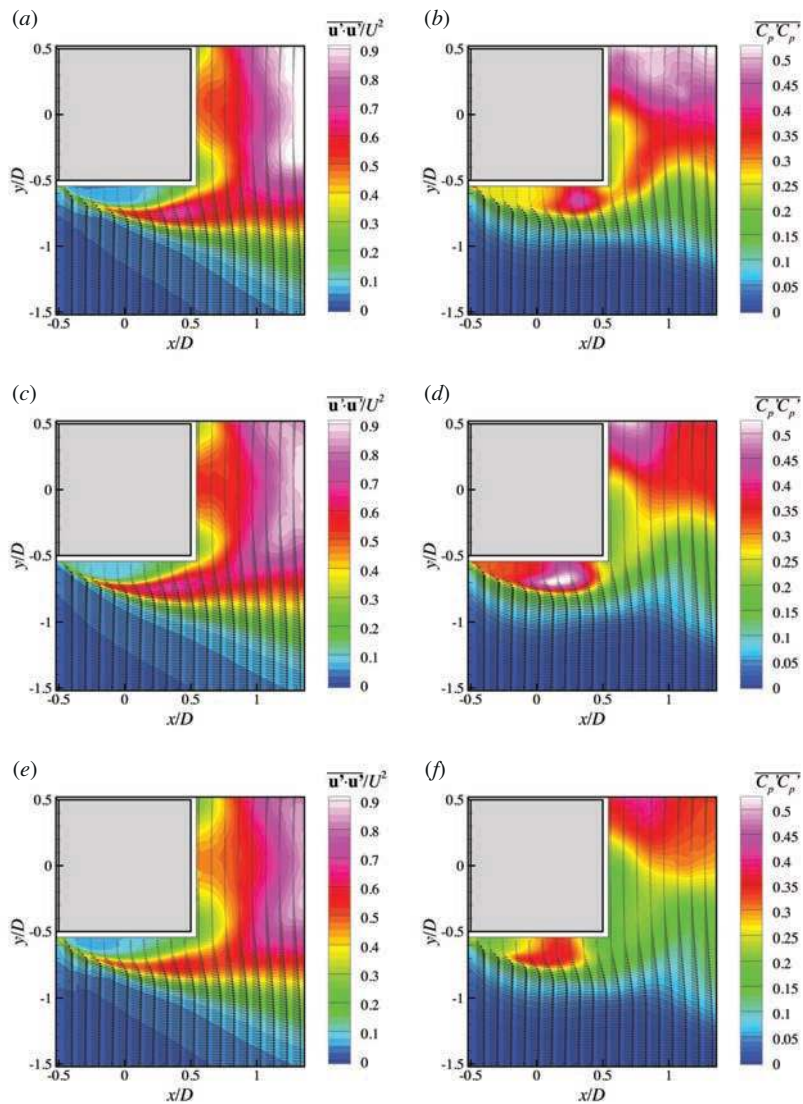
Figure 8.2: Time-averaged velocity and pressure fluctuations. From *top* to *bottom*: $Re_D = 6{,}000$, $9{,}500$, and $19{,}000$. *Left* Velocity fluctuations. *Right* Pressure fluctuations. Each sixth vector in *x*-direction is shown.

flow and due to edge-effects (see chapter 5).

The mean pressure can be used to estimate mean loading. Due to symmetry the mean lift should be zero. The current experiment doesn't allow to check this. However, the symmetry in the wake suggests that the lift is approximately zero for all Reynolds numbers. The mean drag was found to be $\overline{C}_d = 2.14$, 2.15, and 2.13, for $Re_D = 6{,}000$, 9,500, and 19,000, respectively. The contribution of the front face was estimated based on results from experiments on a similar setup (see Turella 2008, for details on the experiment) at $Re_D \approx 9{,}500$, $\overline{C}_d\big|_{front} = 0.74$ (with an RMS of 2.5%), and assuming it Reynolds number independent.

Figure 8.2 show the variance of the velocity and pressure fluctuations. The velocity fluctuations along the side of the cylinder show a decrease with Reynolds number, from $\overline{u'u'} = 0.75$, 0.68, to 0.58, for $Re_D = 6{,}000$, 9,500, and 19,000, respectively. The location, however, does not change significantly ($x/D \approx 0.4$). The velocity fluctuations show that the wake is symmetric around the wake centreline and that, for the region observed, the peak fluctuations decrease with increasing Reynolds number. The maxima in fluctuations within the current field-of-view are $\overline{u'u'} = 0.96$, 0.90, and 0.89, for $Re_D = 6{,}000$, 9,500, and 19,000, respectively.

The peak of the fluctuations along the side of the cylinder also moves forward with Reynolds number, from $x/D = 0.32$, to $x/D = 0.12$ to 0.19, and $x/D = 0.10$ to 0.15. The respective values of fluctuation are $\overline{C_p' C_p'} = 0.43$, 0.53, and $= 0.37$, for $Re_D = 6{,}000$, 9,500, and 19,000, respectively. It is following a similar trend as the mean side-wall region pressure minima, having a peak at $Re_D = 9{,}500$. In the wake the pressure fluctuations are influenced by the lack of full 3D information to determine the instantaneous pressure fields. This shows its footprint in the large asymmetry in the pressure fluctuations in this region. However, the fluctuations seem to follow the same trend with Reynolds number as the velocity fluctuations, decreasing with increasing Reynolds number.

8.2 Phase-averaged description

The extrema in the time-averaged side-lobe pressure and pressure fluctuations cannot be explained purely from the time-averaged velocity

field and its statistics. The flow around bluff-bodies is know to be peri-
odic. To determine periodic loading and to see whether the extrema in
the pressure originate from periodic phenomena and to determine peri-
odic loading, phase-averages were taken. The phase-averages are deter-
mined using the side-wall pressure transducer signal (see figure 6.4) as
a reference. See §2.2.3 and §6.4 for details on the phase determination.

8.2.1   Phase-averaged flow structure

Figure 8.3 shows sequences of phase-averaged vorticity, velocity fluc-
tuations, pressure, and pressure fluctuations for $Re_D = 9{,}500$.

Beginning at $\phi = 0$, the pressure on the side-wall centre of the cylin-
der is at its global minimum, as inferred from the side-wall pressure sig-
nal. The shear-layer appears relatively close to the cylinder, and the size
of the recirculation region is at its global minimum. The side-wall sepa-
ration region may therefore be loosely characterised as being relatively
thin and intense compared to what will be shown at other phases. In ad-
dition, the shear-layer begins to grow significantly from about half-way
along the cylinder. Lyn & Rodi (1994) found that shear-layer growth
for the square cylinder departs markedly from the linear growth of un-
forced mixing layers. As a result, the shear-layer has a brief interaction
with the trailing edge. Passing the trailing edge in streamwise direction,
the vorticity level can be seen to decrease by well over 50%, whereas
the crossflow turbulence intensity increases dramatically. At the trailing
edge, the roll-up of the shear-layer into the main Kármán vortex can be
observed, evident in all the phase-averaged quantities in figure 8.3.

By $\phi = \pi/2$, the pressure at the side-wall is in the middle of its
global increase. The shear-layer has moved appreciably away from the
cylinder, although the vorticity levels have not changed significantly
from $\phi = 0$. The side-wall separation region breaks open, and an addi-
tional influx of fluid near the trailing edge increases the reversed-flow
up to $0.5\,U$. The Kármán vortex appears much farther downstream in
the near-wake region, but is still clearly connected to the shear-layer. It
can be seen that the velocity fluctuations and pressure fluctuations are
moving downstream with increasing phase.

At $\phi = \pi$, the pressure at the side-wall is at its maximum. The
shear-layer is now at its farthest distance from the cylinder in the global
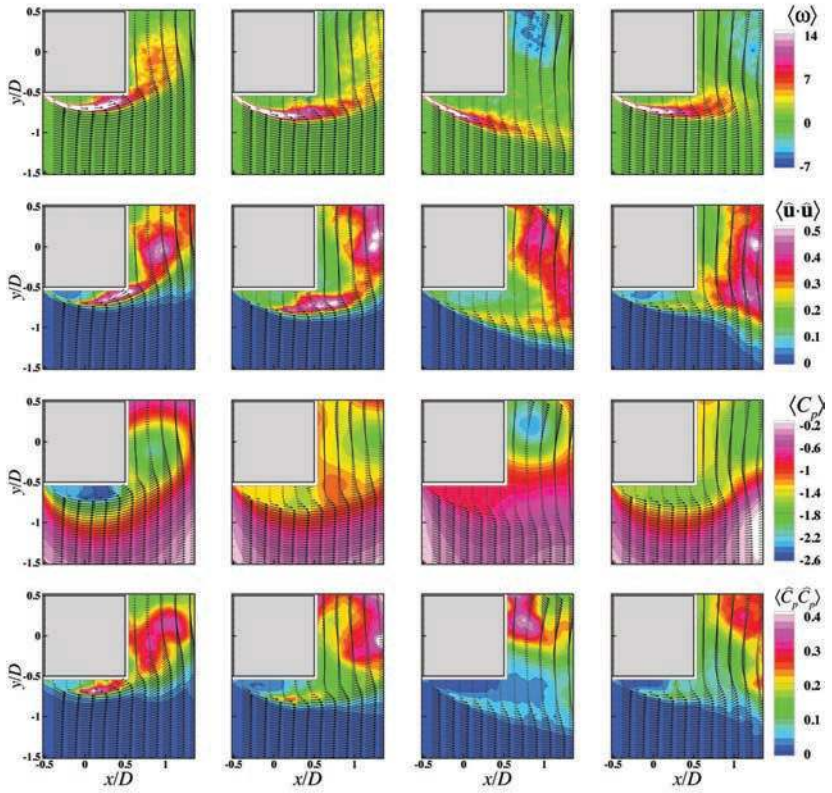
Figure 8.3: Phase-averaged vorticity, velocity fluctuations, pressure, and pressure fluctuations for $Re_D = 9,500$ at four different phases. From *top* to *bottom*: Vorticity, velocity fluctuations, pressure, and pressure fluctuations. From *left* to *right*: $\phi = 0$, $\phi = \pi/2$, $\phi = \pi$, and $\phi = 3\pi/2$. Each tenth vector is shown in *x*-direction and each second vector in *y*-direction.

sense, and the phase-averaged results have changed dramatically. The vorticity level, as well as the velocity and pressure fluctuations, have all decreased significantly along the shear-layer, compared to their values at the previous two phases. The Kármán vortex has now been shed and convected downstream. Closer inspection reveals that the opposite shear-layer Kármán vortex shedding process is now taking place. As a matter of fact, a cursory comparison between phases $\phi = 0$ and $\phi = \pi$ shows that, in the near-wake, they are almost mirror images of each other. The side-wall separation region may now be loosely characterised as relatively large and rather weak, with reversed-flow being much smaller than at $\phi = 0$ and $\phi = \pi/2$, being only 0.05 U.

Finally, by $\phi = 3\pi/2$, the pressure at the side-wall is in the middle of its global decrease. The shear-layer has moved towards the cylinder and is about to form the Kármán vortex of the next shedding cycle. The opposite shear-layer has shed its Kármán vortex, as evidenced by the large negative vorticity region in the near-wake moving out of view. As the shear-layer moves back towards the cylinder, the side-wall separation region begins to close. The reversed-flow magnitude begins to increase again, and the entire process described above is about to repeat itself.

8.2.2   Phase-averaged pressure (periodic loading)

Figure 8.4 shows a 3D visualisation of phase-averaged pressure with streamwise direction, x, crossflow direction, y, and phase ϕ for $Re_D =$ 9,500. The location of the square cylinder is indicated with a square (at $\phi = 0$). It visualises the process described before. Starting from $\phi = 0$, the pressure along the side wall increases reaching a maximum at $\phi = \pi$ and then decreases again to a minimum around $\phi = 2\pi$ ($= 0$). The low pressure region in the wake of the cylinder at $\phi = 0$ indicates that a Kármán vortex is present, which is subsequently shed (from the bottom side) and moving away and into the wake. At $\phi \approx \pi/2$ a low pressure region is starting to form near the top trailing edge of the cylinder. This is a Kármán vortex starting to form from the top side and by $\phi \approx \pi$ it has formed and subsequently moves away and into the wake. At $\phi \approx 3\pi/2$ a low pressure region start to form at the bottom trailing edge, which is the start of the Kármán vortex present at $\phi = 0$ ($= 2\pi$).
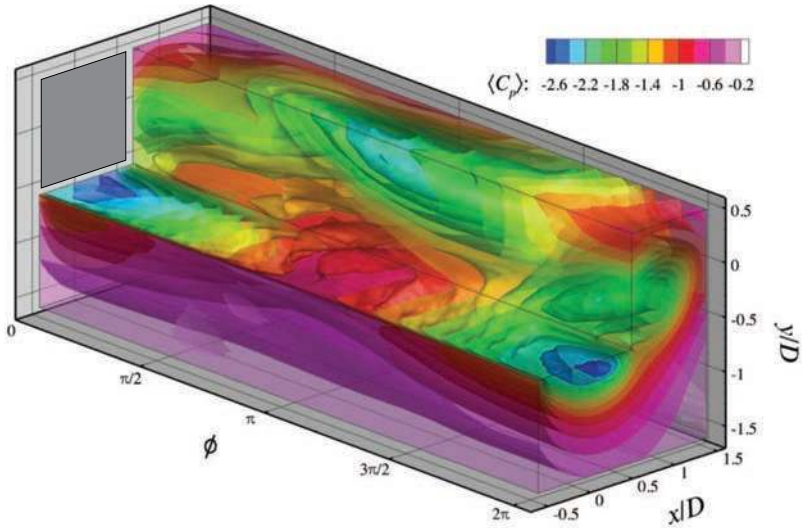
Figure 8.4: Volume visualisation of phase-averaged pressure with x, y, and phase. $Re_D = 9{,}500$.

To show what the cylinder experiences, phase-averaged pressure in the planes closest to the cylinder (x-ϕ and y-ϕ planes) were taken to represent the phase-averaged side- and base-wall pressure distributions.

The evolution of phase-averaged pressure and the evolution of the pressure fluctuations around the phase averages for the side-wall are shown in figure 8.5 for each Reynolds number. For clarity one and a half cycle is shown. For all Reynolds numbers, the oscillating nature of the side-wall pressure is visible and is present along the whole side. However, the values attained differ significantly. The side-wall pressure shows that the maxima attained are similar for all Reynolds number, but the minima are different. The side-wall pressure minima were found for $\phi \approx 0$, $\langle C_p \rangle = $ -2.39 at $x/D = 0.27$, -2.60 at $x/D = 0.17$, and -2.39 at $x/D = 0.15$. This shows a similar trend with Reynolds number as the changes in the side-lobe pressure minimum and pressure fluctuations in the time-averaged description. The minima move forward with increasing Reynolds number and have a peak value for $Re_D = 9{,}500$. The

minima in phase-averaged pressure coincide with the (local) maxima
in pressure fluctuations around the phase-average, which were found
to be $\langle \widehat{C}_p \widehat{C}_p \rangle = 0.40$ at $x/D = 0.27$, 0.22 at $x/D = 0.15$, and 0.23 at
$x/D = 0.14$.

The evolution with phase of phase-averaged pressure and evolution
of pressure fluctuations around the phase-averages for the base-wall are
shown in figure 8.5. Little change with Reynolds number can be ob-
served for the phase-averaged pressure, $\langle C_p \rangle$. For all Reynolds num-
bers, it shows alternating high and low pressure regions near the bot-
tom and top side of the cylinder. These alternating regions occur in
anti-phase for the top and bottom edge, respectively, i.e. when there
is high pressure at the top trailing edge the bottom trailing edge has
low pressure. The low pressure regions start near the edges and move
towards the centre of the base with phase before disappearing. They
are related with the formation and convection of Kármán vortices. In
between these low pressure regions there are regions of relatively high
pressure. The pressure fluctuations around the phase-average show sim-
ilar evolution with phase for all Reynolds number. The major differ-
ence between the Reynolds numbers is the intensity of the fluctuations,
which decreases with increasing Reynolds number. Even though the
determination of pressure from stereo-PIV in the wake is hampered by
the lack of 3D information the fluctuations show reasonable symmetry
behaviour with phase, both in mean and fluctuations.

To assure the pressure trends (in phase and with *Re*) at the side is
correctly captured, phase-averaged pressure and pressure fluctuations
from transducer and from PIV are compared with one another in figures
8.6(*a-d*) and 8.7(*a-d*)

The phase-averaged pressure for the side-wall shows for both trans-
ducer and PIV the same behaviour, figure 8.6(*a*, *b*). The maximum
pressure is the lowest for $Re_D = 19,000$ and the minimum is the lowest
for $Re_D = 9{,}500$. However, the absolute value differ. The minima were
found to be within 7% (with respect to their respective value) comparing
transducer with PIV, whereas the maxima are within 33% (with respect
to their respective value). The fluctuations around the phase-average
are in good agreement between the transducer and PIV, see figure 8.6(*c*,
d). Despite these differences, the influence of the Reynolds number and
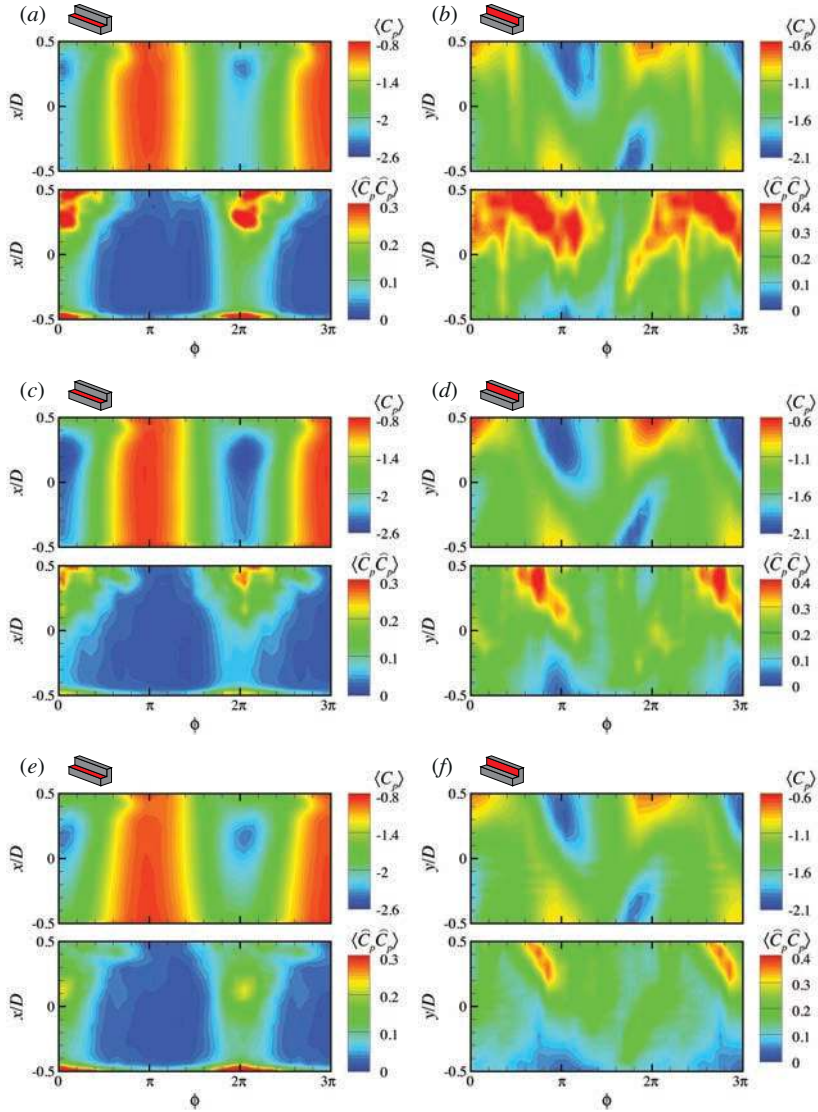the evolution in phase are correctly captured.

Figure 8.5: Phase-averaged pressure and pressure fluctuations with phase. *Left*: side-wall. *Right*: base-wall. (*a-b*) $Re_D = 6,000$, (*c-d*) $Re_D = 9,500$, (*e-f*) $Re_D = 19,000$. *Top*: phase-averaged pressure. *Bottom*: pressure fluctuations.
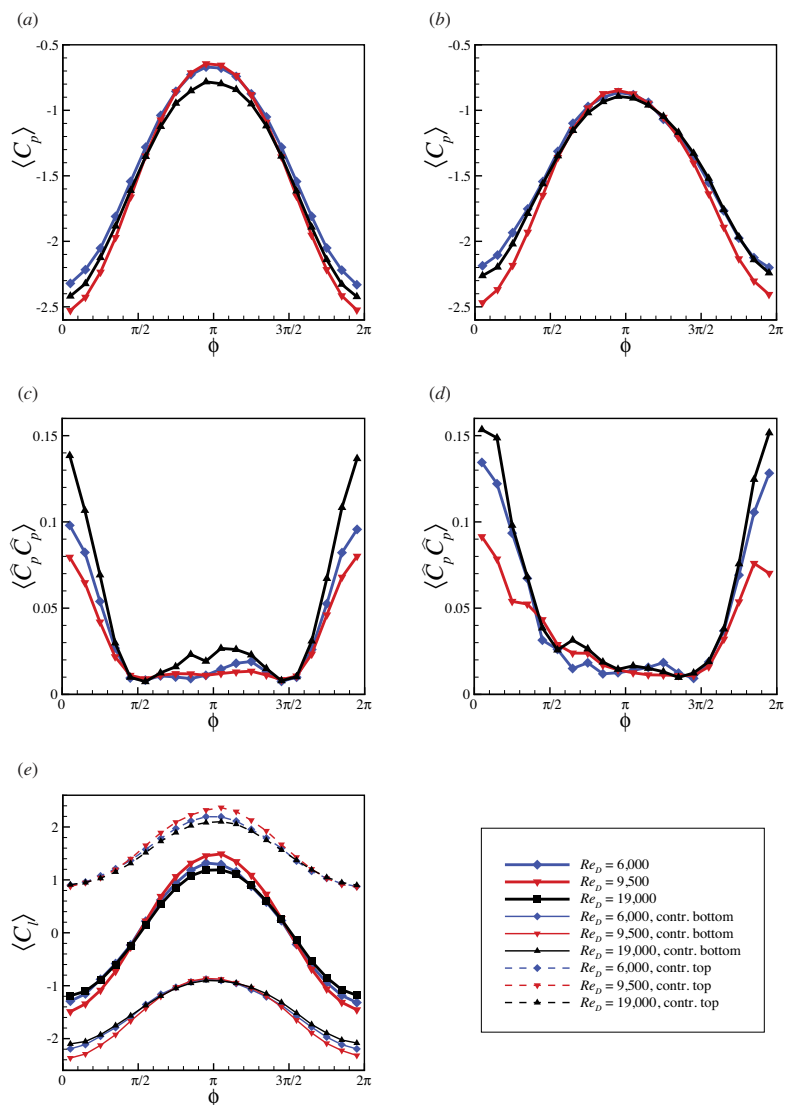
Figure 8.6: Phase-averaged side pressure and pressure fluctuations. (*a-d*) Phase-averaged pressure and pressure fluctuations for the side-wall sensor location (*a*) Pressure from transducer, (*b*) Pressure from PIV, (*c*) Pressure fluctuations from transducer, (*d*) Pressure fluctuations from PIV. (*e*) Estimated lift.

The phase-averaged pressure for the base-wall shows for both transducer and PIV similar behaviour, figure 8.7(*a*, *b*). Differences are larger than for the side-wall. This is expected, since the wake is 3D and stereo does not capture all necessary information to determine the pressure. However, the phase-averaged pressure signal is in good agreement. The fluctuations around the phase-average are in fair agreement between the transducer and PIV, see figure 8.7(*c*, *d*). Despite these differences, the influence of the Reynolds number and the evolution in phase for the phase-averaged pressure are correctly captured.

Periodic loading

After determining the side- and base-wall pressure distributions (and verifying their validity), they can be used to estimate the phase-averaged loading. Integrating the pressure along *x* or *y* for each phase, the contribution of the side- or base-wall to the force acting on the cylinder can be determined, see figure 8.6(*e*) and 8.7(*e*).

To estimate the total periodic lift, the contribution of the top side is estimated by shifting the bottom side contribution by half a cycle in phase. Figure 8.6(*e*) shows the contributions of the bottom and top side to the periodic lift force, together with the estimation for the total lift force. The lift has an amplitude value of $\langle C_l \rangle_{max} = 1.32$, 1.49, and 1.19, for $Re_D = 6{,}000$, 9,500, and 19,000, respectively. The amplitude for $Re_D = 9{,}500$ is 13% larger than the amplitude for $Re_D = 6{,}000$ and 25% larger than $Re_D = 19{,}000$.

To estimate the total periodic drag, the contribution of the front was based on results from experiments on a similar setup (see Turella 2008, for details on the experiment) at $Re_D \approx 9{,}500$, $\langle C_d \rangle|_{front} = 0.74$ (with an RMS of 2.5%), and assuming it to be constant and Reynolds number independent. Figure 8.7(*e*) shows the contributions of the front and base to the periodic drag force, together with the drag force. The drag fluctuations are $\langle C_d \rangle_{RMS} = 0.14$, 0.13, and 0.10, for $Re_D = 6{,}000$, 9,500, and 19,000, respectively. It should be noted, however, that the pressure determination in the wake is limited by both 3D aspects of the flow and edge effects near the top of the domain.
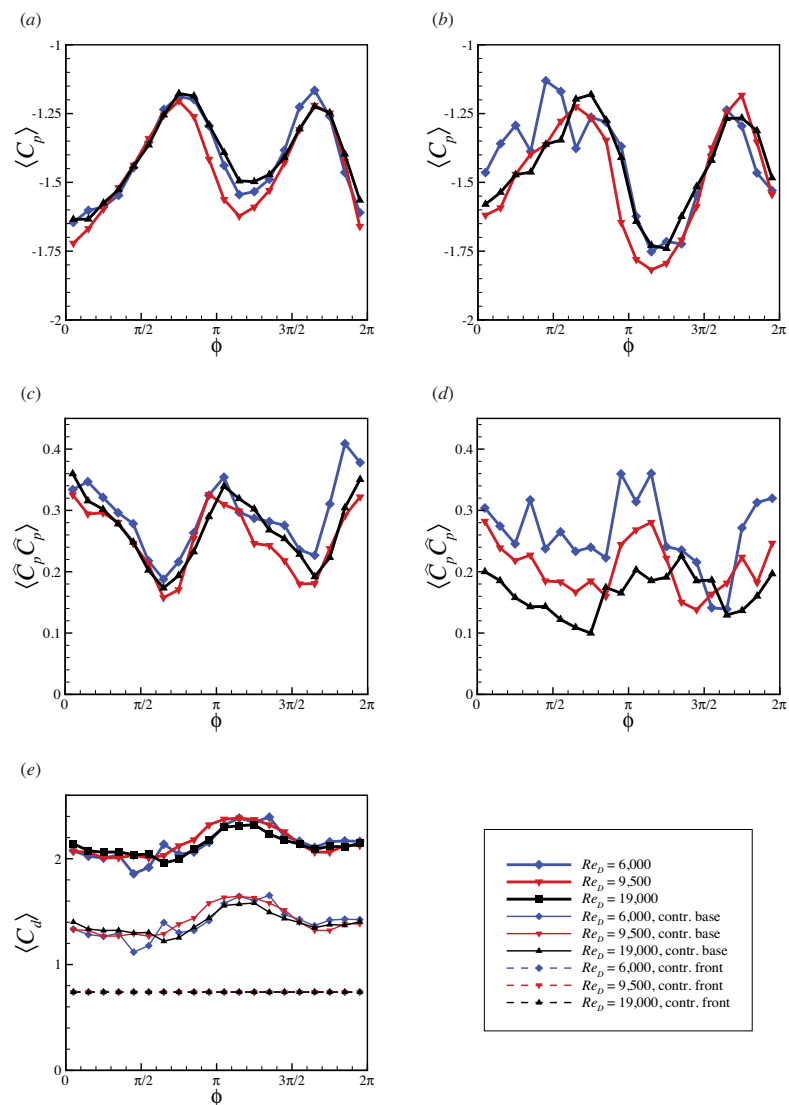
Figure 8.7: Phase-averaged base pressure and pressure fluctuations. (*a-d*) Phase-averaged pressure and pressure fluctuations for the base-wall sensor location. (*a*) Pressure from transducer, (*b*) Pressure from PIV, (*c*) Pressure fluctuations from transducer, (*d*) Pressure fluctuations from PIV. (*e*) Estimated drag.

8.3 Instantaneous pressure

To get insight into what flow structures cause the surface pressure fluctuations and periodic loading to change with Reynolds number, figure 8.8 shows instantaneous fields of vorticity, ω_z, and corresponding pressure for the three different Reynolds numbers. The instantaneous snapshots were chosen to be representative of the moment in phase, where the Reynolds number influence is the largest ($\phi \approx 0$).

The vorticity fields, figure 8.8(a, c, and e), reveal the shear-layer instability starting more upstream with increasing Reynolds number. At $Re_D = 6{,}000$, the shear-layer starts shedding distinct separate vortices roughly at the trailing edge. For $Re_D = 9{,}500$, the shear-layer starts shedding distinct separate vortices roughly halfway along the cylinder. Finally, at $Re_D = 19{,}000$, the shear-layer starts shedding distinct separate vortices at roughly one quarter downstream of the leading edge. Subsequently, these shed vortices interact and form a Kármán-like vortex in the wake. The vortices that comprise this Kármán-like vortex seem to get smaller and less intense with increasing Reynolds number. However, the intensity might be attenuated by the limited resolution of the experiment.

The pressure fields, figure 8.8(b, d, and f), show two low pressure regions. One along the side of the cylinder coinciding with the side-wall separation region and one in the wake coinciding with the Kármán-like vortex. The location of the Kármán-like vortex seems to change slightly with Reynolds number, having roughly the same location for $Re_D = 6{,}000$ and $19{,}000$, whereas at $Re_D = 9{,}500$ it is located more inwards toward the centreline of the wake. Local regions of low pressure coincide with vortices, most noticeable along the side of the cylinder for $Re_D = 9{,}500$.

Combined with the time- and phase-averaged results, these results suggest that the vortices formed by the shear-layer instability significantly influence the side-wall pressure and the periodic loading on a square cylinder.
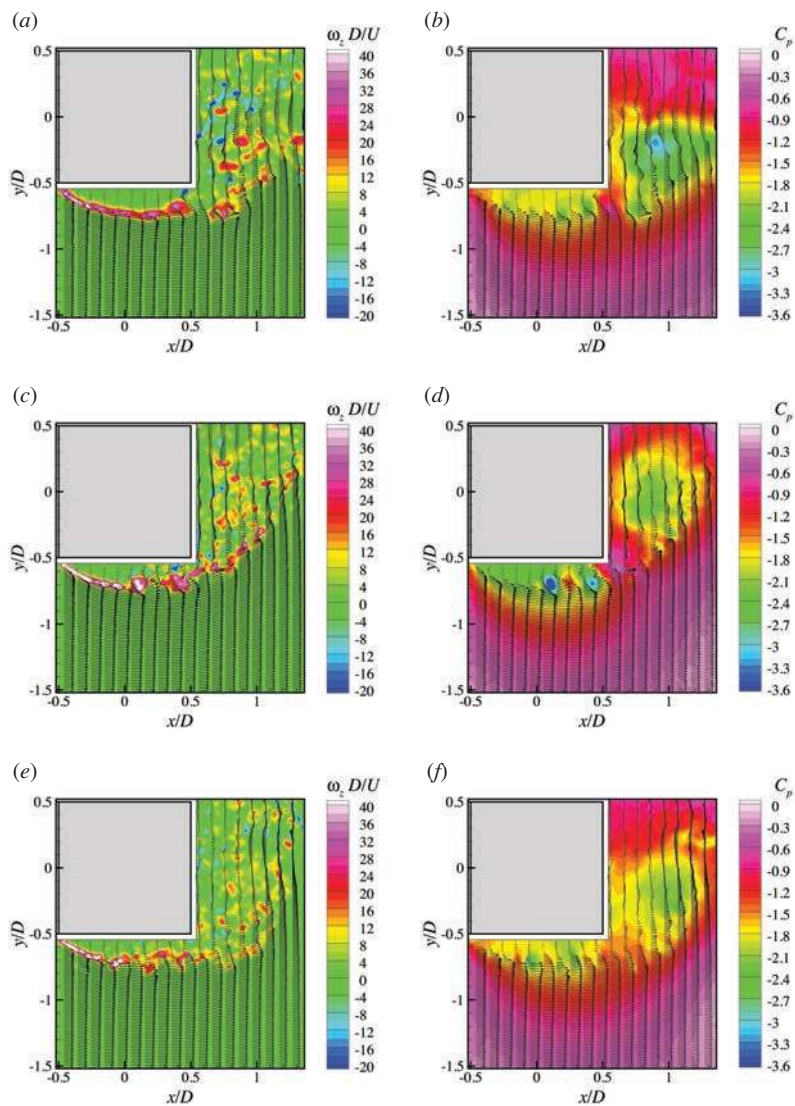
Figure 8.8: Instantaneous vorticity and pressure fields. Each snapshot is representative for $\phi = 0$. (*a*, *c*, and *e*) Instantaneous vorticity. (*b*, *d*, and *f*) Instantaneous pressure. (*a-b*) $Re_D = 6,000$. (*c-d*) $Re_D = 9,500$. (*e-f*) $Re_D = 19,000$. Each sixth vector in *x*-direction is shown.

Chapter 9

Conclusions

The operating principle of obtaining pressure from PIV-data was described using either a Eulerian or a Lagrangian approach. Based on the current implementation, theoretical considerations led to estimates of the limitations of the method. These estimates were checked using a performance analysis on a synthetic flow field, comprised of a advecting Gaussian vortex, as well as on an experimental test-case, the flow around a square cylinder. All results indicate that in order to perform successful pressure-PIV the following criteria should be met.

The spatial resolution needed to successfully perform pressure-PIV were found to be the same for both the Eulerian and the Lagrangian approaches. Ideally (defined as peak modulation smaller than 5%) the spatial resolution needs to be ten times than that corresponding to the flow structures, i.e. $WS/\lambda_x < 0.1$. Good results (based on peak modulation smaller than 10%) have been found for spatial resolutions five times higher than the resolution corresponding to the flow structures, i.e. $WS/\lambda_x < 0.2$.

The temporal resolution needed to successfully perform pressure-PIV is related to the approach used. However, both approaches have a similar limitation. The temporal resolution (acquisition frequency) needs to be ten times that of the corresponding flow frequency, $f_{acq} > 10 \times f_{flow}$. For the Eulerian approach f_{flow} is related to the Eulerian time scales. For the Lagrangian approach f_{flow} is related to the Lagrangian time scales. Depending on the problem at hand one method

might be more suitable than the other. For the current flow problem, where the advective influences are small compared to the strength of the vortices, the restrictions on the Lagrangian approach were found to be more limiting than the restrictions on the Eulerian approach.

Addition of the third component is necessary in order to successfully obtain the pressure from the velocity field in 3D flow. This is clearly shown by the correlation between the pressure-PIV results and the pressure transducer signal as well as the findings in chapter 5, where a peak response with a $\cos(\alpha)$ behaviour with the angle of the vortex axis with the measurement plane normal was found. However, the large scale structures in the wake, i.e. the Kármán vortices, are predominantly 2D (with the axis normal to the current measurement plane) and their influence is therefore already captured correctly by the planar description, as evidenced by the strong correlation (0.65) between the pressure signal from stereo-PIV and pressure transducer signal at the base-wall.

The influence of measurement noise could not be observed in the current analysis of the experimental results. However, estimating U_a and V_p to be in the order of the freestream velocity, U ($\approx 2\ WS/\Delta t$), then, based on the analysis in chapter 5 and $\varepsilon_u/U = 1.5\%$, the effect of noise is expected to be lower than 2%, which is well below the differences found due to the spatial and temporal resolution.

The description of the pressure field around and loading on a square cylinder showed that the vortices, emanating from the shear-layer instability change the flow around the cylinder significantly. Pressure loading and pressure fluctuations along the side of the cylinder can increase depending on Reynolds number. An increase in amplitude of estimated periodic lift for $Re_D = 9,500$ compared with $Re_D = 6,000$ and $19,000$ of $> 10\%$ was found. Together with the slight change in location of the Kármán-like vortex in the wake this suggest an intimate (and complex) relationship exists between the side-wall pressure, shear-layer, separation region, and near-wake, which changes significantly with Reynolds number.

Acknowledgements

Bibliography

Adrian, R. J. (1997), 'Dynamic ranges of velocity and spatial resolution of particle image velocimetry', *Meas. Sci. Technol.* **8**, 1393–1398.

Adrian, R. J. (2005), 'Twenty years of particle image velocimetry', *Exp. Fluids* **39**(2), 159–169.

Anderson, J. D. (1991), *Fundamentals of Aerodynamics*, Aerospace Science Series, second edn, McGraw-Hill International editions.

Baur, T. & Köngeter, J. (1999), 'PIV with high temporal resolution for the determination of local pressure reductions from coherent turbulence phenomena', *3rd International Workshop on Particle Image Velocimetry, Santa Barbara, 16-18 September* pp. 1–6.

Benedict, L. & Gould, R. (1996), 'Towards better uncertainty estimates for turbulence statistics', *Exp. Fluids* **22**(2), 129–136.

Birch, J. & Dickinson, M. (2003), 'The influence of wing-wake interactions on the production of aerodynamic forces in flapping flight', *J. Exp. Biol.* **206**(13), 2257.

Birch, J., Dickson, W. & Dickinson, M. (2004), 'Force production and flow structure of the leading edge vortex on flapping wings at high and low Reynolds numbers', *J. Exp. Biol.* **207**(7), 1063–1072.

Charonko, J., King, C. V., Smith, B. L. & Vlachos, P. P. (2010), 'Assessment of pressure field calculations from particle image velocimetry measurements', *Meas. Sci. Technol.* **21**, 1–16.

Christensen, K. & Adrian, R. J. (2002), 'Measurement of instantaneous Eulerian acceleration fields by particle image accelerometry: method and accuracy', *Exp. Fluids* **33**(6), 759–769.

David, L., Jardin, T. & Farcy, A. (2009), 'On the non-intrusive evaluation of fluid forces with the momentum equation approach', *Meas. Sci. Technol.* **20**, 1–11.

de Clercq, K. M. E., de Kat, R., Remes, B., van Oudheusden, B. W. & Bijl, H. (2009), Flow visualization and force measurements on a hovering flapping-wing MAV 'DelFly II', *in* '39th AIAA Fluid Dynamics Conference', San Antonio, Texas.

de Kat, R. (2007), Vortex decay behind a generic wing-flap-jet aircraft model, Master's thesis, Aerospace Engineering, Delft University of Technology.

de Kat, R., Humble, R. A. & van Oudheusden, B. W. (2010), Time-resolved PIV study of a transitional shear-layer around a square cylinder, *in* 'Proceedings of the IUTAM Symposium on Bluff-Body wakes and Vortex Induced Vibrations', Capri, Italy.

de Kat, R. & van Oudheusden, B. W. (2011), 'Instantaneous planar pressure determination from piv in turbulent flow', *Exp. Fluids* (online first).

de Kat, R., van Oudheusden, B. W. & Scarano, F. (2008), 'Instantaneous planar pressure field determination around a square-section cylinder based on time-resolved stereo-PIV', *14th International Symposium on Applications of Laser Techniques to Fluid Mechanics, Lisbon, Portugal, 7-10 July* pp. 1–11.

de Kat, R., van Oudheusden, B. W. & Scarano, F. (2009*a*), Instantaneous Pressure Field Determination around a Square-Section Cylinder using Time-Resolved Stereo-PIV, *in* '39th AIAA Fluid Dynamics Conference', San Antonio, Texas.

de Kat, R., van Oudheusden, B. W. & Scarano, F. (2009*b*), Instantaneous Pressure Field Determination in a 3D Flow using Time-Resolved Thin Volume Tomographic-PIV, *in* '8th International Sym-

posium on Particle Image Velocimetry', Melbourne, Australia, pp. 1–4.

Durao, D., Heitor, M. V. & Pereira, J. (1988), 'Measurements of turbulent and periodic flows around a square cross-section cylinder', *Exp. Fluids* **6**(5), 298–304.

Elsinga, G. E., Scarano, F., Wieneke, B. & van Oudheusden, B. W. (2006), 'Tomographic particle image velocimetry', *Exp. Fluids* **41**(6), 933–947.

Farhadi, M. & Rahnama, M. (2005), 'Three-dimensional study of separated flow over a square cylinder by large eddy simulation', *P. I. Mech. Eng. G-J. Aer.* **219**(3), 225–234.

Foucaut, J., Carlier, J. & Stanislas, M. (2004), 'PIV optimization for the study of turbulent flow using spectral analysis', *Meas. Sci. Technol.* **15**, 1046–1058.

Foucaut, J. & Stanislas, M. (2002), 'Some considerations on the accuracy and frequency response of some derivative filters applied to particle image velocimetry vector fields', *Meas. Sci. Technol.* **13**(7), 1058–1071.

Fujisawa, N., Nakamura, Y., Matsuura, F. & Sato, Y. (2006), 'Pressure field evaluation in microchannel junction flows through PIV measurement', *Microfluid. Nanofluid.* **2**(5), 447–453.

Fujisawa, N., Tanahashi, S. & Srinivas, K. (2005), 'Evaluation of pressure field and fluid forces', *Meas. Sci. Technol.* **16**, 989–996.

Gurka, R., Liberzon, A., Hefetz, D., Rubinstein, D. & Shavit, U. (1999), 'Computation of Pressure Distribution Using PIV Velocity Data', *3rd International Workshop on Particle Image Velocimetry, Santa Barbara, 16-18 September* pp. 1–6.

Haigermoser, C. (2009), 'Application of an acoustic analogy to PIV data from rectangular cavity flows', *Exp. Fluids* **47**(1), 145–157.

Hain, R. & Kähler, C. J. (2007), 'Fundamentals of multiframe particle image velocimetry (piv)', *Exp. Fluids* **42**, 575–587.

Herman, G. T. & Lent, A. (1976), 'Iterative Reconstruction Algorithms', *Comput. Biol. Med.* **6**, 273–294.

Hosokawa, S., Moriyama, S., Tomiyama, A. & Takada, N. (2003), 'PIV Measurement of Pressure Distributions about Single Bubbles', *J. Nucl. Sci. Technol.* **40**(10), 754–762.

Huang, N., Shen, Z., Long, S., Wu, M., Shih, H., Zheng, Q., Yen, N., Tung, C. & Liu, H. (1998), 'The empirical mode decomposition and the Hilbert spectrum for nonlinear and non-stationary time series analysis', *P. Roy. Soc. Lond. A Mat.* **454**(1971), 903–995.

Huang, N., Wu, M., Qu, W., Long, S., Shen, S. & Zhang, J. (2003), 'Applications of Hilbert-Huang transform to non-stationary financial time series analysis', *Appl. Stoch. Model. Bus.* **19**(3), 245–268.

Humble, R. A. (2008), Unsteady Flow Organization of a Shock Wave/Boundary Layer Interaction, PhD thesis, Delft University of Technology.

Hussain, A. K. M. F. & Reynolds, W. (1970), 'The mechanics of an organized wave in turbulent shear flow', *J. Fluid Mech.* **41**(part 2), 241–258.

Jakobsen, M., Dewhirst, T. & Greated, C. (1997), 'Particle image velocimetry for predictions of acceleration fields and force within fluid flows', *Meas. Sci. Technol.* **8**, 1502–1516.

Kline, S. J. & McClintock, F. A. (1953), 'Describing uncertainties in single- sample experiments', *Mechanical Engineering* **75**, 3–8.

Koschatzky, V., Moore, P., Westerweel, J., Scarano, F. & Boersma, B. (2011), 'High speed PIV applied to aerodynamic noise investigation', *Exp. Fluids* **4**, 863–876.

Kurtulus, D. F., Scarano, F. & David, L. (2007), 'Unsteady aerodynamic forces estimation on a square cylinder by TR-PIV', *Exp. Fluids* **42**(2), 185–196.

Lighthill, J. (1986), 'Fundamentals concerning wave loading on offshore structures', *J. Fluid Mech.* **173**, 667–681.

Lin, J. & Rockwell, D. (1996), 'Force identification by vorticity fields: techniques based on flow imaging', *J. Fluid. Struct.* **10**(6), 663–668.

Liu, X. & Katz, J. (2006), 'Instantaneous pressure and material acceleration measurements using a four-exposure PIV system', *Exp. Fluids* **41**(2), 227–240.

Luo, S., Tong, X. & Khoo, B. (2007), 'Transition phenomena in the wake of a square cylinder', *J. Fluid. Struct.* **23**(2), 227–248.

Lyn, D., Einav, S., Rodi, W. & Park, J. (1995), 'A laser-Doppler velocimetry study of ensemble-averaged characteristics of the turbulent near wake of a square cylinder', *J. Fluid Mech.* **304**(12), 285–319.

Lyn, D. & Rodi, W. (1994), 'The flapping shear layer formed by flow separation from the forward corner of a square cylinder', *J. Fluid Mech.* **267**, 353–376.

Melling, A. (1997), 'Tracer particles and seeding for particle image velocimetry', *Meas. Sci. Technol.* **8**, 1406–1416.

Noca, F., Shiels, D. & Jeon, D. (1997), 'Measuring instantaneous fluid dynamic forces on bodies, using only velocity fields and their derivatives', *J. Fluid. Struct.* **11**(3), 345–350.

Noca, F., Shiels, D. & Jeon, D. (1999), 'A comparison of methods for evaluating time-dependent fluid dynamic forces on bodies, using only velocity fields and their derivatives', *J. Fluid. Struct.* **13**(5), 551–578.

Okajima, A. (1982), 'Strouhal numbers of rectangular cylinders', *J. Fluid Mech.* **123**, 379–398.

Prasad, A. K. (2000), 'Stereoscopic particle image velocimetry', *Exp. Fluids* **29**, 103–116.

Price, J. F. (2006), 'Lagrangian and Eulerian Representations of Fluid Flow: Kinematics and the Equations of Motion', *MIT Open Course Ware* pp. 1–91.

Raffel, M., Willert, C. E., Werely, S. T. & Kompenhans, J. (2007), *Particle Image Velocimetry: A Practical Guide*, second edn, Springer-Verlag Heidelberg Berlin.

Ragni, D., Ashok, A., van Oudheusden, B. W. & Scarano, F. (2009), 'Surface pressure and aerodynamic loads determination of a transonic airfoil based on particle image velocimetry', *Meas. Sci. Technol.* **20**, 074005.

Ragni, D., Schrijer, F. F. J., van Oudheusden, B. W. & Scarano, F. (2010), 'Particle tracer response across shocks measured by piv', *Exp. Fluids* **50**, 53–64.

Scarano, F. & Riethmuller, M. (2000), 'Advances in iterative multigrid PIV image processing', *Exp. Fluids* **29**, 51–60.

Schrijer, F. F. J. & Scarano, F. (2008), 'Effect of predictor–corrector filtering on the stability and spatial resolution of iterative PIV interrogation', *Exp. Fluids* **45**(5), 927–941.

Schröder, A., Geisler, R., Elsinga, G. E., Scarano, F. & Dierksheide, U. (2008), 'Investigation of a turbulent spot and a tripped turbulent boundary layer flow using time-resolved tomographic PIV', *Exp. Fluids* **44**(2), 305–316.

Sheard, G. J., Fitzgerald, M. J. & Ryan, K. (2009), 'Cylinders with square cross-section: wake instabilities with incidence angle variation', *J. Fluid Mech.* **630**, 43–69.

Soloff, S., Adrian, R. & Liu, Z. (1997), 'Distortion compensation for generalized stereoscopic particle image velocimetry', *Meas. Sci. Technol.* **8**(12), 1441–1454.

Stern, F., Muste, M., Beninati, M.-L. & Eichinger, W. E. (1999), 'Summary of Experimental Uncertainty Assessment Methodology with Example', *Iowa Institute of Hydraulic Research Tecnical Report No 406* pp. 1–41.

Turella, A. (2008), 'An Accuracy Assessment of Instantaneous Planar Pressure Imaging based on TR-PIV', *M.Sc. Thesis* pp. 1–114.

Unal, M., Lin, J. & Rockwell, D. (1997), 'Force prediction by PIV imaging: a momentum-based approach', *J. Fluid. Struct.* **11**(8), 965–971.

van Oudheusden, B. W. (2008), 'Principles and application of velocimetry-based planar pressure imaging in compressible flows with shocks', *Exp. Fluids* **45**(4), 657–674.

van Oudheusden, B. W., Casimiri, E. W. F. & Scarano, F. (2008), 'Aerodynamic load characterisation of a low speed aerofoil using particle image velocimetry', *Aeronaut. J.* **112**(1130), 197.

van Oudheusden, B. W., Scarano, F. & Casimiri, E. W. F. (2006), 'Non-intrusive load characterization of an airfoil using PIV', *Exp. Fluids* **40**(6), 988–992.

van Oudheusden, B. W., Scarano, F., Roosenboom, E. W. M., Casimiri, E. W. F. & Souverein, L. J. (2007), 'Evaluation of integral forces and pressure fields from planar velocimetry data for incompressible and compressible flows', *Exp. Fluids* **43**(2), 153–162.

van Oudheusden, B. W., Scarano, F., van Hinsberg, N. P. & Watt, D. (2005), 'Phase-resolved characterization of vortex shedding in the near wake of a square-section cylinder at incidence', *Exp. Fluids* **39**(1), 86–98.

Violato, D., Moore, P. & Scarano, F. (2011), 'Lagrangian and Eulerian pressure field evaluation of rod-airfoil flow from time-resolved tomographic PIV', *Exp. Fluids* **4**, 1057–1070.

Westerweel, J. (1997), 'Fundamentals of digital particle image velocimetry', *Meas. Sci. Technol.* **8**, 1379–1392.

Westerweel, J. & Scarano, F. (2005), 'Universal outlier detection for PIV data', *Exp. Fluids* **39**(6), 1096–1100.

White, F. M. (1991), *Viscous Fluid Flow*, Mechanical Engineering Series, second edn, McGraw-Hill International editions.

Wieneke, B. (2005), 'Stereo-PIV using self-calibration on particle images', *Exp. Fluids* **39**(2), 267–280.

Wieneke, B. (2008), 'Volume self-calibration for 3D particle image velocimetry', *Exp. Fluids* **45**(4), 549–556.

Willert, C. (1997), 'Stereoscopic digital particle image velocimetry for application in wind tunnel flows', *Meas. Sci. Technol.* **8**, 1465–1469.

Williamson, C. H. K. (1996), 'Vortex dynamics in the cylinder wake', *Annu. Rev. Fluid Mech.* **28**(1), 477–539.

List of publications

Journal articles

- de Kat, R., Humble, R. A. and van Oudheusden, B. W. (in preparation), 'Influence of shear-layer instability on pressure loading of a square cylinder.'

- Nati, A., de Kat, R., Scarano, F. and van Oudheusden, B. W. (in preparation), 'Dynamic pitching effect on a laminar separation bubble.'

- de Kat, R. and van Oudheusden, B. W. (2011), 'Instantaneous planar pressure determination from PIV in turbulent flow,' *Exp. Fluids*, DOI:10.1007/s00348-011-1237-5.

- De Clercq, K. M. E., de Kat, R., Remes, B., van Oudheusden, B. W. and Bijl, H. (2009), 'Aerodynamic experiments on Delfly II: Unsteady lift enhancement,' *Int. J. Micro Air Vehicles*, 1(4), 255-262.

- Lentink, D., Muller, U. K., Stamhuis, E. J., de Kat, R., van Gestel, W., Veldhuis, L. L. M., Henningston, P, Hedenstrom, A., Videler, J. J. and van Leeuwen, J. L. (2007), 'How swifts control their glide performance with morphing wings,' *Nature*, 446 (7139), 1082-1085.

Reports

- de Kat, R. (2007), 'Vortex decay behind a generic wing-flap-jet aircraft model,' M.Sc. thesis, Aerodynamics, Aerospace Engineering, Delft University of Technology.

- Veldhuis, L. L. M., de Kat, R. and Elsinga, G. E. (2006), 'Towing tank experiments of cold jet-vortex interaction on a generic wing-flap model,' EU FP6, FAR-Wake TR 2.1.1-5, ASTA4-CT-2005-012238.

Conference publications/contributions

- Lentink, D. and de Kat, R. (2011) 'Swifts have an edge on drag reduction,' SICB Annual Meeting 2011, Salt Lake City, Utah, 3-7 January.

- de Kat, R. and van Oudheusden, B. W. (2010) 'Instantaneous planar pressure from PIV: analytic and experimental test-cases,' 15th Int. Symp. on Application of Laser Techniques to Fluid Mechanics, Lisbon, Portugal, 5-8 July.

- de Kat, R., Humble, R. A. and van Oudheusden, B. W. (2010) 'Time-resolved PIV study of a transitional shear-layer around a square cylinder,' IUTAM Symposium on Bluff Body Wakes and Vortex Induced Vibrations (BBVIV6), Capri Island, Italy, 22-25 June.

- Lentink, D., Muller, U. K., Stamhuis, E. J., de Kat, R., van Gestel, W., Veldhuis, L. L. M., Henningston, P., Hedenstrom, A., Videler, J. J. and van Leeuwen, J. L. (2009) 'How swifts control their glide performance with morphing wings,' Annual Meeting Dutch Biophysics and Biomedical Technology, Nijmegen, The Netherlands, November.

- Veldhuis, L. L. M. and de Kat, R. (2009) 'Vortex wake investigation behind a wing-flap model with jet simulation,' CEAS European Air and Space Conference 2009, Manchester, United Kingdom, 26-29 October.

- de Kat, R., van Oudheusden, B. W. and Scarano, F. (2009) 'Instantaneous pressure field determination in a 3D flow using time-resolved thin volume tomographic-PIV,' 8th Int. Symp. on Particle Image Velocimetry (PIV09), Melbourne, Australia, 25-28 August.

- Lentink, D., Muller, U. K., Stamhuis, E. J., de Kat, R., van Gestel, W., Veldhuis, L. L. M., Henningston, P., Hedenstrom, A., Videler, J. J. and van Leeuwen, J. L. (2009) 'How swifts control their glide performance with morphing wings,' US-Chia Workshop on: Bio-inspired Smart Systems: Materials, Mechanics, Control, and Sensor Innovation, Dalian, China, 2-7 July.

- de Kat, R. and Saunders-Smits, G. N. (2009) '3, 2, 1, Launch!' SEFI Annual Conference 2009: Attracting Young People in Engineering, Rotterdam, The Netherlands, 1-4 July.

- De Clercq, K. M. E., de Kat, R., Remes, B., van Oudheusden, B. W. and Bijl, H. (2009) 'Flow visualization and force measurements on a hovering flapping-wing MAV Delfly II,' AIAA-209-4035, 39th AIAA Fluid Dynamics Conference, San Antonio, Texas, 22-25 June.

- de Kat, R., van Oudheusden, B. W. and Scarano, F. (2009) 'Instantaneous pressure field determination around a square-section cylinder using time-resolved stereo-PIV' AIAA-2009-4043, 39th AIAA Fluid Dynamics Conference, San Antonio, Texas, 22-25 June.

- Veldhuis, L. L. M. and de Kat, R. (2008) 'Vortex wake investigation behind a wing-flap model with jet simulation,' 26th International Congress of the Aeronautical Sciences, Anchorage, Alaska, .

- de Kat, R., van Oudheusden, B. W. and Scarano, F., (2008) 'Instantaneous planar pressure field determination around a square-section cylinder based on time-resolved stereo-PIV,' 14th Int. Symp. on Application of Laser Techniques to Fluid Mechanics, Lisbon, Portugal, 7-10 June.

- Veldhuis, L. L. M. and de Kat, R., (2008) ' Vortex wake investigation behind a wing-flap model with jet simulation,' International Workshop on Fundamental Issues Related to Aircraft Wakes (FAR-Wake Workshop), Marseille, France, 27-29 May.

- de Kat, R., van Oudheusden, B. W. and Scarano, F., (2008) 'Instantaneous planar pressure field determination around a square-section cylinder based on time-resolved stereo-PIV,' EWA Int. Workshop on Advanced Measurement Techniques in Aerodynamics, Delft, The Netherlands, 31 March-1 April.

- Lentink, D., Muller, U. K., Stamhuis, E. J., de Kat, R., van Gestel, W., Veldhuis, L. L. M., Henningston, P., Hedenstrom, A., Videler, J. J. and van Leeuwen, J. L. (2008) 'How swifts control their glide performance with morphing wings,' Annual Meeting Netherlands Society for Anatomy, Lunteren, The Netherlands, 4-5 January.

- Lentink, D., Muller, U. K., Stamhuis, E. J., de Kat, R., van Gestel, W., Veldhuis, L. L. M., Henningston, P., Hedenstrom, A., Videler, J. J. and van Leeuwen, J. L. (2007) 'How swifts control their glide performance with morphing wings,' SICB Annual Meeting 2007, Phoenix, Arizona, 3-7 January.

- Lentink, D., Muller, U. K., Stamhuis, E. J., de Kat, R., van Gestel, W., Veldhuis, L. L. M., Henningston, P., Hedenstrom, A., Videler, J. J. and van Leeuwen, J. L. (2007) 'How swifts control their glide performance with morphing wings,' Annual Main Meeting of the Society for Experimental Biology (SEB), Glasgow, United Kingdom, 31 March-4 April.

- Lentink, D., Muller, U. K., Stamhuis, E. J., de Kat, R., van Gestel, W., Veldhuis, L. L. M., Henningston, P., Hedenstrom, A., Videler, J. J. and van Leeuwen, J. L. (2006) 'How swifts control their glide performance

with morphing wings,' 13th BeNeLux Congress of Zoology, Leuven, Belgium, 27-28 October.

Magazines

- Veldhuis, L. L. M. and de Kat, R. (2007), 'Will wake vortex research save the A380?,' *Leonardo Times*, 11(1), 20-21.

Miscelaneous

- de Kat, R. (2010), Production of the front-cover image for *Journal of Bacteriology*, accompanying the paper:
  Sevcenco, A. M., Bevers, L. E., Pinkse, M. W. H., Krijger, G. C., Wolterbeek, H. T., Verhaert, P. D. E. M., Hagen, W. R., and Hagedoorn, P. L. (2010), 'Molybdenum Incorporation in Tungsten Aldehyde Oxidoreductase Enzymes from *Pyrococcus furiosus*,' *Journal of Bacteriology*, 192(16), 4143-4152.

Curriculum Vitae

Roeland de Kat was born on 11 May 1980 in Utrecht, The Netherlands. He finished secondary school (V.W.O.) at G.S.G. Helinium in Hellevoetsluis in 1998, after which he started his studies in Aerospace Engineering at Delft University of Technology. He obtained his BSc degree in Aerospace Engineering in May 2005 and his MSc degree with specialization in Aerodynamics in April 2007. As part of the MSc curriculum he did an internship in the group of Experimental Zoology at Wageningen University, which resulted in an article in Nature. The Master thesis work dealt with the influence of cold-jets on the vortex decay behind a generic wing-flap-jet aircraft model as part of the European Union Framework 6 project, 'FAR-Wake.' The work was carried out at the Aerodynamics Group, Delft University of Technology.

In May 2007 he started his doctoral project at the same group on the determination of instantaneous pressure under supervision of dr. ir. B. W. van Oudheusden and prof. dr. F. Scarano. The results of this work are presented in this thesis. In 2010 he spent three week as a visiting scholar at the Laboratory for Experimental Fluid Dynamics of Dr. Joseph Katz at the Johns Hopkins University. During the period where he did his doctoral research, he was involved in a number of other projects. He was responsible for the first year aerodynamics project (with a typical enrollment of 400+ students), which he coordinated for three years (first year as a teaching assistant) and after that he assisted in designing and running project. He was involved in flow visualization and force measurements on the Delfly, a flapping wing MAV, also in flow visualization of a laminar separation bubble on an unsteady pitching aerofoil, and in measuring forces on an unsteady pitching aerofoil by force balance as well as deriving them from PIV-data.